Pillar photonic crystals in integrated circuits

Document Version:

Publisher's PDF, also known as Version of Record (includes final page, issue and volume numbers)

Please check the document version of this publication:

• A submitted manuscript is the version of the article upon submission and before peer-review. There can be important differences between the submitted version and the official published version of record. People interested in the research are advised to contact the author for the final version of the publication, or visit the DOI to the publisher's website.
• The final author version and the galley proof are versions of the publication after peer review.
• The final published version features the final layout of the paper including the volume, issue and page numbers.

[Link to publication](#)

Pillar photonic crystals in integrated circuits

PROEFSCHRIFT

ter verkrijging van de graad van doctor

aan de Technische Universiteit Eindhoven,

op gezag van de Rector Magnificus, prof.dr.ir. C.J. van Duijn,

voor een commissie aangewezen door het College voor Promoties

in het openbaar te verdedigen op

maandag 16 juni 2008 om 16.00 uur

door

Abigaël Adriana Maria Kok

geboren te Borsele

Aan mijn ouders

Contents

Contents

Chapter 1
Introduction

This thesis focuses on photonic crystals and their use for photonic integrated devices. In this chapter the main concepts will be introduced and the boundary conditions for the integration will be defined. Section 1.1 gives a short introduction to the concept of photonic crystals. Section 1.2 gives the required background information on photonic integrated circuits in which the photonic crystal components are to be implemented. An overview of possible photonic crystal components and their functionalities are given in section 1.3. Different geometries can be used to create a photonic crystal. These geometries are compared in section 1.4. Section 1.5 describes the pillar-based photonic crystals in more detail. Finally, in section 1.6 the outline of this thesis is given.

1.1 Photonic crystals

A photonic crystal (PhC) is a periodic structure having a refractive index that is modulated with a wavelength-scale periodicity. The crystal can be periodic in one, two, or three dimensions. Some examples are shown in Fig. 1.1. At each interface between media of high and low refractive index, light is partly transmitted and partly reflected. Due to the periodicity of the crystal, multiple reflections arise when light passes through. These reflections constructively interfere over a certain range of wavelengths, the so-called stop band of the photonic crystal [1]. The Bragg grating is an example of a one-dimensional photonic crystal; the refractive index is periodically modulated only in the direction of propagation. In 3D photonic crystals an omni-directional stop band can be created [2].

The unit cell of a photonic crystal is defined as one period in each of the relevant directions. To open up a stop band, the refractive index contrast within the unit cell has to be large enough. The periodicity of the crystal translates into a periodicity in reciprocal k-space. The dispersion diagram, or band diagram, given by $\omega(k)$ is therefore periodic in k-space. The electromagnetic waves, the so-called Bloch modes, follow the periodicity of the PhC lattice.

In some well-defined three-dimensional photonic crystal configurations, where the refractive index contrast is high enough, light is prohibited to propagate in any direction within the crystal. In that case we speak of a complete photonic band gap. The translational symmetry of the crystal is an important issue. If one adds a defect to a PhC lattice, its properties are changed and a corresponding localized mode may exist. This means that an electromagnetic oscillation can be bound to that position by reflections in the surrounding photonic crystal. A mode is allowed to exist at the defect position, and due to the photonic band gap it can not escape through the crystal.

By adding a line of defects to the PhC instead of just a single defect, a waveguide can be created along which light in a certain frequency range is allowed to propagate. Since the light can not penetrate into the photonic crystal, very sharp waveguide bends can be made. Therefore, by tailoring the PhC, one has full control over the flow of light [4]. However, manufacturing and precisely tailoring a three-dimensional photonic crystal is challenging.

Instead of using a three-dimensional photonic crystal for waveguiding purposes, one could use a two-dimensional crystal. This type of photonic crystal consists of either holes or rods that are etched into a layer stack with a high-refractive-index core in between low-refractive-index claddings. The photonic crystal imposes in-plane confinement, whereas guiding in the third dimension is due to total internal reflection in the high-index core [5, 6]. This is indicated in Fig. 1.1(b), where the higher index in the
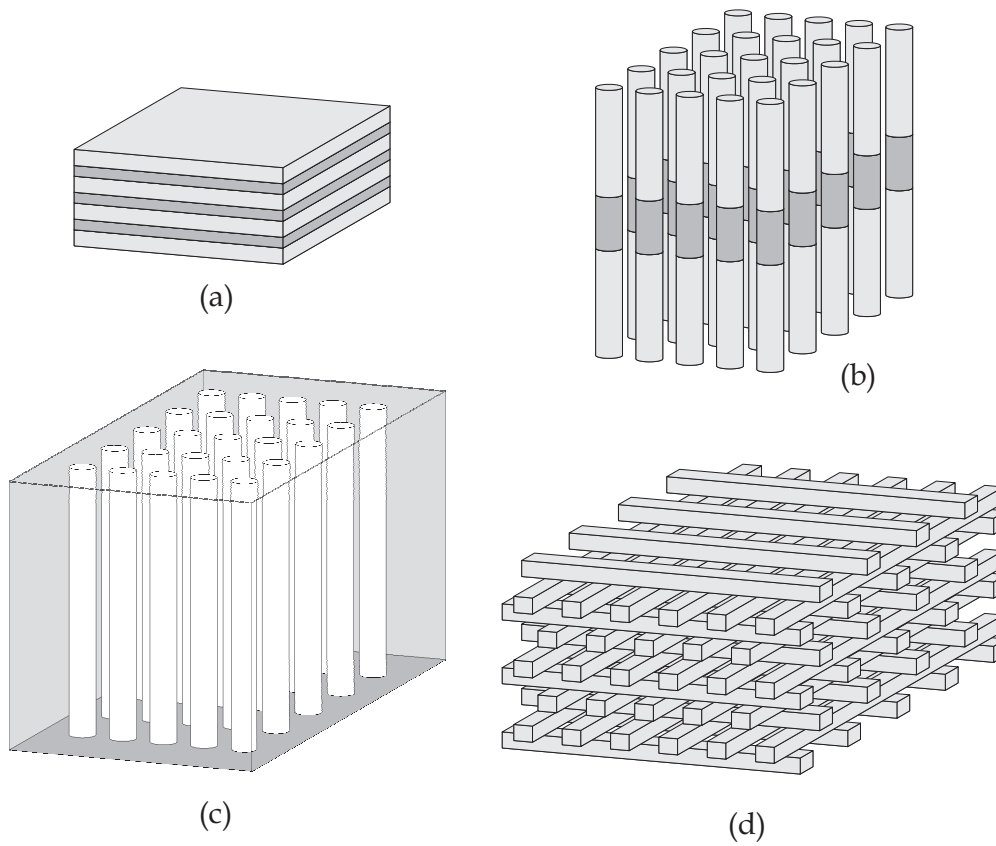
Figure 1.1: *Schematic representation of different types of photonic crystals; a) a one-dimensional photonic crystal, b) a two-dimensional photonic crystal based on pillars in air, c) a two-dimensional photonic crystal based on air holes in a high-dielectric medium, and d) a three-dimensional photonic crystal, the so-called woodpile structure [3].*

core layer of the 2D pillar-based PhC is represented by a darker grey. Two-dimensional PhCs are in principle suitable for integration in photonic integrated circuits.

1.2 Photonic integrated circuits

Photonic integrated circuits (PICs) can be realized in different material systems, depending on the applications. However, indium phosphide (InP) technology is the only platform to monolithically integrate active and passive devices for use in the near-infrared wavelength region (1300 – 1550 nm), which is important for telecom applications. In this material system, the guiding layer is an $In_{1-x}Ga_xAs_yP_{1-y}$ alloy that is epitaxially grown on an InP substrate and covered again by an InP cladding layer. The electronic band gap energy and the refractive index of the quaternary InGaAsP layer depend on the fractions x and y. The band gap energy can be tuned from 0.75 to 1.35 eV, corresponding to wavelengths from 1.65 to 0.92 μm [7]. InGaAsP has a direct electronic band gap, facilitating an efficient interaction with photons. Our interest is in the transmission window around 1.55 μm, and in that range InGaAsP can either be transparent, absorbing or amplifying. By tuning the electronic band gap energy in different areas of the chip, passive and active devices can be integrated in the same InGaAsP waveguiding layer.

In photonic integrated circuits, we have a set of components forming the building blocks of the circuits. Examples of passive building blocks are bends, multimode interference couplers (MMIs [8]), distributed Bragg reflectors (DBRs), electro-optical switches [9], arrayed waveguide gratings (AWGs [10]) and polarization filters, splitters [11] and converters [12]. Active building blocks are for instance semiconductor optical amplifiers (SOAs [13]), photodetectors and saturable absorbers (SAs). The building blocks on the chips are interconnected via ridge waveguides. To distinguish these well-established PICs and components from their PhC-based equivalents, we refer to them as 'classical' in the rest of this thesis.

The aim of this thesis is to investigate the feasibility of integrating components based on two-dimensional photonic crystals with classical components. The first reason to explore the possibilities to integrate PhC components in classical PICs is that in PhCs light can be confined in much smaller volumes than can be done with classical waveguides. This implies that PhC components can be made with much smaller footprints than components based on classical waveguide technology. Secondly, PhCs can add new functionalities to the classical circuits. To integrate PhC-based devices in classical waveguide circuits, we need to design the PhC components in such a way that they can be connected to the ridge waveguides. Furthermore, the fabrication technologies of both ridge waveguides and PhC components have to be compatible.

4
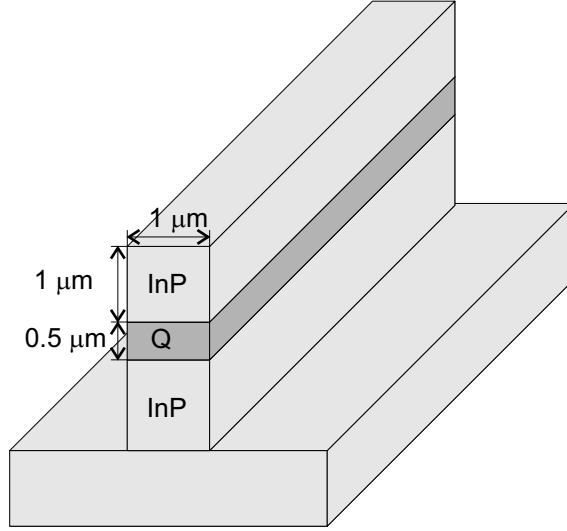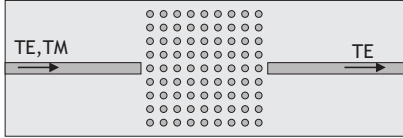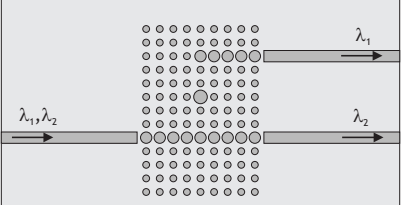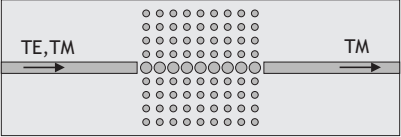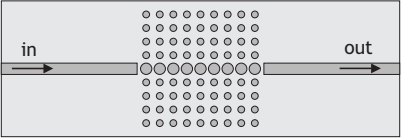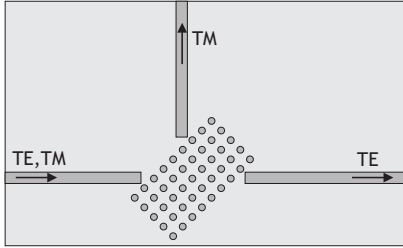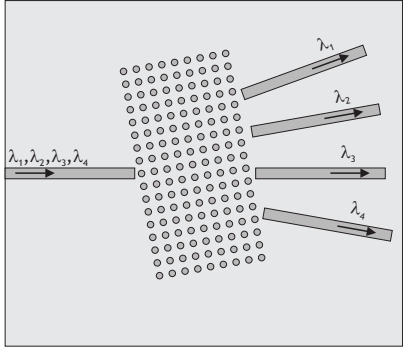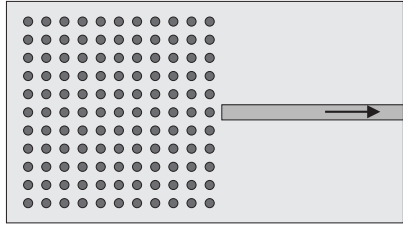
Figure 1.2: *Classical ridge waveguide for connecting the building blocks of a photonic integrated circuit.*

All components are designed in a layer stack with an InGaAsP [Q(1.25 μm)] core layer of 500 nm thickness, with an InP top cladding of 1 μm thickness on an InP substrate. The refractive index of the quaternary layer is $n_{\text{InGaAsP}} = 3.3640$ and that of the InP is $n_{\text{InP}} = 3.1693$ (both at $\lambda = 1.55$ μm [14]). The ridge waveguides connecting the PhC components to the classical components are assumed to have a width of 1 μm. A schematic picture of the interconnecting waveguide is shown in Fig. 1.2.

1.3 Photonic crystal-based components

Due to the special properties of PhCs (and defects in them) one can create small (micron size) components. On the one hand, we can distinguish between photonic crystals with and without defects. On the other hand, the materials used can be either passive or active at the wavelength range of interest. An overview of the four possible combinations that follow from these two distinctions is given in Table 1.1, with some examples of PhC-based devices that are suitable for integration in classical PICs. In this section, we shortly describe the functionalities of these components.

Passive, defect-free crystal. A two-dimensional photonic crystal responds differently to TE and TM polarization, where TE is the polarization with the *E*-field com-

	defect-free PhC	PhC with defects
passive	a) polarization filter: TE,TM → ▫▫▫ → TE b) polarization splitter: TM ↑ TE,TM → → TE c) wavelength demultiplexer: $\lambda_1, \lambda_2, \lambda_3, \lambda_4$ → λ_1 / λ_2 / λ_3 / λ_4	d) wavelength drop filter: λ_1 λ_1, λ_2 → λ_2 e) polarization filter: TE,TM → → TM f) delay line: in → → out
active	g) band edge laser: →	h) micro laser: →

Table 1.1: *Overview of photonic crystal-based devices for integration in PICs. The darker grey in the pictures in the lower row indicates active material.*

6

ponent in the plane of the circuits, and TM is the polarization with the E-field component parallel to the rods or holes[1]. The polarization sensitivity of a two-dimensional photonic crystal can be used to make micron size polarization filters or splitters [16, 17, 18]. E.g., a crystal with a TM band gap would filter out this polarization, while allowing the TE polarization to pass through (see Table 1.1(a)). By placing such a crystal under an angle with respect to the incoming waveguide, the reflected TM polarized light can be captured in a second output waveguide and a polarization splitter is created (see Table 1.1(b)). Furthermore, by exploiting the high spatial dispersion (the so-called superprism phenomenon), one could make a very small wavelength splitter for wavelength division multiplexing purposes (see Table 1.1(c) [19]).

Passive crystal with defects. By adding a line defect one can make a photonic crystal waveguide. With a cavity (e.g. a single defect) in between such waveguides, light at the cavity resonance wavelength can be coupled from one waveguide to the other (see Table 1.1(d)). Another possibility is to exploit again the polarization sensitivity to make polarization filters, where one polarization is guided and the other is either blocked or scattered into the surrounding photonic crystal (see Table 1.1(e) [20]), or polarization splitters, where the two polarization states are guided in different directions [21]. Furthermore, an interesting feature of photonic crystals is the fact that modes at certain frequencies can have a very low group velocity. A waveguide designed to support such a slow mode could be used in delay lines [22] or in pulse compressors (see Table 1.1(f)).

Active, defect-free crystal. A finite, defect-free photonic crystal can act as a cavity itself if the PhC Bloch modes are trapped inside the crystal [23]. If the gain spectrum of the active material coincides with the frequencies of low group velocity, we obtain a strong interaction with the material. The light will build up inside the crystal and if the gain is large enough to compensate for the losses, the structure can act as a laser (see Table 1.1(g)). By selecting certain patterns of unit cells to be pumped, one lasing mode can be selected. Different patterns give different modes, and thus different emission wavelengths [24].

Active crystal with defects. A cavity can be created by introducing a single defect in a PhC. These cavities are used in active devices to make micro lasers (see

---

[1]In literature, TE and TM polarization in 2D photonic crystals are sometimes defined differently, see for example Ref. [15]. In this work, the polarization states correspond to those as defined in Ref. [4], as this is the most commonly used definition and it corresponds to the definition in conventional waveguide technology.

Table 1.1(h)). The quality factor Q of a cavity mode is defined as the ratio of the full width at half maximum of the cavity resonance in the frequency domain $\Delta\omega$ to the center frequency ω_c. This Q factor indicates the losses from the resonating mode. It can be increased by modifying some of the unit cells surrounding the defect cell to reduce these losses.

In this section we have briefly introduced some possible applications for two-dimensional photonic crystals in PICs. We have seen that if we can tune the PhCs to fit our needs, a variety of components is within reach, with either reduced size or novel functionality with respect to classical devices. In the next section we will discuss the advantages and disadvantages of the possible PhC geometries for these applications.

1.4 Photonic crystal geometries

We can distinguish photonic crystals by the contrast in dielectric constants of the core and the cladding layers. Fig. 1.3 shows a schematic picture of the refractive indices. A PhC is said to have a high vertical index contrast if $\Delta\varepsilon_{vert} = \varepsilon_{h,1} - \varepsilon_{h,2} = n_{h,1}^2 - n_{h,2}^2 \geq 10$ [6]. A membrane-type photonic crystal has a high vertical index contrast. However, a deeply etched photonic crystal is a low-vertical-index-contrast PhC with $\Delta\varepsilon_{vert} \leq 2$. Regardless of the vertical index contrast, the lateral index contrast $\Delta\varepsilon_{hor} = \varepsilon_{h,eff} - \varepsilon_{l,eff} = n_{h,eff}^2 - n_{l,eff}^2$ has to be sufficient to open up a photonic band gap that is large enough for applications in photonic devices (see section 2.1.1 for details on the effective index method).

We have already seen that two-dimensional photonic crystals either consist of low-dielectric rods in a connected high-dielectric lattice (the hole-type crystals) or of high-dielectric pillars embedded in a low-dielectric medium (the pillar-based crystals). As both of these can have either a high or a low vertical index contrast, this leads to four possible geometries.

- Membrane holes: hole-type crystals with a high vertical index contrast

- Membrane pillars: pillar-based PhCs with a high vertical index contrast

- Deeply etched holes: hole-type crystals with a low vertical index contrast

- Deeply etched pillars: pillar-based crystals with a low vertical index contrast

Given the InP/InGaAsP/InP layer stack, the pillars with a high vertical index contrast are not a technologically realizable option. Therefore, in this section we will compare the other three types of photonic crystals. All three photonic crystal types exhibit
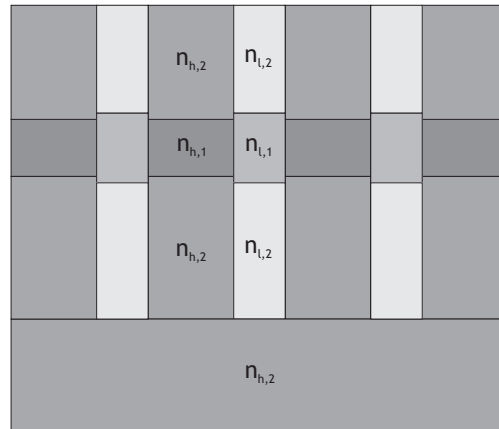
Figure 1.3: *Schematic picture of a cross section of a photonic crystal, where the refractive indices of the materials are indicated.*

specific advantages and disadvantages on different aspects. Here we discuss the most important issues with respect to the integration of PhC devices in classical waveguide circuits.

Polarization. For structures where islands of high-dielectric material are interconnected, the TE band gap dominates. This is the case for hole-type photonic crystals. The TM band gap prevails if the low-dielectric material is interconnected, which is the case for the pillar photonic crystals. However, if the lateral index contrast is high enough, overlapping TE and TM band gaps can be found for both crystal types [4]. For the hole-type photonic crystal, a hexagonal lattice provides such a situation, whereas in the case of pillar photonic crystal, the so-called honeycomb lattice can have a band gap for both polarizations. A hexagonal lattice of low-index holes provides a large TE band gap, and for an optimal TM band gap a square lattice of pillar photonic crystal is the most suitable configuration.

Intrinsic losses. In a two-dimensional photonic crystal waveguide with a high vertical index contrast, it is possible to excite a Bloch mode that can not be coupled to an out-of-plane radiation mode [5]. Thus, it will not experience losses as long as the crystal is ideal, i.e. infinitely large in lateral directions. However, if an extra defect is added to the photonic crystal waveguide, the perfect symmetry of the structure is broken. This implies that curves, splitters, etc. will have relatively high excess losses in crystals with a high vertical index contrast.

9

In section 2.4 it will be shown that for PhC waveguides with a low vertical index contrast it is possible to have very low propagation losses by avoiding the excitation of those Bloch mode components that are able to couple to radiation modes. In that case, even adding defects to the crystal does not induce coupling to out-of-plane radiation modes. This approach is based on a different physical mechanism as the lossless Bloch modes in membrane PhCs.

Roughness-induced losses. The losses that are induced by roughness of the side walls increase with lateral index contrast. This is because roughness disturbs the electromagnetic field, so loss increases as $(\Delta n)^2$ [25]. In membrane photonic crystals, the lateral index contrast (i.e. the contrast between $n_{h,eff}$ and $n_{l,eff}$) is lower than in deeply etched structures. The losses due to roughness will thus be lower for the membrane crystals. If the lateral index contrast of deeply etched PhCs can be reduced, the losses will decrease correspondingly.

Technology. The membrane photonic crystals are created by selective wet etching of the InP below an InGaAsP layer after this layer has been etched through with reactive ion etching [26, 27, 28]. Since the required etch depth in the dry etching process is less than a micrometer, the fabrication process in itself is easier than that of the deeply etched photonic crystals, where etch depths of several micrometers are required. However, there is a major drawback if one wants to integrate the membrane photonic crystals in a photonic integrated circuit. The excitation of higher order modes in normal direction will affect the band gap properties of the crystal. This imposes restrictions on the maximum thickness of the guiding layer. Due to the high vertical index contrast in membranes, the thickness of the InGaAsP layer should be ≤ 240 nm to have it single-mode. To integrate these membranes with classical ridge waveguides, consisting of a 500-nm-thick guiding layer and a 1 μm InP top cladding, vertical tapering is needed. This considerably complicates the fabrication process. For the photonic crystals with a low vertical index contrast, the same layer stack can be used as in classical ridge waveguides. For these crystals the deep reactive ion etch is the most challenging step in the fabrication process [29, 30, 31]. Comparing the deeply etched holes and the pillars, the latter features are slightly easier to etch. Etching products are removed more efficiently in this geometry, since the open (etched) area is larger than in the case of a hole-type crystal and it is interconnected.

Mechanical stability. The deeply etched holes have the highest mechanical stability of the different types of photonic crystal. However, since the InP-based layer stack is an epitaxially grown, lattice-matched stack, also the pillar photonic crys-

tals are mechanically stable, as is confirmed by experiments. Membrane PhCs are less favorable in this respect. If the area of such a membrane is larger than about 20 μm, the membrane runs the risk of collapsing which will destroy the PhC.

Electrical contacting. A huge potential is created if the photonic crystals can be electrically pumped. A big advantage of the pillar photonic crystals as opposed to hole-type photonic crystals, is that pillars inherently avoid current spreading in the active layer. Furthermore, if the pillars can be passivated and planarized by a polymer layer, the addition of electrical contacts is relatively straightforward. This makes fabrication of active components based on III-V pillar photonic crystals feasible. It is even possible to contact one or a few pillars individually, which opens up possible applications like micro lasers. Especially for membranes electrical contacting is much more difficult to realize.

Thermal properties. In pillar PhCs as well as in deeply etched holes, heat that is generated in active devices can dissipate easily to the InP substrate. By placing the chip on a temperature controlled chuck, the temperature stability can be regulated. Heat dissipation in active components is one of the major bottlenecks in membrane PhC technology.

In this section we have discussed the advantages and drawbacks of three types of photonic crystals. Based on this discussion we are able to make a choice for the kind of PhC that is best suited for components that are compatible with classical PICs.

1.5 Two-dimensional photonic crystals based on pillars

The scope of this project is to investigate the feasibility of integrating photonic crystal-based components in classical photonic integrated circuits in InP technology. For membrane photonic crystals the material layer stacks as well as the fabrication technology are not compatible with those of the PICs. This is a serious drawback, and therefore we disregard this geometry.

In literature, much experimental results are reported on deeply etched holes [29, 31, 32, 33]. From a technological point of view, deeply etched hole-type photonic crystals are suitable for passive devices integrated in classical PICs. However, active devices are more difficult to realize in this type of photonic crystal.

On the pillar-based PhCs, very few experiments are reported in literature[34, 35, 36, 37, 38, 39]. However, a huge number of publications can be found on the modeling and theoretical aspects of those crystals. Therefore, once a suitable fabrication

process is developed for pillar PhCs, a large number of possible applications opens up. Furthermore, pillar-based PhCs are best suited for active devices because of the possibility for electrical contacting and the efficient heat dissipation to the substrate.

The large TM band gap of pillar-based PhCs enables the realization of components that can manipulate polarization on a very short length scale. A polarization splitter made with classical PIC building blocks has a length in the order of millimeters. By using PhCs, this length could be reduced to a few tens of micrometers.

The out-of-plane losses of pillar-based photonic crystals can be significantly reduced by implementation of a polymer layer stack between the semiconductor pillars. This will be shown in section 2.4. Additionally, one could anticipate the use of functional polymers. They could for instance contain liquid crystals of which the refractive index can be tuned by applying an electric field over the polymer layer stack. A change in refractive index slightly changes the wavelength range of the photonic band gap of the crystal. In this way switching or modulation of optical signals can be achieved. Another option is to use non-linear polymers. Combined with the control over propagation properties offered by PhCs, this would open up the way to a platform for non-linear optical signal processing, such as opto-optical switching, four-wave mixing, frequency doubling, etc.

Based on the previous discussions, this thesis focuses on two-dimensional photonic crystals based on pillars in a background of low refractive index. They offer excellent possibilities for integration in the conventional PICs and they are suitable for use in active as well as in passive devices. The major problem to be tackled in this case is the excessive loss that pillar photonic crystals have shown until now. How this is addressed is the subject of the next chapter. By developing a technology platform for these pillar photonic crystals, a huge number of applications in PICs is within reach.

1.6 Outline of this thesis

In the next chapters, the suitability of pillar-based photonic crystals is first investigated from a theoretical point of view. A general introduction to pillar photonic crystals is given in chapter 2. In this chapter, the concept of waveguiding in photonic crystals is treated, where the in-plane and out-of-plane confinement are considered separately.

The modeling of the transmission and reflection of photonic crystal waveguides, and the connection of these to classical ridge waveguides, is the subject of chapter 3. The design of a first set of photonic crystal based devices, TE and TM filters, is described.

After the theory and modeling of pillar photonic crystals, the fabrication issues are treated in chapter 4. A technology scheme was developed for the integration of pillar

photonic crystals in a photonic circuit based on classical waveguides.

In chapter 5 the layout of the designed chip is described. Furthermore, the results of transmission measurements are given and related to the modeling results.

Finally, the achievements of this work are summarized in chapter 6. Recommendations for future research are given in this chapter as well.

Chapter 2
Pillar-based photonic crystals

This chapter describes the theory of planar photonic crystals based on pillars and the modeling of photonic crystal waveguides. In a slab photonic crystal component, light is confined in-plane by the photonic band gap properties of the crystal, whereas the guiding in the out-of-plane direction is based on the mechanism of total internal reflection. To design and model the components, three-dimensional calculations are needed. However, these calculations are very time consuming and impose strong requirements on computational power. Therefore the in-plane and out-of-plane confinement problems are treated separately in the design simulations. After optimization of the design, the results will be verified by full 3D simulations (see chapter 3).

In section 2.1 a short introduction is given to the simulation tools that are used in this work. In section 2.2 the photonic band gap properties of two-dimensional photonic crystals are reviewed. In section 2.3, line defects are introduced in the two-dimensional crystal to create waveguides, where the in-plane confinement is imposed by the photonic band gap of the crystal. Section 2.4 reports on the out-of-plane loss and the implementation of a polymer layer stack to introduce a guiding layer between the pillars. Finally, in section 2.5, conclusions are drawn.

Table 2.1: *Overview of refractive indices of the materials that are used in this thesis. All indices are taken at* $\lambda = 1550$ *nm and for TM polarization.*

(a)			(b)	
III-V stack			polymer stack	
$n_{h,1}$	3.3640		$n_{l,1}$	1.64
$n_{h,2}$	3.1693		$n_{l,2}$	1.38
$n_{h,eff}$	3.2641		$n_{l,eff}$	1.5236

2.1 Modeling tools

Different modeling tools are used to model the behavior of photonic crystals and to optimize for the geometrical parameters within the constraints imposed by the InP-based material stack. These simulation methods are introduced in this section.

2.1.1 Effective-index method

When designing a component, it is often convenient to start with 2D simulations to get an initial design which can then be further optimized by full 3D simulations. To account for the third dimension in the 2D simulations, the effective index method (EIM) can be used. The basic idea of this method is to take the effective refractive index of the guided mode in normal direction to represent that direction in the plane of 2D simulation, as is illustrated in Fig. 2.1. The photonic crystal in Fig. 2.1(a) consists of two material 'stacks', one is the III-V semiconductor stack of the pillars, and the other is the background of air (or polymers). First, we compute the effective index of the fundamental guided mode in the III-V slab waveguide. The guided mode always has an effective index $n_{h,2} < n_{h,eff} < n_{h,1}$, and it depends on the layer thicknesses and on the wavelength. In this case, the pillars are surrounded by air, having a refractive index of 1.0. The effective index for 2D simulations is equal to that value. In case a polymer layer stack is used, the guided mode of that structure provides the effective index of the background. All refractive indices that are relevant in this thesis, are given in Table 2.1.

As mentioned before, the effective refractive index depends not only on the material stack, but also on the wavelength. Photonic crystal band calculations cover a large range of frequencies (see section 2.1.2). However, the effective index always has a value between that of the refractive indices of core and cladding materials. For a PhC

(a)   (b)
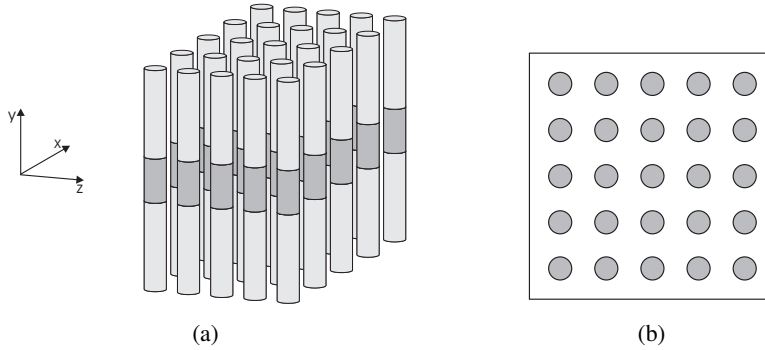
Figure 2.1: *Illustration of the effective index method; a) a three-dimensional structure of a two-dimensional slab PhC, where the core and claddings have refractive indices $n_{h,1}$ and $n_{h,2}$, respectively, and b) a two-dimensional PhC where the circles have a refractive index $n_{h,eff}$, being the effective refractive index of the fundamental TM mode in a material stack with indices $n_{h,1}$ and $n_{h,2}$.*

with low vertical index contrast, the variation in the effective index will thus be small over a large range of optical frequencies, but especially in PhCs with a high vertical index contrast, the effective refractive index varies considerably. In the InP technology platform, due to the low vertical index contrast, the EIM approximation is well suited within the frequency range of interest [40].

2.1.2 Band solver

The band solver that is used to compute band diagrams, is the commercially available software package CrystalWave [41]. A bulk photonic crystal can be regarded as an infinite repetition of a unit cell. After a 2D unit cell has been defined, the band solver computes the solutions of this unit cell with periodic boundary conditions in two directions. The unit cell can be that of a bulk lattice without defects, but it can also be a unit cell of a photonic crystal waveguide, as is shown in Fig. 2.2. A PhC waveguide existing of a line defect is periodic in the direction of propagation with the same lattice constant as that of the surrounding crystal. By extending the unit cell in the transverse direction, so that it covers several periods on each side of the waveguide, it can be used to compute the bands of the waveguide in the propagation direction. In that case we refer to the unit cell as a super cell, because it extends into the surrounding photonic crystal over several lattice constants. Since the super cell itself has also periodic boundary conditions, in fact an infinite number of waveguides are virtually placed next to each other. If the distance between these waveguides is large enough (by extend-
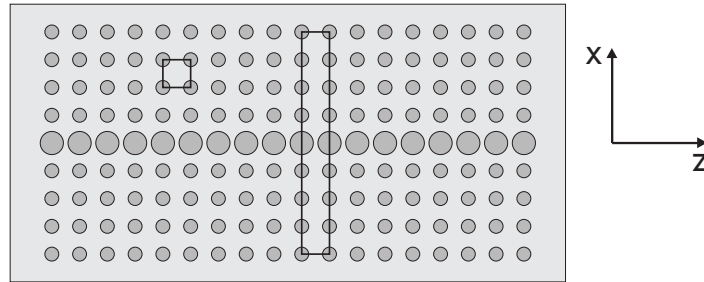
Figure 2.2: *Unit cells in a band solver calculation. The unit cell on the left is used to compute the band diagram of the undisturbed lattice, whereas the super cell on the right is used to compute the bands of guided modes along the photonic crystal waveguide.*

ing the super cell over enough periods on both sides of the waveguide), they are not coupled and they do not influence each other.

2.1.3   Eigenmode expansion method

In some of the calculations, e.g. the grating simulations that will be described in section 2.4.2, the software package CAMFR is used [42]. This is a freely available program developed by Bienstman at the university of Ghent, Belgium. The software is based on an eigenmode expansion algorithm. As yet, it was only available for 2D calculations.

In CAMFR, a structure is divided into slices perpendicular to the direction of propagation. Within a slice, the refractive index profile is constant in the propagation direction. The fields in each slice are written as a sum of the eigenmodes of that slice. The propagation of the field from the starting point to the end point of the slice is accounted for by a phase term. At the interface with a next slide, the overlap between the fields of the eigenmodes in both slides gives the transmission and reflections.

The eigenmode expansion method requires a discrete set of modes within a finite calculation window. The boundary conditions of the calculation window can cause parasitic reflections; light radiating away from the simulated structure can be reflected at the window boundaries and be recaptured by the structure. To overcome this problem, perfectly matched layers (PMLs) are introduced. These PMLs absorb the radiated light, suppressing reflections.

For 2D photonic crystals with circular structures, the slicing of the structure might cause uncertainties due to a staircase approximation of the (effective) refractive index profile. The discontinuities at the interfaces can cause non-physical reflections. There-

fore, the program is less suitable for calculations on objects with continuously varying widths.

2.1.4 Finite difference time domain method

In contrast to the eigenmode expansion method, the finite difference time domain method (FDTD) uses a computational grid with a fixed spacing. The Maxwell equations are solved for each interval in time, making it a very powerful simulation tool. The main drawbacks of FDTD calculations are the computation time and the memory requirements. The FDTD method is included in the software package Crystal-Wave [41]. It can perform 2D as well as 3D calculations. Like in CAMFR, perfectly matched layers are used to avoid parasitic reflections from the boundaries of the calculation window. FDTD is in this thesis used to calculate the transmission and reflection of complex 2D structures that are not easily divided in slices, making the CAMFR software less accurate. Furthermore, FDTD is used for 3D calculations.

A structure can be excited in CrystalWave with a pulse or with a continuous wave signal, either with a Gaussian profile or with a certain waveguide mode. To get the frequency response of a device, a pulse excitation is used. The bandwidth of the calculation is determined by the (inverse of the) time duration of the pulse. The field at a certain wavelength can be found by excitation with a continuous wave signal. In our simulations, we excite the fundamental guided TM mode.

Now we have briefly introduced the various modelling tools that are available, we can use these to investigate the properties of photonic crystals, as will be done in the remaining sections of this chapter.

2.2 Two-dimensional pillar photonic crystals

In this section, the basic properties of 2D photonic crystals are described; we will introduce the concepts of Bloch modes, Brillouin zones, band diagrams, gap maps and the light line. For an introduction to 1D, 2D and 3D photonic crystals, we refer to Joannopoulos [4]. For the more specific case of 2D planar PhC's exploiting total internal reflection in the third dimension, Bogaerts gives a comprehensive introduction [6].

All the graphs and calculation results presented in this section, are obtained by the 2D band solver and by use of the EIM, both of which were introduced in the previous section.

2.2.1 Bloch modes and the Brillouin zone

Consider a dielectric medium with a non-uniform refractive index $n = n(\mathbf{r})$. The wave equation for the electric field in such a medium is

$$\frac{c^2}{n^2(\mathbf{r})}\nabla^2 \mathbf{E}(\mathbf{r},t) - \frac{\partial \mathbf{E}^2(\mathbf{r},t)}{\partial t^2} = 0 \tag{2.1}$$

where $\mathbf{E}(\mathbf{r},t)$ is the electric field as a function of position $\mathbf{r}$ and time t, and c is the speed of light in vacuum. We will apply this wave equation to find the modes in photonic crystal structures.

The simplest photonic crystal is a 1D photonic crystal, where the refractive index is periodically modulated in one direction, defined here as the z-direction. Because the refractive index is periodic with a lattice constant a, we have

$$n(z) = n(z+a) \tag{2.2}$$

The Bloch theorem states that the solution of the wave equation of such a crystal is

$$E(z,t) = u_k(z)e^{jkz}e^{-j\omega t} \tag{2.3}$$

where k is the wavevector in z-direction. The function $u_k(z)$ has the same periodicity as $n(z)$:

$$u_k(z) = u_k(z+a) \tag{2.4}$$

Because the field is periodic in space, it can be expanded in a Fourier series, resulting in

$$E(z,t) = \sum_{m=-\infty}^{\infty} c_m \exp(j(k + \frac{2\pi m}{a})z)\exp(-j\omega_k t) \tag{2.5}$$

where the c_m are the coefficients of the Fourier components of the Bloch mode and m is an integer number. Increasing k by an integer times $2\pi/a$ leaves the Bloch state unchanged, although it influences the numbering of the Fourier components c_m. The mode frequencies are therefore periodic in k:

$$\omega(k) = \omega(k + \frac{2\pi m}{a}) \tag{2.6}$$

Therefore, to investigate the dispersion relation $\omega(k)$ of this 1D photonic crystal, it suffices to regard only the wave vectors $-\pi/a < k < \pi/a$. This region is called the first Brillouin zone.

So far we have only regarded a 1D photonic crystal, but the concepts are easily extended to 2D and 3D photonic crystals. Here we will only consider 2D photonic

crystals, as in this thesis we aim for planar integration in PICs. In the case of a 2D photonic crystal, we assume the refractive index to be modulated in x and z direction (see Fig. 2.1 for the definition of the axes). Consider a square-lattice PhC with lattice constant a. The refractive index is invariant under a translation over any linear combination of the elementary lattice vectors $\mathbf{R}$, where

$$\mathbf{R} = la\hat{x} + ma\hat{z} \tag{2.7}$$

According to the Bloch theorem, the solution of the wave equation is

$$\mathbf{E_k}(\mathbf{r},t) = \mathbf{u_k}(\mathbf{r})e^{j\mathbf{k}\cdot\mathbf{r}}e^{-j\omega t} \tag{2.8}$$

and

$$\mathbf{u_k}(\mathbf{r}) = \mathbf{u_k}(\mathbf{r}+\mathbf{R}) \tag{2.9}$$

The Fourier expansion of the field is now

$$E(x,y,z,t) = \sum_{l=-\infty}^{\infty}\sum_{m=-\infty}^{\infty} c_{lm}(y)e^{j(k_x+2\pi l/a)x}e^{j(k_z+2\pi m/a)z}e^{-j\omega_k t} \tag{2.10}$$

and the mode frequencies are periodic in k-space:

$$\omega(\mathbf{k}) = \omega(\mathbf{k}+\mathbf{G}) \tag{2.11}$$

with the reciprocal lattice vector

$$\mathbf{G} = \frac{2\pi l}{a}\hat{x} + \frac{2\pi m}{a}\hat{z} \tag{2.12}$$

Also in 2D photonic crystals, the periodicity in spatial frequency can be exploited to regard only the Brillouin zone of the lattice. Fig. 2.3 shows a 2D square-lattice photonic crystal with its first Brillouin zone in reciprocal space. For symmetry reasons, the irreducible Brillouin zone (the darker grey area in the Brillouin zone of Fig. 2.3(b)) gives all information that is needed to obtain the dispersion relation $\omega(\mathbf{k})$. The high-symmetry points are denoted by Γ, X and M by convention. In the rest of this thesis, we will focus on PhC lattices with this square geometry.

2.2.2 Band diagrams and gap maps

The dispersion relations of a photonic crystal can be computed using a band solver (see section 2.1.2) and the results are plotted in a band diagram. In a 2D photonic crystal, the k-vector has two in-plane components, so the band diagram $\omega(\mathbf{k})$ would result in a
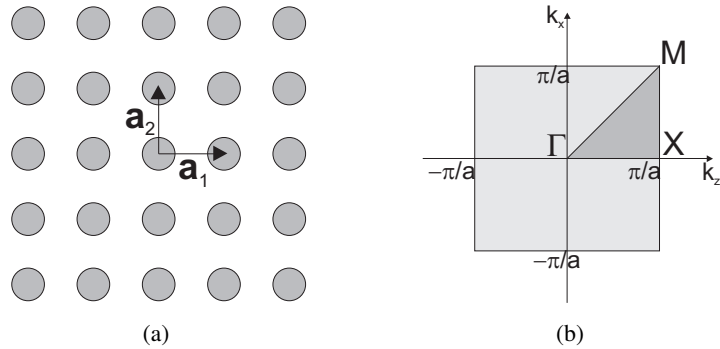
Figure 2.3: *A two-dimensional square lattice with the first Brillouin zone and the irreducible Brillouin zone.*

3D graph. However, it is often convenient to plot only the frequencies along the edges of the irreducible Brillouin zone.

Because of the scalability of Maxwell's equations, both **k** and ω can be normalized with the lattice constant. The *k*-vector can be expressed in π/a, whereas the frequency ω can be expressed in units of a/λ. In this way, the only parameters that determine the band diagram are the structure of the unit cell, the refractive indices of the media and the ratio between high-index and low-index dielectrics.

Fig. 2.4 shows a band diagram of a 2D photonic crystal, consisting of a square lattice of circles with $n_{h,eff} = 3.2641$ and radius $r = 0.25a$, in a background medium with $n_{l,eff} = 1.0$. The lowest frequency bands for the two polarizations are plotted. TE is the polarization with the electric field vector in the plane perpendicular to the rods, and TM is the polarization with the electric field vector parallel to the rods. Since the TM band gap can be exploited for in-plane confinement of the light, the rest of this chapter focuses on that polarization.

In the normalized frequency range from 0.265 to 0.368, between the first and the second band, no TM bands (modes) are present. The photonic crystal has a 2D band gap for TM-polarized light at those frequencies. Since TE-polarized light is allowed to propagate in the crystal, the band gap is not a complete 2D band gap. This polarization sensitivity can be employed in components such as polarization filters and polarization splitters, as will be discussed in more detail in chapter 3. Note that there are two smaller TM band gaps in the frequency ranges from 0.493 to 0.557 and from 0.875 to 0.882.

The bands above and below the gap can be distinguished by their field distributions in the photonic crystal. The field of the lower band is more concentrated in the high-
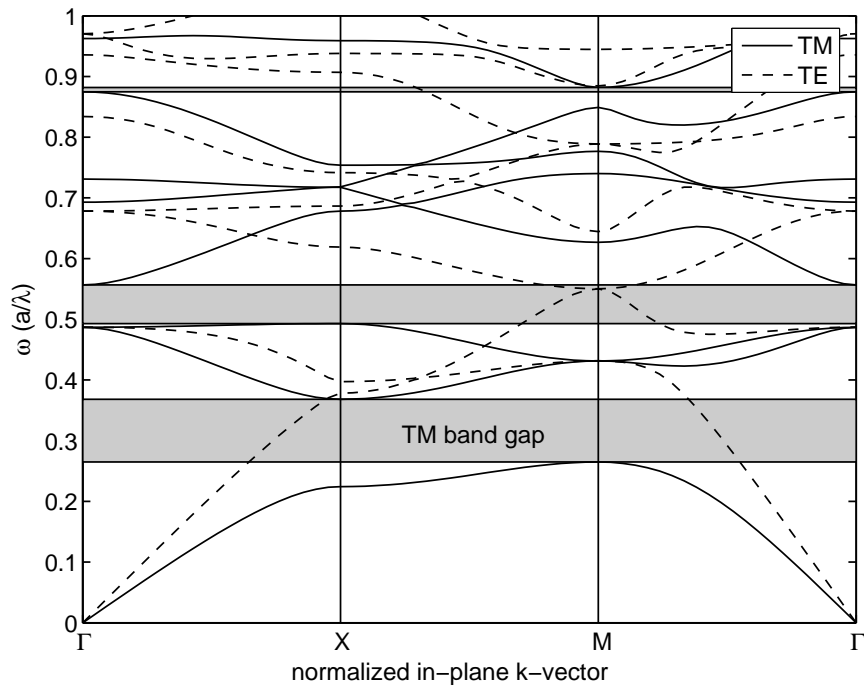
Figure 2.4: *2D band diagram of a square array of high-refractive-index pillars ($n_{\text{h,eff}} = 3.2641$) in air ($n = 1$) with $r/a = 0.25$. The solid curves represent TM modes whereas the dashed curves represent TE modes. The grey areas indicate the TM band gaps.*

index regions than the field of the upper band. By convention, the band below a gap is therefore called the dielectric band, whereas the band above a gap is called the air band[1].

Up to this point we have not introduced any dimensions to the PhC. Due to the scalability, we can normalize all properties of the band diagram with the lattice constant a. Now, let us impose the condition that the center frequency of the TM band gap has to be at the telecom wavelength $\lambda = 1550$ nm. The center frequency of the TM band gap is $\omega_c = 0.317$. If we take this frequency to be at $\lambda = 1550$ nm, the corresponding lattice constant is given by $a = \lambda\omega_c \simeq 491$ nm. The corresponding pillar radius is $r = 0.25a \simeq 123$ nm. The stop band ranges from $\lambda_{min} = a/\omega_{max} \simeq 1334$ nm to $\lambda_{max} = a/\omega_{min} \simeq 1853$ nm.

We mentioned before that the band diagram can be influenced by the the ratio of rod radius over the lattice constant r/a and by the effective refractive index contrast of the media. Both properties affect the size and the center frequency of the band gap. To visualize these effects, one can make use of a so-called gap map. In such a graph, the sizes and center frequencies of the band gaps as calculated by the band solver are plotted against the varying r/a or index contrast. Fig. 2.5(a) represents the gap map of the square lattice of rods in air, showing the TM band gap as a function of the normalized radius. The frequencies of the band gaps decrease as r/a increases. This can be explained by the fact that as r/a increases, the average refractive index of the crystal increases as well, inducing a reduction in the frequency[2].

If a polymer layer stack is implemented to create a guiding layer between the semiconductor pillars, the effective refractive index contrast between the pillars and the low-index medium is reduced. To illustrate the effect on the photonic band gap properties of the crystal, fig. 2.5(b) shows the gap map as function of the effective refractive index of the background $n_{l,eff}$. The normalized radius is kept constant ($r/a = 0.25$) and $n_{l,eff}$ is varied from 1.0 to 2.0. When the lower refractive index increases, the average index increases so the center frequency of the gap is again reduced. Since the wavelength scales inversely with normalized frequency, the dimensions of a photonic crystal operating at the same wavelength become smaller. This effect is more pronounced for the upper boundary of the gaps than for the lower boundary. This is explained by the fact that the lower boundary corresponds to the dielectric band of the crystal, for which the mode intensity is concentrated in higher-index regions, whereas the upper boundary represents the air band, having most of its intensity located in the lower-index regions. Since the lower refractive index is changed, the effect on the upper frequency of the gap is much larger than the effect on the lower band gap frequency.

---

[1] In electric band diagrams, these bands are called the valence and conduction bands.

[2] In a homogeneous medium: $\omega = ck/n$.
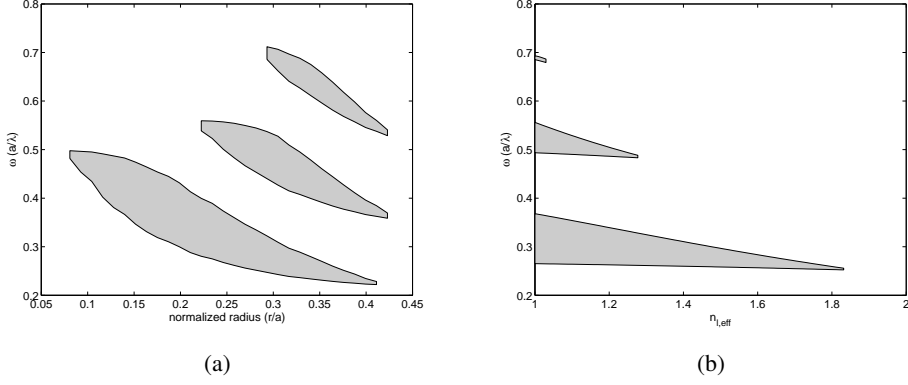
Figure 2.5: *Gap map of a pillar photonic crystal; a) TM band gap size as function of normalized radius with a background medium of n = 1 and b) TM band gap size as function of the effective refractive index of the background medium with r/a = 0.25.*

For refractive indices $n_{\text{l,eff}} \geq 1.8$, the index contrast is too small to open up a band gap.

Fig. 2.6 shows the 2D band diagram of a square lattice of pillars ($n_{\text{h,eff}} = 3.2641$ and $r/a = 0.25$) with $n_{\text{l,eff}} = 1.5236$ for the background medium. This value for $n_{\text{l,eff}}$ corresponds to the optimized polymer layer stack, which will be described in section 2.4. The TM band gap ranges from 0.258 to 0.294. The lattice constant of a photonic crystal with the center frequency corresponding to $\lambda = 1550$ nm should now be $a = \lambda \omega_c = 1550 \cdot 0.276 \simeq 427$ nm and the radius $r = 0.25a \simeq 107$ nm. The TM band gap ranges from $\lambda_{\text{min}} = a/\omega_{\text{max}} \simeq 1452$ nm to $\lambda_{\text{max}} = a/\omega_{\text{min}} \simeq 1655$ nm. Although the photonic band gap is clearly reduced in size, it is large enough for the intended applications operating in the EDFA window (1530 − 1570 nm).

2.2.3 The light line

In the normal direction, light is confined by total internal reflection (TIR). In a band diagram, the light line marks the continuum of modes that are supported by the claddings of the photonic crystal slab. In a homogeneous medium, the dispersion relation is given by

$$\omega(k) = \frac{ck}{n} \tag{2.13}$$

For a membrane-type photonic crystal, where the guiding slab is suspended in air, the light line is given by the dispersion relation of air, i.e. $\omega(k) = ck$. However, in the case of a deeply etched photonic crystal, the cladding layers as well as the guiding
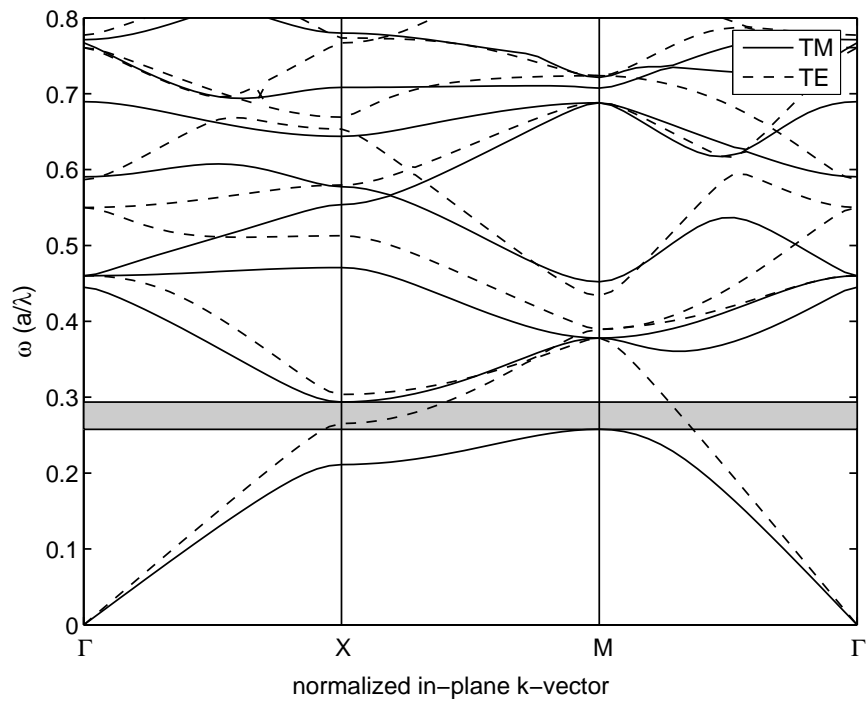
Figure 2.6: *2D band diagram of a square array of pillars (n = 3.2641) in a background of n = 1.5236 with r/a = 0.25. The solid curve represents TM modes whereas the dashed curve represents TE modes. The grey area indicates the TM stop gap between the first and the second band.*

(a)   (b)
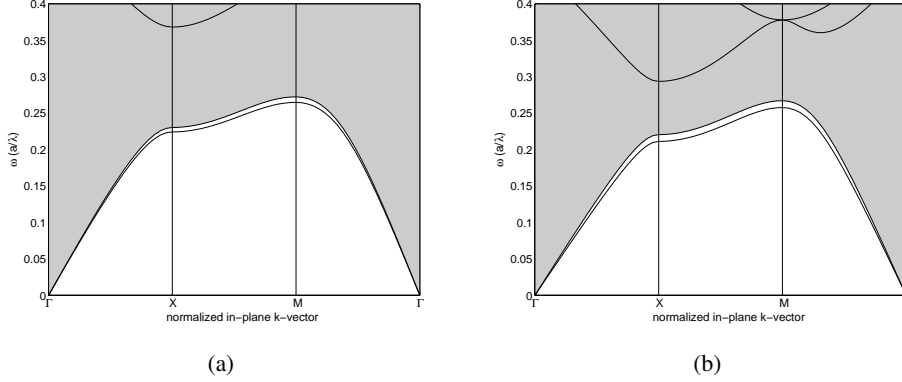
Figure 2.7: *Band diagrams of defect-free photonic crystals a) in air, and b) in a polymer layer stack. In these graphs, only the TM bands are represented. The lower boundary of the grey area is the light line. The grey area represents all radiation modes of the claddings.*

layer have a modulated refractive index. Then, the light line is given by the lowest frequency band of the cladding layers [5].

For bands lying beneath the light line, the modes are confined inside the guiding layer, but decay exponentially into the claddings, analogous to TIR in homogeneous slabs. Modes above the light line have a large out-of-plane *k*-vector. They are not confined to the slab and they couple to the radiation modes in the claddings.

In our InP-based technology platform, the core photonic crystal consists of In-GaAsP pillars in an air background, whereas the cladding photonic crystal consists of InP pillars in the same background. Because the vertical index contrast between InGaAsP and InP is low, the respective band diagrams are close in frequency.

For the pillar-based photonic crystal embedded in a polymer layer stack, although the lateral index contrast is lower, the vertical index contrast is higher than for pillars in an air background. The core photonic crystal consists of InGaAsP pillars in a high-index polymer, whereas the cladding photonic crystal is that of InP pillars in a low-index polymer. Hence, the frequency difference in the band diagrams of core and cladding is somewhat larger than it is for the pillars in air. However, the band gap frequencies of the core photonic crystal are all inside the continuum of cladding modes, implying possible coupling to the radiation modes.

Both for the pillars in air and for the pillars in polymers, the defect Bloch modes have a component that is above the light line of the cladding. In the next section, where we will design the photonic crystal waveguides, we will omit the light line from the

2D band diagrams, for clarity of the graphs. However, the influence of the Bloch mode components above the light line will be discussed in more detail in section 2.4.3.

2.3 In-plane confinement

In the previous section, we reviewed the basic properties of infinite, defect-free photonic crystals. By adding defects to a photonic crystal, one can create in-plane confinement of the light. A waveguide can be created in a planar photonic crystal by changing either the refractive index or the radius of a row of pillars in the bulk lattice. Since we are bound to the material stack, the only practical possibility to tailor the crystal is to vary the pillar radius.

Fig. 2.2 in section 2.1.2 showed a photonic crystal of high-index pillars in a low-index background medium. To find the modes that are guided along the line defect, we calculate the bands of the super cell that is indicated in the figure. The super cell is periodic in the ΓX direction, the propagation direction along the PhC waveguide (see Fig. 2.3). By projecting the band diagram onto the ΓX edge of the Brillouin zone we can include all in-plane directions in a graph of just the ΓX direction. In this way, we find the Bloch modes that are allowed to propagate along the photonic crystal waveguide but that are confined in-plane by the surrounding photonic crystal.

The criteria for the design of a photonic crystal waveguide, are the following:

- We want to avoid the excitation of slow modes, since such a mode is not suitable for transporting light. Therefore, modes with a large group velocity are aimed for. The group velocity is defined as $v_g = d\omega/dk$, so this criterion implies that the slope of the guided mode in the band diagram has to be large.

- The dispersion should be low, so the group velocity should be constant over a reasonable bandwidth.

- The bandwidth of the waveguide should be large enough for practical applications.

- We aim for excitation of even modes, having an amplitude that has mirror symmetry in the plane through the axes of the defect pillars.

In this section, the design of photonic crystal waveguides is described, based on these design constraints. We will start by optimizing the radius of the defect pillars for the case of pillars in air and for the pillars in the optimized layer stack. To this end, the radius of the line defect pillars is increased, since larger pillars are more stable and

have a higher effective refractive index. To find the optimal defect radius, the band diagrams of PhC waveguides are calculated for varying defect pillar radius, and we inspected the defect modes that appeared in the band gap. The band diagrams are obtained by 2D band solver calculations, where the EIM is used to account for the third dimension.

2.3.1 InP-based pillars without polymer layer stack

We start by examining the photonic crystal lattice of pillars in air. The projected band diagrams of two different PhC waveguides in this lattice are shown in Fig. 2.8. The line defects consist of pillars with defect radius $r_d = 170$ nm (Fig. 2.8(a)) and pillars with $r_d = 210$ nm (Fig. 2.8(b)). Both PhC waveguides meet the requirements that we defined previously. The grey areas represent the projected bands of the lattice modes. These are the modes that are allowed to propagate in the bulk lattice, for which a photonic crystal waveguide can not support a guided mode that is confined to the line defect. They are identical in both cases, since the PhC lattice in which the waveguide is created, is kept the same.

In the band diagram of Fig. 2.8(a), we can distinguish three modes that are caused by the introduction of the line defect in the bulk lattice. One waveguide mode is lower in frequency than the first band of the bulk lattice. This is an index-guided mode, due to the higher average index of the line defect as compared to the bulk lattice. Furthermore, there are two waveguide modes in the band gap between the first and the second band of the bulk lattice. The mode with monotonically increasing frequency is an odd mode, as can be seen in the E_y field plot of Fig. 2.9(a). The mode that is monotonically decreasing in frequency is an even mode, see the corresponding E_y field plot in Fig. 2.9(b).

The bulk photonic crystal was designed to have its center frequency corresponding to the wavelength $\lambda = 1550$ nm, as represented in the band diagram by the dash-dotted line. At this frequency, the slope of the odd mode is close to zero, implying that the group velocity is very small. This means that the odd mode is in the so-called slow-light regime, where it propagates extremely slowly. At the crossing of the even and the odd mode, the waveguide mode becomes hybrid. Excitation at this frequency should be avoided.

On the other hand, the even mode has a large and constant slope around $\lambda = 1550$ nm. This regime is favorable for waveguiding purposes, since the group velocity is high and the wavelength dispersion is low over a considerable bandwidth. If we are able to excite only the even mode, the frequency range that could be used for waveguiding runs at least from $\omega = 0.30$ to $\omega = 0.33$, corresponding to a wavelength

(a)

(b)
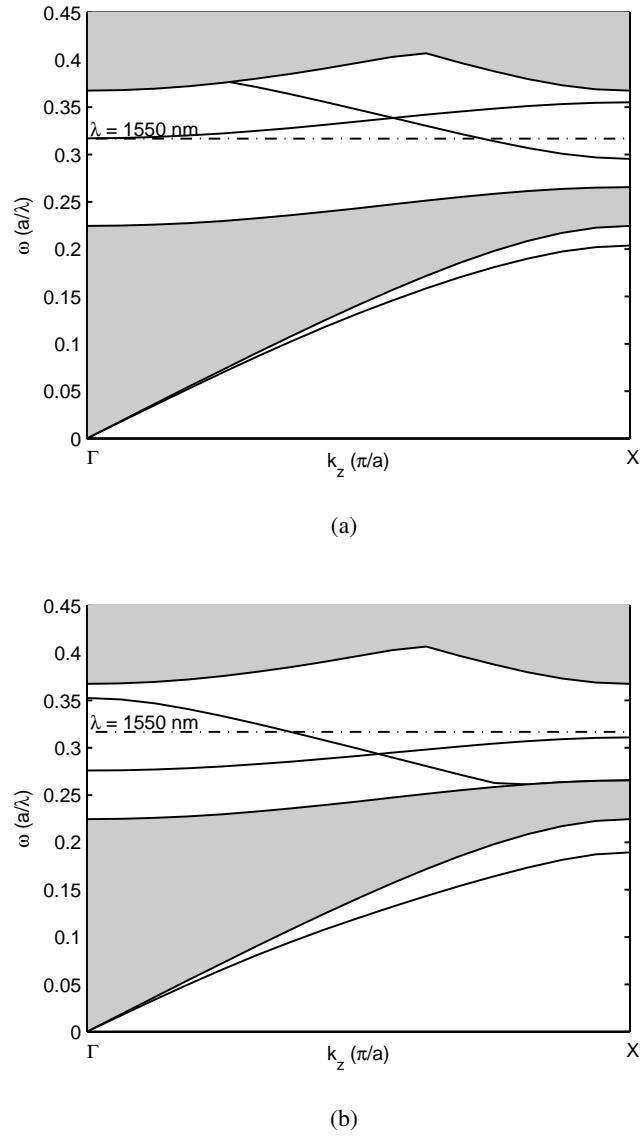
Figure 2.8: *Projected band diagrams of a photonic crystal waveguide based on pillars ($n_{h,eff} = 3.2641$) in air. The photonic crystal waveguide consists of a line defect with a) $r_d = 170$ nm and b) $r_d = 210$ nm in a background crystal with lattice constant $a = 491$ nm and $r = 123$ nm.*
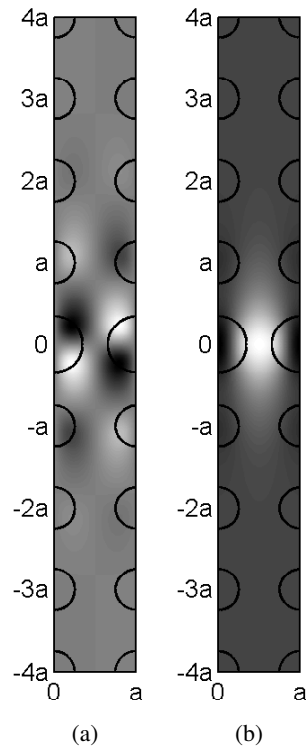
Figure 2.9: *Field plots of a) the odd waveguide mode, and b) the even waveguide modes, both for a photonic crystal waveguide based on pillars ($n_{h,eff} = 3.2641$) in air. The photonic crystal waveguide consists of a line defect with $r_d = 170$ nm in a background crystal with lattice constant $a = 491$ nm and $r = 123$ nm.*
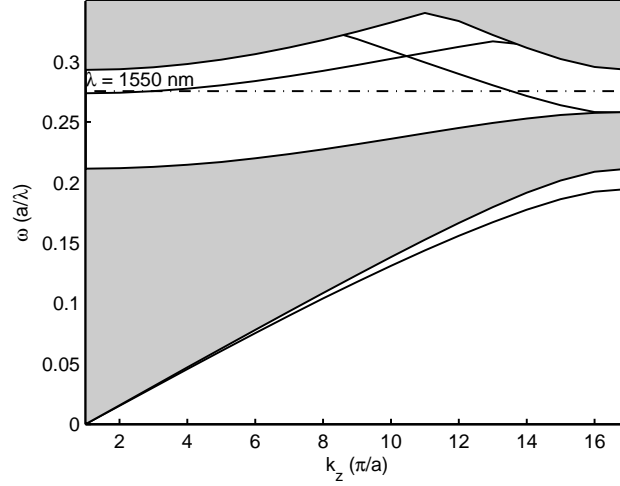
Figure 2.10: *Projected band diagram of a photonic crystal waveguide based on pillars ($n_{h,eff}$ = 3.2641) in a polymer layer stack ($n_{l,eff}$ = 1.5236). The photonic crystal waveguide consists of a line defect with r_d = 155 nm in a background crystal with lattice constant a = 427 nm and r = 107 nm.*

range from 1.49 – 1.64 μm.

By increasing the radius of the line defect pillars, the waveguide modes are pushed down in frequency. At some point, the odd waveguide mode is completely below the center frequency of the band gap. This is illustrated in fig. 2.8(b), where the defect pillar radius r_d = 210 nm. This design therefore avoids any problems with possible excitation of the odd mode. The even mode still has the desired properties, but as the distance between defect pillars in the waveguide becomes small (71 nm), realization of these waveguides might be difficult (see chapter 4). Both designs will be tested in the realization.

2.3.2 InP-based pillars with polymer layer stack

As was discussed in section 2.2, implementation of the polymer layer stack between the pillars reduces the lateral index contrast, causing a smaller band gap and smaller dimensions of the crystal for operation at wavelength λ = 1550 nm. Fig. 2.10 shows the projected band diagram of a photonic crystal waveguide based on III-V pillars in a polymer layer stack.

For this PhC waveguide, the lattice constant is a = 427 nm, the bulk lattice radius

Table 2.2: *Overview of design parameters of the photonic crystal waveguides.*

(a)		(b)	
pillars in air		pillars in a polymer stack	
a	491 nm	a	427 nm
r	123 nm	r	107 nm
r_{d}	170 nm	r_{d}	155 nm
	210 nm		

is $r = 107$ nm and the optimized radius of the defect pillars is $r_{\mathrm{d}} = 155$ nm. Apart from the band gap size, the band diagram is comparable to that in fig. 2.8(a) for pillars in air with $r_{\mathrm{d}} = 170$ nm. Again, the waveguide mode decreasing in frequency is an even one, whereas the mode increasing in frequency belongs to an odd mode. Due to the smaller band gap and the smaller lattice dimensions, no defect radius can be found for which the odd mode vanishes as was the case for pillars in air with $r_{\mathrm{d}} = 210$ nm. The frequency range over which the slope of the even guided mode is large runs from 0.265 to 0.290, corresponding to a wavelength range from $1.47 - 1.61$ µm.

In this section, the designs for photonic crystal waveguides were presented. Table 2.2 summarizes the design parameters for the pillars in air and for the pillars embedded in a polymer layer stack.

2.4 Out-of-plane confinement

In the classical ridge waveguides, light is confined by total internal reflection (TIR). Light is reflected at a transition from a high-n to a low-n medium if the angle of incidence is smaller than the critical angle. In a classical waveguide, this mechanism is exploited for the in-plane as well as for the out-of-plane direction. In a photonic crystal waveguide, as described in the previous section, the in-plane confinement by TIR is replaced by in-plane confinement by the photonic band gap properties of the PhC. However, the out-of-plane confinement is still created by TIR.

After the semiconductor pillars are etched, initially they are surrounded by air. Due to the absence of a guiding layer of high refractive index between the pillars, there is a lack of optical confinement. This lack of guiding translates into high out-of-plane propagation losses. In this section we will investigate the possibility of creating confinement between the III-V pillars by implementing a polymer layer stack.

Although polymers are available in a relatively wide range of refractive index, our choice is limited by further demands such as transmission and absorption spectra, chemical stability etc. Section 4.4 elaborates on the selection of the polymers that are used. For the moment, it suffices to say that the selected polymers have indices $n_{l,1} = 1.64$ and $n_{l,2} = 1.38$. As we saw in sections 2.2.2 and 2.3.2, although the increase in $n_{l,\text{eff}}$ does have an effect on the size and center frequency of the photonic band gap, the design window is large enough for applications in devices such as PhC waveguides.

Optimal coupling between the semiconductor and polymer layer stacks is achieved when the mode profiles of the fundamental guided TM modes of both stacks are matched. Given the indices of the polymers, we will optimize the layer thickness of the high-index polymer and the etch depth of the pillars. The optimization is done with 2D calculations of a vertical cross section. First we study the coupling between the semiconductor and the polymer waveguide for a single transition. Then we investigate the periodic structure of III-V and polymer stacks. This 2D calculation is done by taking a vertical cross section through the center of the PhC waveguide pillars. This structure effectively represents a 1D grating. Finally we analyse the Bloch modes in a 1D grating and link them to the band diagrams of the photonic crystal waveguides. For convenience, we will use the acronyms PiA for pillars surrounded by air, PiP for pillars in a polymer layer stack and PiUP for pillars in a uniform polymer layer with a refractive index equal to the effective refractive index of the polymer layer stack.

2.4.1 Single transition

We start the optimization of the polymer layer stack by studying one single transition from the III-V to the polymer layer stack as shown in Fig. 2.11. In order to find the optimal design parameters, we perform an FDTD simulation of the coupling to find the transmission and reflection of the transition.

In an FDTD simulation, a calculation window has to be defined, with PMLs at the window boundaries (see section 2.1.4). In these simulations, the InGaAsP guiding layer $d_{h,\text{core}} = 0.5$ μm thick and the InP top cladding has a thickness of $d_{h,\text{top}} = 1$ μm. The calculation window limits the InP bottom cladding to $d_{h,\text{bottom}} = 5$ μm and the air top cladding to $d_{\text{air}} = 4$ μm. In this way, the calculation window is large enough not to influence the calculation of the guided modes in the exciter and sensors. PMLs are placed at the boundaries of the calculation window.

The etch depth d_{etch} is taken to penetrate the full III-V layer stack at first instance. Within the calculation window this means that

$$d_{\text{etch}} = d_{l,\text{top}} + d_{l,\text{core}} + d_{l,\text{bottom}} \tag{2.14}$$
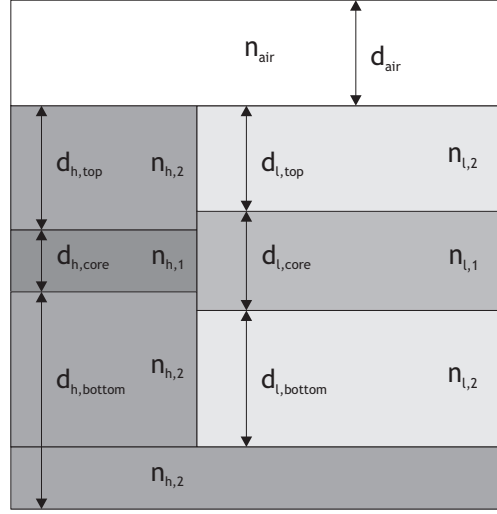
Figure 2.11: *Structure for the FDTD simulation of a single transition from III-V layer stack to polymer layer stack.*

Furthermore, the polymer waveguide core is first assumed to be centered at the center line of the InGaAsP core. The coupling transmission is calculated by taking the ratio of the power in the fundamental guided TM mode at the output polymer waveguide to the power in the fundamental guided TM mode at the input III-V waveguide. The reflection from the interface into the fundamental guided TM mode is also taken into account; since the photonic crystal effect is based on resonances propagating back and forth in the structure, this light is not considered as being lost. The loss follows from the transmission T and the reflection R by the relationship

$$T + R + L = 1 \tag{2.15}$$

where L denotes the loss.

The coupling loss as a function of the polymer waveguide core thickness for the single transition is given in Fig. 2.12. If the polymer core thickness increases from 0.2 μm to 0.8 μm, the coupling loss steadily decreases because the mode profile of the polymer waveguide gets more confined to its core layer. This provides a better overlap with the mode of the InP/InGaAsP/InP waveguide. Increasing this thickness even more, however, reduces the coupling again, because the mode in the polymer waveguide starts to scale with the thickness. For polymer core thickness > 1.0 μm the polymer waveguide ceases to be single-mode, and light can be coupled into higher order modes too. Since these higher order modes destroy the in-plane photonic crystal
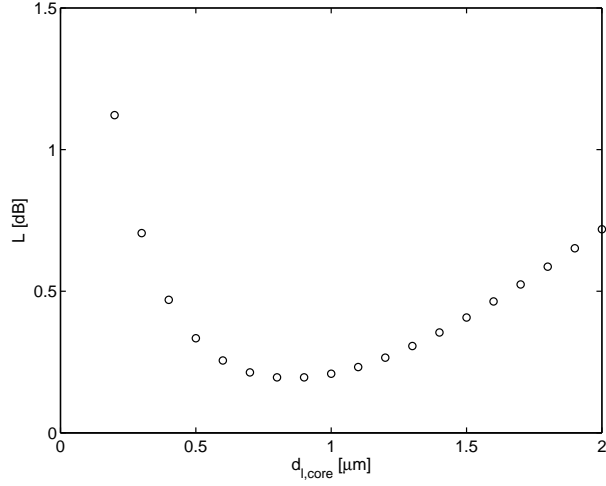
Figure 2.12: *Coupling loss as function of polymer core thickness of a single transition from semiconductor to polymer layer stack.*

properties, multi-mode operation should be avoided. The optimal polymer core layer thickness is thus $d_{l,core} = 0.8$ μm, resulting in ~ 0.2 dB loss. The allowable deviation is ± 0.1 μm for 0.01 dB extra loss.

In actual planar photonic crystals, the finite etch depth can induce leakage from the polymer slab waveguide to the InP substrate. The guided modes in the polymer core are in fact leaky modes. To limit the loss, the coupling of these modes to the InP substrate should be small enough, imposing a minimum required etch depth. Fig. 2.13 shows the total losses of the transition and propagation over 20 μm through the polymer slab waveguide as a function of the etch depth of the structure. The calculation is performed for different polymer core thicknesses. If the etch depth is large enough, there is no coupling of light to the InP substrate and thus the total loss is effectively constant and equal to the coupling loss at the transition. The etch depth should be at least 3.0 μm to prevent substrate leakage. With this etch depth and a polymer core thickness of 800 nm the propagation loss due to leakage is limited to ~ 1.5 dB/mm. For etch depth $d_{etch} \leq 3.0$ μm the losses rapidly increase due to this effect.

Fig. 2.14 shows the influence of an offset of the polymer waveguide with respect to the InGaAsP core. It gives an indication of the fabrication tolerance of the polymer layer stack implementation. For an offset of ± 100 nm, which seems technologically feasible, the excess loss is < 0.1 dB. This is an acceptable number.
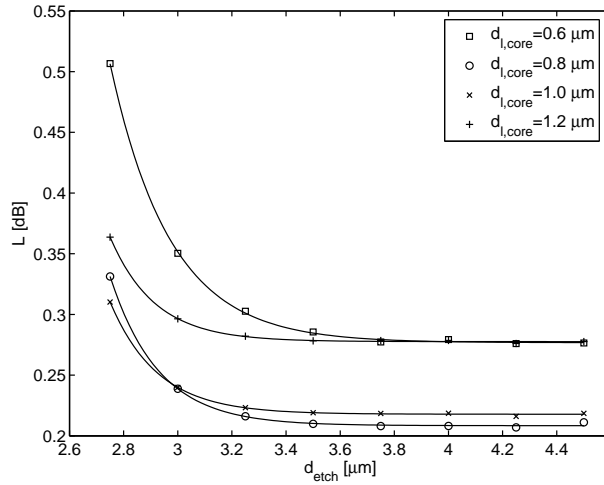
Figure 2.13: *Total losses of the transition and 20 μm propagation through the polymer slab waveguide as function of the etch depth. The solid lines represent a fit to an exponential model.*
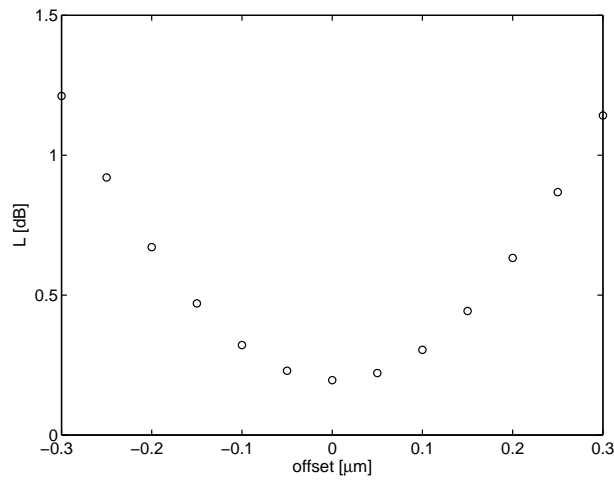
Figure 2.14: *Total losses of the transition and 20 μm propagation through the polymer slab waveguide as function of the transverse offset (where a positive offset corresponds to an offset toward the air region).*

37
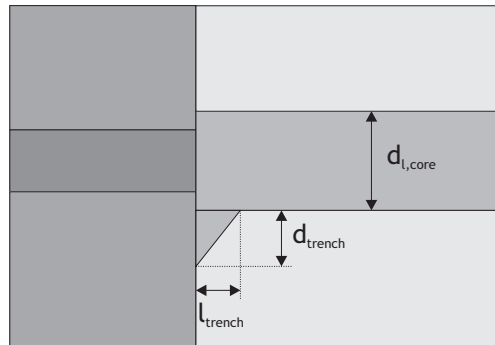
Figure 2.15: *Schematic representation of the structure that is used to simulate the influence of trenching of the low-index polymer on the transition loss.*

Another issue to keep in mind is possible trenching in the etching process of the polymer (see chapter 4). With trenching we mean that close to a semiconductor-polymer interface, the etching back of the polymer layers might be faster than on areas with only the polymer. In practice, trenching is worse for the cladding polymer. Therefore, we simulate the influence of trenching of the low-index polymer on the loss at the transition, as is schematically shown in Fig. 2.15.

In the simulation, the length and depth of the trench are varied. The trench is always assumed to have a triangular shape. The losses that are thus obtained are plotted in Fig. 2.16. As is expected, the losses increase with increasing trench dimensions. However, the graph shows that the tolerance for trenching is much higher than it is for an offset in vertical direction; even with unrealistically large trenches of 1 µm depth and 0.5 µm length, the extra loss is only 0.05 dB. The explanation for this small effect is that the length of the disturbance is well below the wavelength in the polymer layer stack (i.e. $\sim$ 1 µm), so that the mode easily passes through.

Based on the simulations on a single transition, we have optimized the parameters for the polymer layer stack and we obtained an estimation of the fabrication tolerances. In the following section we will investigate the performance of this layer stack in a periodic structure.

2.4.2 Multiple transitions

The periodicity of a photonic crystal can either enhance or reduce the out-of-plane scattering due to constructive or destructive interference, respectively [43]. Therefore, the polymer layer stack designed in the previous section should be tested in a structure with multiple transitions. The simulated structure is a one-dimensional periodic
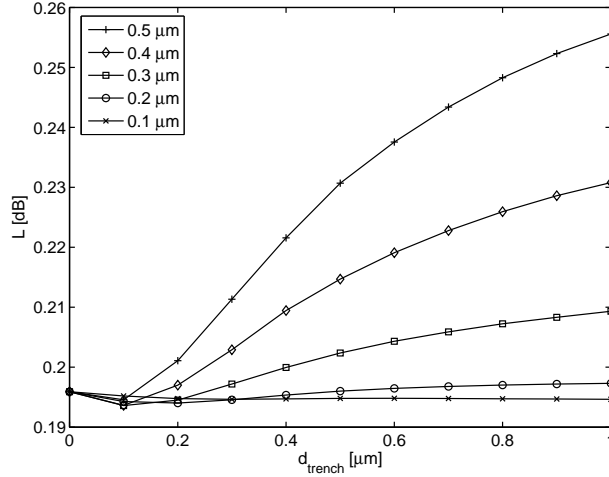
Figure 2.16: *Losses as a function of the length and the depth of the trench.*

grating of semiconductor pillars interrupted by low-index regions consisting of either air, a polymer layer stack or a uniform polymer. In this way, we invesigate if the polymer waveguide causes a significant reduction of the out-of-plane losses. For the simulations in this section, the software package CAMFR is used (see section 2.1.3).

The structure that is simulated, is schematically drawn in Fig. 2.17. It consists of an input waveguide that is 10 μm long, followed by a one-dimensional grating of N periods and an output waveguide of again 10 μm length. One period of the grating consists of a high-index region with a length of $l_h = 310$ nm and a lattice constant $a = 427$ nm. The choice for the geometrical parameters is based on the photonic crystal waveguide parameters for pillars in a polymer stack (see section 2.3.2), for the PiP structures as well as for the PiA and the PiUP structures. The semiconductor layer stack is the same as before (see Fig. 1.2).

At the input waveguide, the fundamental guided TM mode is excited. T is the transmission from that mode to the fundamental guided TM mode at the output wave-guide. R is the reflection to the fundamental TM mode at the input waveguide. From these two coefficients, the loss is again calculated by Eq. 2.15. The simulation results are averaged over 30 to 60 periods to average out oscillations caused by the finite grating length.

Fig. 2.18 shows the transmission, reflection and loss of the grating for varying polymer core thickness. The reflection is nearly constant over the full range of poly-
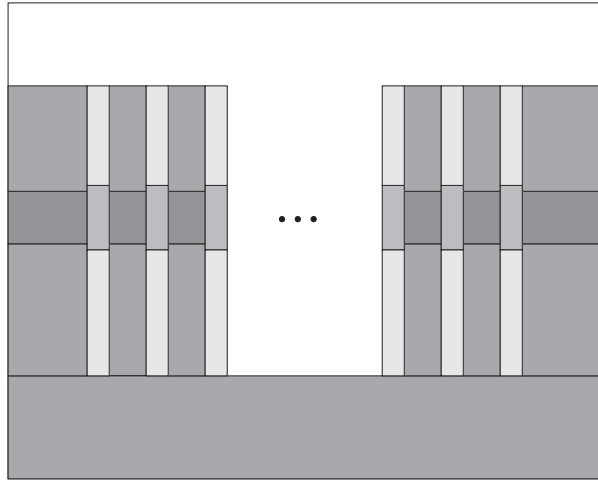
Figure 2.17: *Schematic structure of the 1D grating used in the simulations.*

mer core thickness, and it corresponds with the Fresnel equations for the reflection at an interface. The loss curve confirms the optimized core thickness of the previous simulations on a single transition. However, the loss is low over a larger range of polymer core thickness due to the periodicity of the structure. Light that is radiated out-of-plane at a semiconductor-polymer interface can be recaptured at the next III-V stack, whereas in case of a single transition it is lost without a chance of being recaptured.

Fig. 2.19(a) shows the calculated reflection, transmission and loss of the PiA structure as a function of the etch depth. For etch depth > 3 µm, the loss is between 40% and 50%, and this value increases for smaller etch depth. If we implement the polymer layer stack with optimized core thickness, the calculated transmission, reflection and loss are as shown in fig. 2.19(b). The optimized polymer stack reduces the loss to ∼ 5% for etch depths > 3 µm, a reduction of an order of magnitude with respect to the PiA.

Finally, we consider the case where the regions between the pillars are filled with a uniform polymer layer, having a refractive index equal to that of the effective refractive index of the full polymer layer stack (PiUP). The results are shown in Fig. 2.19(c). The loss is now in the order of 10%, which is twice as much as for the PiP. It can be concluded that the reduction in out-of-plane loss is not only caused by the change in lateral refractive index contrast, but also to the presence of optical confinement between the pillars.

Fig. 2.20 shows the losses in the three cases as a function of the number of periods
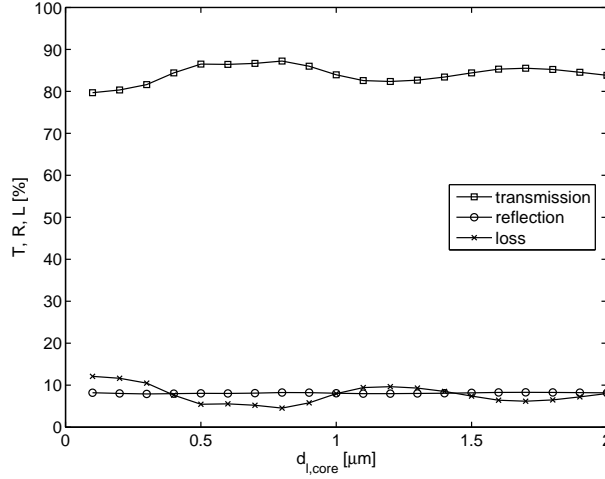
Figure 2.18: *Transmission, reflection and loss as a function of polymer core thickness for a one-dimensional periodic structure. All values are averaged over 30 to 60 periods to average out oscillations that are due to the finite grating length.*

N of the grating. The losses are plotted in dB. From the linear fits, we can get an estimation of the propagation losses in the transmission window of the grating. For the pillars in air, the estimation obtained in this way is ~ 10.9 dB/mm. The losses are reduced to ~ 7.0 dB/mm if a uniform polymer is introduced between the pillars. By applying the optimized polymer layer stack, the losses are as low as ~ 0.3 dB/mm. From the estimated propagation losses it becomes clear that a reduction in index contrast between pillars and surrounding medium reduces the losses. Presumably this is because the diffraction angle is smaller, so a larger amount of the light is recaptured by the next pillar. However, the fact that *optical guiding* is introduced between the pillars induces a huge reduction in propagation losses.

The losses in the first few periods in Fig. 2.20 are due to the transition from a ridge waveguide mode to a grating Bloch mode. These transition losses are ~ 2 dB for PiA, decreasing to ~ 0.4 dB for PiUP and as small as ~ 0.2 dB for PiP. The reduction in transition losses can also be contributed to the reduction in diffraction angle.

In this section we have optimized the thicknesses of the polymer layers. We have seen that the propagation losses can be significantly reduced by implementation of the polymers. In the next section we will link these results to the Bloch modes that were found for the photonic crystal waveguides.

(a)

(b)

(c)
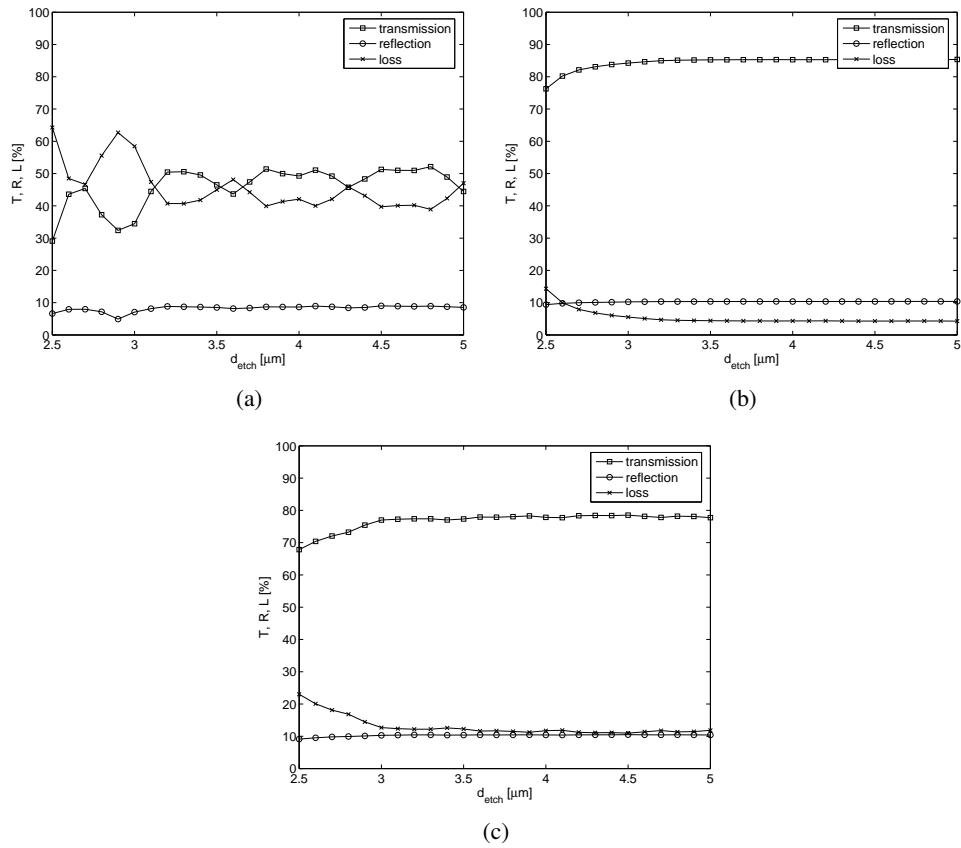
Figure 2.19: *Transmission, reflection and loss as a function of etch depth, a) for a grating in air, b) for a grating with a polymer layer stack with $d_{l,core} = 800$ nm and c) for a grating with a uniform polymer with $n = n_{l,eff}$.*
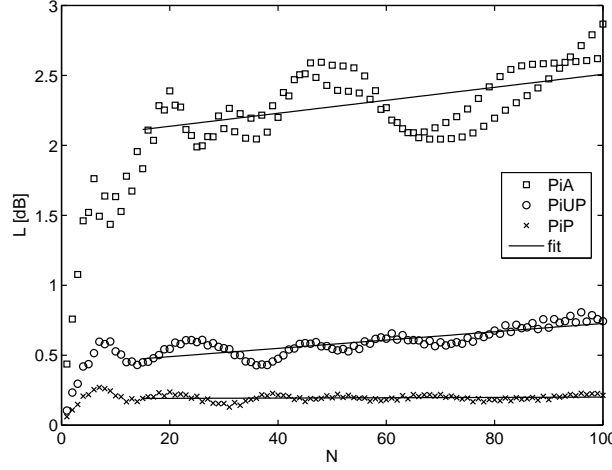
Figure 2.20: *Loss as function of the total number of periods N of the grating for three different fillings between the semiconductor pillars: without polymers, with a uniform polymer with $n = n_{\mathrm{l,eff}}$, and with the optimized polymer layer stack and etch depth 3 µm.*

2.4.3 Bloch mode analysis

The dispersion diagram of a Bloch mode is periodic, where the spatial frequencies are an integer multiple of $\mathbf{G} = (2\pi l/a)\hat{x} + (2\pi m/a)\hat{z}$ apart. Because of the periodicity of the dispersion diagram and the symmetry of the lattice, the band diagram of the irreducible Brillouin zone gives all the relevant information on the optical frequencies of the modes. In fact, the band diagram of the first Brillouin zone of the 1D grating is repeated infinitely in positive and in negative direction of $\mathbf{k}$. Fig. 2.21 shows the projected band diagram of a PhC waveguide, extended over one-and-a-half Brillouin zone. Every Bloch mode consists of spatial frequencies from different Brillouin zones and it can thus be written as

$$E(y,z) = \sum_{m=-\infty}^{\infty} c_m(y)e^{j(k_z+2\pi m/a)z} \tag{2.16}$$

Not all spatial frequencies are equally strong represented in an excited Bloch mode. By Fourier transforming the field of an actual excited Bloch mode, the relative strengths of the spatial frequency components can be found [44].

To this end, we investigate the guided Bloch mode in the 1D grating simulated in the previous section. By taking the 2D Fourier transform of the field profile, we

43
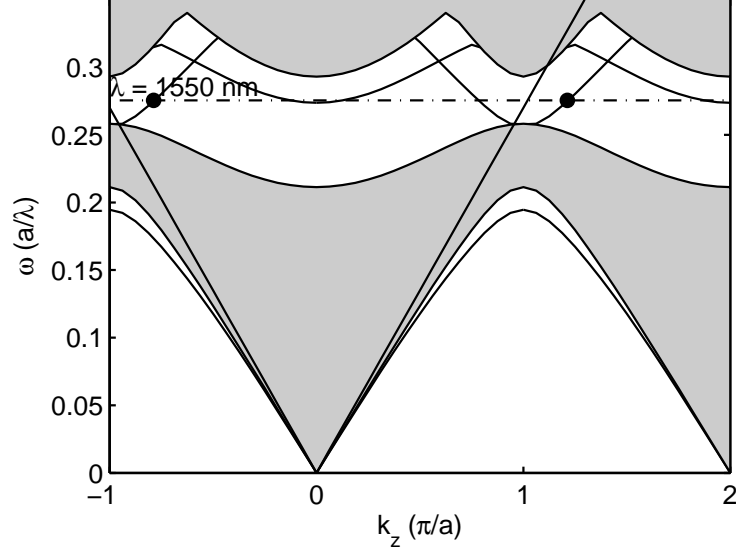
Figure 2.21: *Projected band diagram of a PhC waveguide, extended over one-and-a-half Brillouin zone. It corresponds to the PhC waveguide of pillars in polymers, where $r = 107$ nm, $a = 427$ nm and $r_{\mathrm{d}} = 155$ nm. The dots indicate the Fourier components of the Bloch mode in subsequent Brillouin zones.*

obtain the relative strengths of its spatial frequencies k_z (in propagation direction) and k_y (out-of-plane).

The complex field amplitude of the Bloch mode that is excited in a 1D grating is calculated using FDTD calculations (see appendix A). The parameters used for the lengths of semiconductor and low-index sections in the grating are the same as in the previous section. The grating length is kept at 50 periods. PMLs are placed at the boundaries of the calculation window. The input waveguide is excited with the fundamental guided TM mode in continuous-wave operation at a wavelength $\lambda = 1550$ nm. Fig. 2.22 shows the field amplitudes after 500 fs (when the field is stable) for the three different cases: pillars in air, pillars in a uniform polymer layer and pillars in the optimized polymer layer stack. From the figures it is qualitatively visible that for the PiA, the radiation of light to the air and to the substrate is higher than for the other two cases. The PiP case seems to have the least radiation.

Taking the Fourier transforms of the field amplitudes provides us with the relative strengths of the spatial frequencies. In the field plots of Fig. 2.22 we encounter three

(a)

(b)

(c)
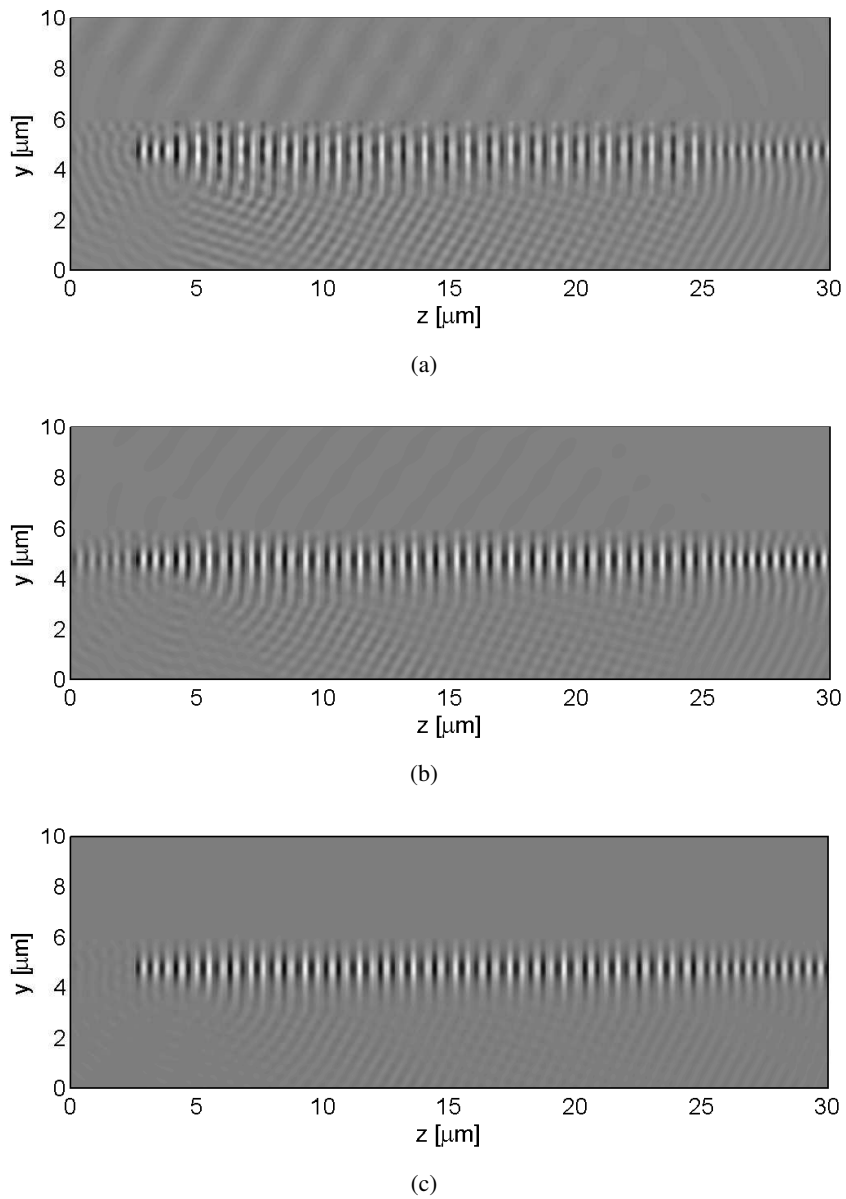
Figure 2.22: *Field amplitudes in a 50-period 1D grating after 500 fs for a) pillars in air, b) pillars in a uniform polymer layer, and c) pillars in the optimized layer stack.*

regions; the field at the input and output ridge waveguides, the field inside the grating and the fields at the transitions between both types of waveguides. From Fig. 2.20 we learned that the transition from a ridge waveguide mode to a grating Bloch mode spans about ten periods. Since we are only interested in the Fourier components of the grating Bloch modes, we do not take into account the first and the last ten grating periods when taking the Fourier transforms. The field over the center 30 periods of the grating is Fourier transformed to find the strengths of the spatial frequency components.

The results of the 2D Fourier transforms of the three cases are shown in Fig. 2.23. Both k_z and k_y are expressed in (π/a). The light lines of air and InP at $\lambda = 1550$ nm are plotted in the graphs as semicircles, where the light line of air is only represented for positive k_y and that of InP is only represented for negative k_y. The full circle represents a medium with a refractive index equal to the average refractive index n_{av} of the InP grating claddings:

$$n_{av} = \frac{n_{h,2} \cdot l_h + n_{l,2} \cdot (a - l_h)}{a} \tag{2.17}$$

This light cone only approximates the **k**-vectors of cladding modes, because the claddings are no homogeneous media with this average refractive index. All modes that are excited in the grating either belong to the guided Bloch mode without an out-of-plane component (i.e. modes having only a k_z component) or they are out-of-plane modes on one of the light lines belonging to the claddings, the air above or the InP below. The k_z values of all modes are determined by the Bloch mode of the grating, and the k_y values of the radiation modes follow from the light cones of the corresponding media. The peaks in the Fourier spectrum that are not on one of the light lines nor on the $k_y = 0$ axis, are ghost peaks that are probably due to the finite step size in the FDTD calculation of the complex field amplitude.

From Fig. 2.23(a) we can see that the PiA has relatively strong radiation mode components. On the air light cone, a strong peak visualizes the radiation into the air, as we could see from the field plot in Fig. 2.22(a). On the InP light cone there are three peaks, and indeed in the field plot the InP substrate shows a more complicated radiation pattern with interfering plane waves. The presence of the peaks on the cladding light cone shows that coupling to the radiation modes is possible via intermediate coupling to the cladding modes. The cladding modes do not exactly coincide with the cladding light cone due to the fact that this light cone is an approximation based on the weighted average refractive index of the claddings.

For the PiUP, for which the spatial Fourier transform is given in Fig. 2.23(b), the strengths of the components in the first Brillouin zone are significantly reduced, although they are still present (note the difference in greyscale in the Fourier spectrum). Finally, Fig. 2.23(c) shows the Fourier spectrum of the PiP. The peaks on the light

cones have nearly vanished from the spectrum.

The peaks belonging to the k_z in the first Brillouin zone have the largest contribution to the out-of-plane losses. In Fig. 2.24 the relative strengths of these peaks are compared. The curves are normalized to the peak belonging to the guided Bloch mode, i.e. one at $k_y = 0$. All three curves belong to the spatial frequency of the Bloch mode with $-\pi/a \leq k_z \leq 0$ (the peaks in the positive half of the first Brillouin zone are ghost peaks). The actual k_z value is slightly different in each case, as the Bloch mode depends on the refractive indices of the grating. In the graph, the reduction in the coupling to out-of-plane radiation modes is clearly visible.

Apart from the coupling to radiation modes by intermediate coupling to the cladding modes, there is also a coupling mechanism that is probably due to the penetration of the evanescent tails of the guided Bloch mode into the InP substrate. This peak is the one on the InP light cone with $\pi/a \leq k_z \leq 2\pi/a$. Its $|\mathbf{k}|$ value is too large to couple to the cladding modes. The implementation of the polymer layer stack reduces this out-of-plane loss mechanism because of the smaller diffraction angle. By increasing the etch depth further into the InP substrate, the direct coupling to the InP substrate via the evanescent tails will vanish completely.

The polymer layer stack maximizes the coupling to the Fourier components with high in-plane k-vectors, thereby minimizing the coupling to $\mathbf{k}$-vectors with a small k_z that are able to couple to the radiation modes. Recalling the band diagram in Fig. 2.21, the Bloch components above the light line are strongly reduced and effectively, we excite a Bloch mode with only components outside the light cone. This mechanism enables us to design pillar-based PhC components with extremely low propagation losses.

2.5 Conclusions

In this chapter, some basic concepts of photonic crystals were introduced. It has been shown that line defects in 2D photonic crystals can act as waveguides. The photonic band gap properties of the crystal induce the in-plane confinement, whereas out-of-plane confinement is due to total internal reflection. It has been shown that the implementation of a polymer layer stack between the pillars can significantly reduce the propagation losses of PhC waveguides. Because of these very low losses, pillar-based photonic crystals form a strong platform for integration of a new series of devices in classical PICs.
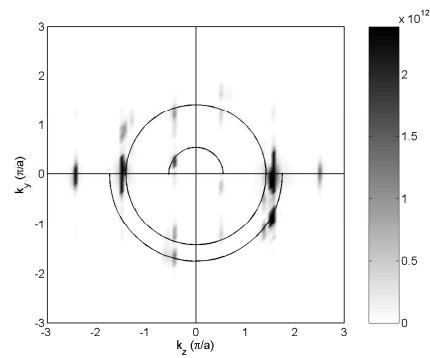
(a)
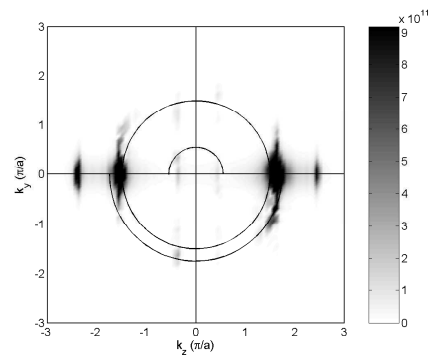
(b)
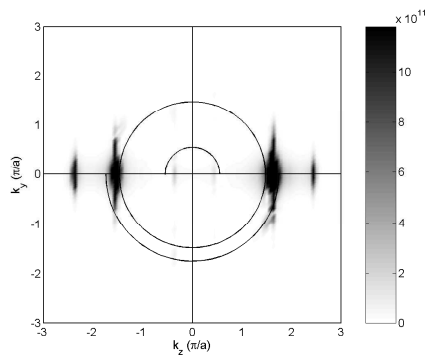
(c)

Figure 2.23: *Fourier transform of the field amplitudes over the center 30 periods in a 50-period 1D grating after 500 fs for a) pillars in air, b) pillars in a uniform polymer layer, and c) pillars in the optimized layer stack. The grey scale is adapted to improve the visibility of the relevant spectral peaks.*

48
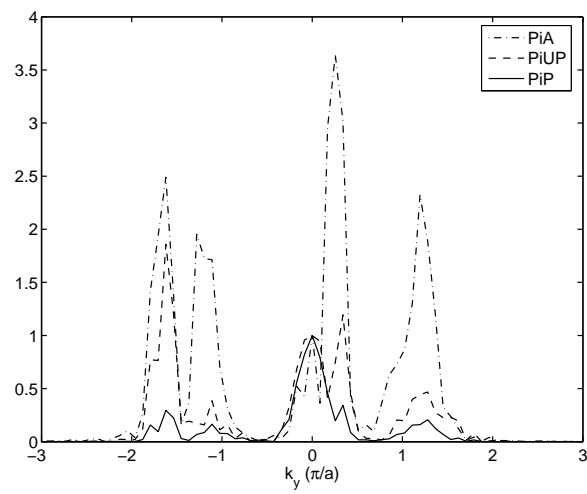
Figure 2.24: *Fourier spectrum along the line of constant k_z belonging to the grating Bloch mode in the first Brillouin zone with $-\pi/a \leq k_z \leq 0$ for pillars in air, pillars in a uniform polymer and pillars in the optimized polymer layer stack.*

Chapter 3
Design of integrated photonic crystal components

For photonic crystal-based components to be competitive with classical components, the insertion loss is the most important issue. The insertion loss consists of the propagation loss and the transition losses between the classical waveguide and the PhC component. In the previous chapter it was shown by out-of plane simulations that low-loss propagation is possible for pillar-based photonic crystals in a structure with low vertical index contrast. The design parameters of the photonic crystal waveguides were optimized for low propagation loss. In the applications, also the coupling between classical ridge waveguides and photonic crystal waveguides has to be optimized. This chapter focuses on the application of photonic crystals in photonic integrated circuits.

In section 3.1, the simulation method is described. The optimization of the coupling between classical ridge waveguides and PhC waveguides is described in section 3.2. The polarization-selective nature of photonic crystals can be exploited in their application in polarization components. In section 3.3 the design of TE and TM polarization filters is described. Conclusions are drawn in section 3.4.
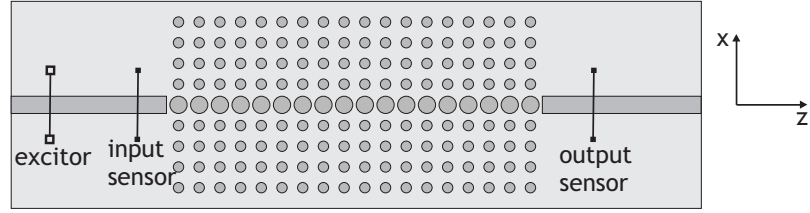
Figure 3.1: *Definition of a structure for FDTD simulations.*

3.1 Simulation method

Using the Finite Difference Time Domain (FDTD) method, we can study the transmission and the reflection of a photonic crystal waveguide as a function of wavelength (or frequency, since these are inversely proportional). The available FDTD method can handle 2D as well as 3D simulations [41]. The 2D simulations can be used as a development tool, to study the parameter dependencies and obtain a first design, while the more accurate but time consuming 3D simulations can be used for final checking and adjusting that design.

In 2D simulations we use the EIM to account for the third dimension. Fig. 3.1 shows an example of a structure that is simulated. It consists of an input waveguide, a PhC component and an output waveguide. The minimum length of a simulated PhC component is 20 periods, since the transition between a waveguide mode and the Bloch mode of the photonic crystal takes ∼ 10 periods (see section 2.4.2). The length of the PhC components is limited to 40 periods, in order to have reasonable calculation times. The access waveguides have a length of $\geq 7.5a$. On both sides of the PhC waveguides, 10 lattice periods are included in the simulations. These values result in a maximum calculation window of 27 μm length and 10.8 μm width.

To ensure that the grid of the FDTD calculation matches the periodicity of the PhC lattice, it is chosen to be $a/20$. This discretization grid results in the same calculation accuracy as a grid of $a/40$, so it is accurate enough while calculation times are relatively small. To maintain the symmetry of the structure, the calculation window is always an integer multiple of the lattice constant.

The input waveguide is excited with the fundamental guided TM or TE mode, as calculated by a mode solver that is implemented in the simulation software. The excitor generates a pulse, exciting the fundamental guided mode at 1.55 μm for the specified polarization. The pulse has a sinusoidal envelope; the magnitude of the excitation rises sinusoidally from zero to its maximum value and then falls sinusoidally to zero again. The bandwidth of the pulse is determined by its time duration. For
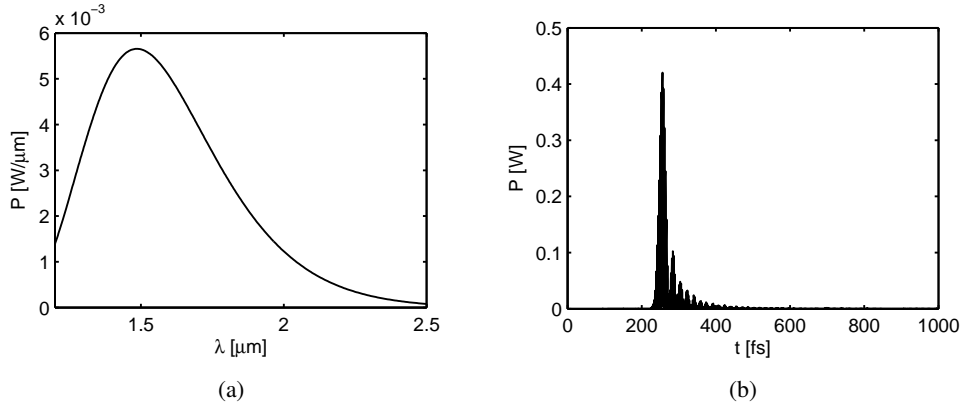
Figure 3.2: *a) Spectrum of the pulse with which the simulated structures are excited, and b) Time response of the output sensor for a PiA PhC waveguide ($r_d = 210$ nm) with a length of 40 periods, being a representative situation for all PhC simulations.*

our simulations, the time duration is chosen to be 20 fs resulting in the excitor spectrum as shown in Fig. 3.2(a). To reduce the calculation times, the highest frequencies (lowest wavelengths) are not taken into account. In our simulations, the minimum wavelength is 1.2 μm, corresponding to the normalized frequencies $0.409(a/\lambda)$ for PiA and $0.356(a/\lambda)$ for PiP. In both cases, the bandwidth of the excitor spectrum covers the full band gap, so that no relevant information is lost by neglecting these frequencies/wavelengths.

Following the excitor, a reference sensor is placed in the input waveguide. This sensor is used to act as a reference for the output sensor, which is located in the output waveguide. Furthermore, the reference sensor is used to determine the reflection from the PhC device. For the comparison between the output and the reference sensor to be meaningful, the pulse should have traversed the complete device, including the echo's that occur due to reflections at the PhC boundaries. The maximum length of our PhC lattice is 40 periods. Fig. 3.2(b) shows the time response of the output sensor to an excitation at the input. From this graph it can be seen that 1000 fs is long enough for the simulations on this structure. All 2D simulations, also those on shorter structures, have been performed with a time duration of 1000 fs.
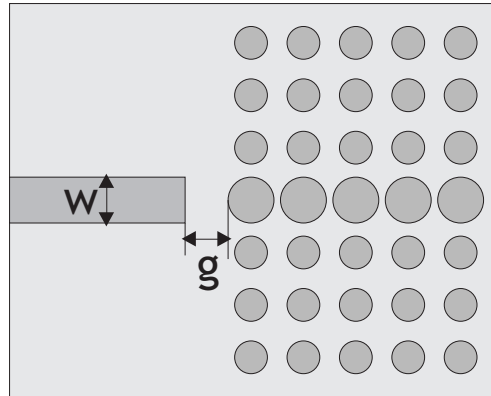
Figure 3.3: *Schematic drawing of the butt coupler.*

3.2 Coupling between photonic crystal waveguides and ridge waveguides

The simplest coupling structure between a ridge waveguide and a pillar photonic crystal waveguide is butt coupling: putting them opposite to each other, as shown in Fig. 3.3. The parameters a, r and r_d of the PhC waveguides were determined in section 2.3 (see Table 2.2). That leaves the gap g and the access waveguide width w to be optimized for the largest coupling efficiency. In literature, quite a few references can be found treating the coupling between classical ridge waveguides and waveguides in photonic crystals [45, 46, 47, 48]. In this section, we will start with an examination of the field profiles of both types of waveguides and their overlap. The width of the ridge waveguide can be varied to optimize the field overlap. However, the waveguide width affects the effective index of the waveguide mode and therefore its impedance, as will be described as well.

At first instance, the coupling from the classical ridge waveguide to the photonic crystal waveguide and vice versa will be optimized with 2D calculations. This optimization is done for pillar PhCs in air and for pillar PhCs with the polymer layer stack separately. Since they are very time consuming, 3D calculations will only be performed on the optimized designs for final evaluations.
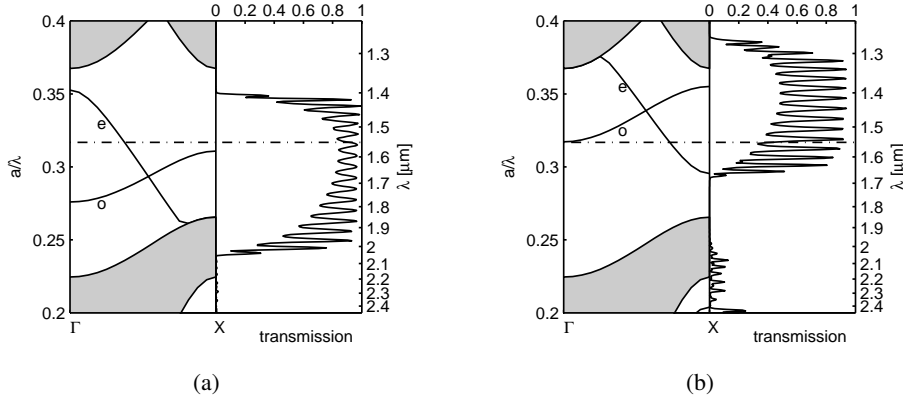
Figure 3.4: *Comparison of the transmission spectra and the band diagrams of the PhC waveguides with a length of 20 periods for PiA with a) $r_d = 210$ nm, and b) $r_d = 170$ nm, both with $w = 2r_d$ and $g = 0$ nm. The symmetry of the PhC waveguide modes is denoted by 'e' for even symmetry and 'o' for odd symmetry.*

3.2.1 Waveguides in air

We first calculate the transmission of the structure from the input waveguide to the output waveguide, with zero gap between the end facet of the ridge waveguide and the first defect pillar. Initially, the width of the access waveguides is taken to be equal to the diameter of the PhC waveguide pillars, i.e. $w = 2r_d$.

Fig. 3.4 shows the transmission spectrum of the PiA PhC waveguides with $r_d = 210$ nm and $r_d = 170$ nm in comparison with their respective band diagrams. Because the whole device is symmetrical, only its even modes are excited. The PhC waveguides are 20 periods long. The transmission shows a strong modulation as a function of the wavelength. This modulation is caused by the facets of the PhC waveguide, as a Fabry-Pérot cavity is created by the reflections on these. This is confirmed by comparing the transmission spectra of structures where the PhC waveguides have different lengths. Fig. 3.5 shows the transmission spectra for PhC waveguides ($r_d = 210$ nm) with 20, 30 and 40 periods length. The number of resonance peaks scales with the length of the PhC waveguide.

In order to optimize the coupling between the access ridge waveguides and the photonic crystal waveguide in the wavelength range around $\lambda = 1550$ nm, it is important to take into account the field profiles of both types of waveguide at this wavelength. The field profile of a guided mode in a classical ridge waveguide is invariant along the propagation direction. However, the photonic crystal waveguide supports a
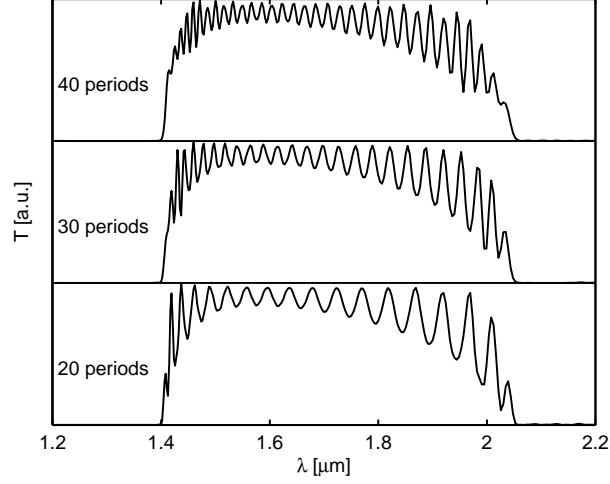
Figure 3.5: *Comparison of the transmission spectra of PhC waveguides with different lengths (PiA with $r_d = 210$ nm).*

Bloch mode, of which the E_y component is shown in Fig. 3.6(a) for the waveguide with $r_d = 210$ nm at $\lambda = 1550$ nm. Due to the symmetry of the super cell and its boundary conditions, the Bloch modes have their maxima and minima at the symmetry lines $z = 0$ and $z = a/2$, i.e. exactly through the center of the defect pillars and exactly in between the pillars. The absolute E_y field amplitudes at the extrema are plotted as a function of the transverse coordinate x in Fig. 3.6(b). The field of the Bloch mode is normalized to that of the classical ridge waveguide.

In Fig. 3.7 the same data are plotted for PiA with $r_d = 170$ nm. From the field profiles it can be seen that the field of the PhC waveguide with $r_d = 210$ nm is more confined than the field of the PhC waveguide with $r_d = 170$ nm. In the latter case, the field profile at $z = 0$ has strong additional maxima at the rows of pillars next to the defect pillars, but also the field in between the pillars has larger tails into the surrounding photonic crystal.

The field profiles from Fig. 3.6(b) and 3.7(b) show that the best overlap with the field profile of the fundamental guided mode of a classical ridge waveguide will be obtained if the classical waveguide field is offered at $z = a/2$, the position exactly in between two pillars. That is to say, the optimal gap between the end facet of the ridge waveguide and the first waveguide pillar is given by

$$g_{opt} = 0.5(a - 2r_d) \tag{3.1}$$

56
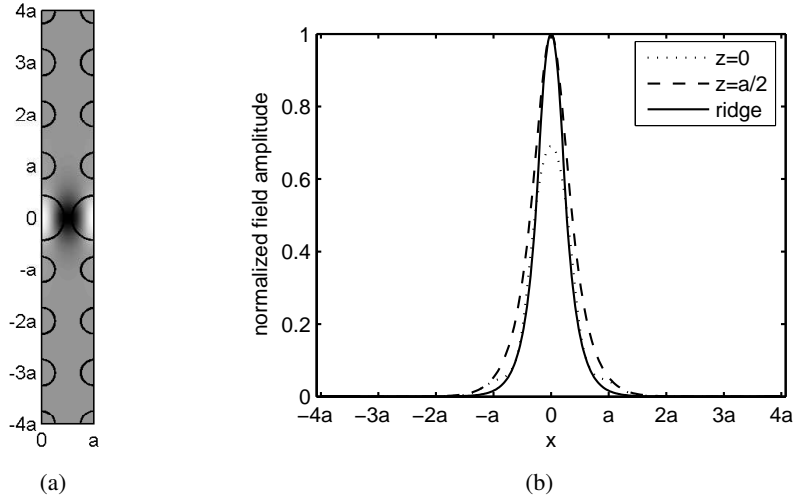
Figure 3.6: *Fields of the guided modes at* $\lambda = 1550$ *nm for PiA with* $r_d = 210$ *nm, a) field amplitude distribution of the guided Bloch mode, and b) the normalized fields at the symmetry points of the PhC waveguide and that of a ridge waveguide with* $w = 2r_d$.
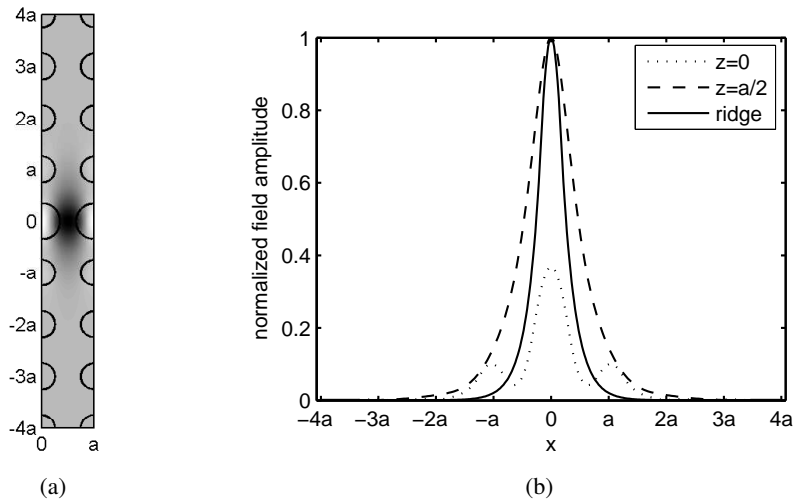
Figure 3.7: *Fields of the guided modes at* $\lambda = 1550$ *nm for PiA with* $r_d = 170$ *nm, a) field amplitude distribution of the guided Bloch mode, and b) the normalized fields at the symmetry points of the PhC waveguide and that of a ridge waveguide with* $w = 2r_d$.

With this gap, the end facet of the ridge waveguide is placed exactly at the mirror plane between the last (real) pillar and the next (virtual) pillar. At this position, the shapes of the E_y fields of both the classical and the photonic crystal waveguide are similar.

To maximize the overlap between the field of the Bloch mode at this position and the field of the fundamental guided mode in the ridge waveguide, the waveguide width can be varied. This provides us with an initial design window for the access ridge waveguide. Fig. 3.8 shows the calculated overlap of the field profile E_{y1} of the Bloch mode (at $z = 0$, exactly between the pillars) with the field E_{y2} of a ridge waveguide of which the width is varied. The overlap of both fields $E_{y1}(x)$ and $E_{y2}(x)$ is determined as

$$\text{Overlap} = \frac{|\int E_{y1}(x)E_{y2}(x)dx|^2}{\int E_{y1}^2(x)dx \int E_{y2}^2(x)dx} \tag{3.2}$$

Both curves in Fig. 3.8 have a dip at $w = 200$ nm. This is the width for which the ridge waveguide has the narrowest mode profile, resulting in a low overlap value. Both photonic crystal waveguides have broader mode profiles than the waveguide at this point. Overall, the overlap of the ridge waveguide with the mode profile of the Bloch mode of $r_d = 210$ nm is higher. This is the result of the smaller mode profile that was shown before in Fig. 3.6(a), which has a better overlap with the narrow field profile of a ridge waveguide. The curve for $r_d = 210$ nm has a maximum for $400 < w < 450$ nm, for which the overlap is 99%. The slight mismatch in mode profile accounts for a loss of $\simeq 0.04$ dB per transition. In contrast, the curve for the photonic crystal waveguide with $r_d = 170$ nm does not reach a maximum by increasing the width of the ridge waveguide from 200 to 500 nm, because of its wider Bloch field profile at $z = 0$ (see Fig. 3.7(a)). At the waveguide width of 340 nm, equal to the diameter of the waveguide pillars, the overlap is 91.8%, resulting in a loss of $\simeq 0.37$ dB per transition.

Both overlaps increase also if the ridge waveguide width is reduced below 200 nm. The field profile of the ridge waveguide is broadening as its width is decreasing. If the waveguide width is very small, the field resembles a plane wave, and in the end the overlap decreases. This implies that for small waveguide widths a second maximum is reached in the overlap curve. However, there are a number of reasons not to reduce the waveguide width below 200 nm in real (3D) applications. Firstly, the waveguide mode will be pushed to the InP substrate if the ridge waveguide is very narrow and if it is not etched deep enough into the substrate. Secondly, for a very narrow waveguide the influence of sidewall roughness will be high. And finally, the fabrication of waveguides with a width of 50-100 nm and an etch depth of several micrometers is difficult, if not impossible.

In the preceding paragraphs, the field overlap of the ridge waveguide mode to the PhC Bloch mode at a certain position was taken. This is a much simplified picture,
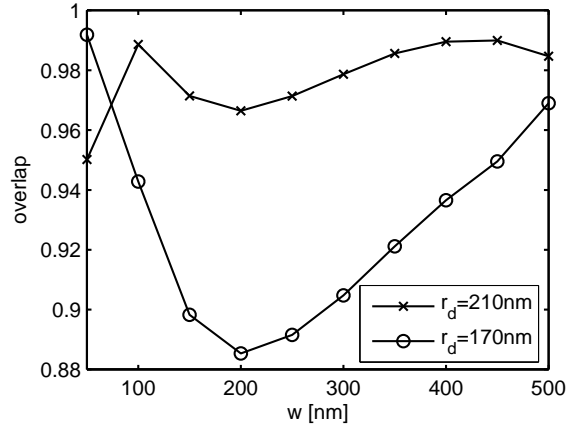
Figure 3.8: *Overlap of the field of the fundamental guided TM mode of a ridge waveguide and the field of a Bloch mode in between two adjacent waveguide pillars at* $\lambda = 1550$ *nm, for two different line defects and varying ridge waveguide width.*

meant to get an idea of the design window for the access ridge waveguide. However, the mechanism of light propagation in a photonic crystal waveguide is different from that in a classical waveguide [49]. Therefore, calculating the overlap in itself does not predict the actual transmission at the transition between the two types of waveguides.

To find the influence of the ridge waveguide width and the gap size on the transmission of the coupling structure between both types of waveguides, the transmission is simulated using a 2D FDTD method as described before. A PhC waveguide of 40 periods length was modeled. To filter out the modulation due to Fabry-Pérot resonances, the transmission is taken as the mean value of the minimum and maximum within the wavelength range 1530–1570 nm. This is the EDFA window which is the interesting range for applications. In principle, a component could be designed in such a way that it operates at the maximum of a resonance peak in order to obtain a high transmission. However, this will reduce the bandwidth of efficient operation. Due to the limited number of Fabry-Pérot peaks in the wavelength range under consideration, taking the mean of the minimum and maximum transmission better estimates the transmission over the whole wavelength regime than taking the average of the simulation data over that range.

Fig. 3.9 shows the dependence of the transmission of the structures on the gap g. The lowest loss is obtained for a gap size of 35 nm for the PiA PhC waveguide with $r_d = 210$ nm. This is in agreement with Eq. 3.1, as for $a = 491$ nm the equa-
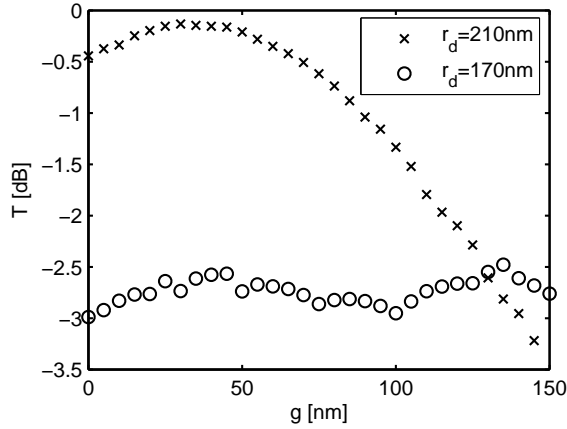
Figure 3.9: *Transmission of a photonic crystal waveguide as a function of the gap for two different line defects. The calculated spectra are averaged over the wavelength range 1530–1570 nm to filter out Fabry-Pérot resonances.*

tion evaluates to $g_{\mathrm{opt}} = (491 - 2 \cdot 210)/2 = 35.5$ nm. The optimum gap results in 0.15 dB insertion loss. In the case of $r_{\mathrm{d}} = 170$ nm, the transmission is significantly lower and it has no pronounced maximum. The optimum gap is expected to be $g_{\mathrm{opt}} = (491 - 2 \cdot 170)/2 = 75.5$ nm. At that gap size, the reduction in transmission is 2.86 dB. Since the mismatch in the mode profiles for that gap size was found to give a loss of $\simeq 0.37$ dB per transition, the mode field matching is not the only mechanism influencing the coupling efficiency.

The only remaining way of influencing the coupling efficiency is tuning the width of the access waveguides. The transmission and reflection of both structures as a function of the width of the access waveguides is shown in Fig. 3.10. In these simulations, the gap size is the optimum gap as calculated from Eq. 3.1. The transmission is defined as the fraction of the intensity that is eventually coupled to the fundamental guided TM mode at the output waveguide. The reflection is the fraction of the intensity that is coupled to the backward propagating fundamental guided TM mode in the input waveguide. Light that radiates away and that is absorbed by the PMLs is regarded as loss, just as higher order modes that might be excited in the structure.

For the waveguide with $r_{\mathrm{d}} = 210$ nm the transmission increases for a waveguide width $w > 200$ nm because the mode profiles have a better overlap. However, the transmission also increases for narrower waveguides in the range $0 < w < 200$ nm, which is not explained by the mode profile overlap. Fig. 3.11 shows the calculated
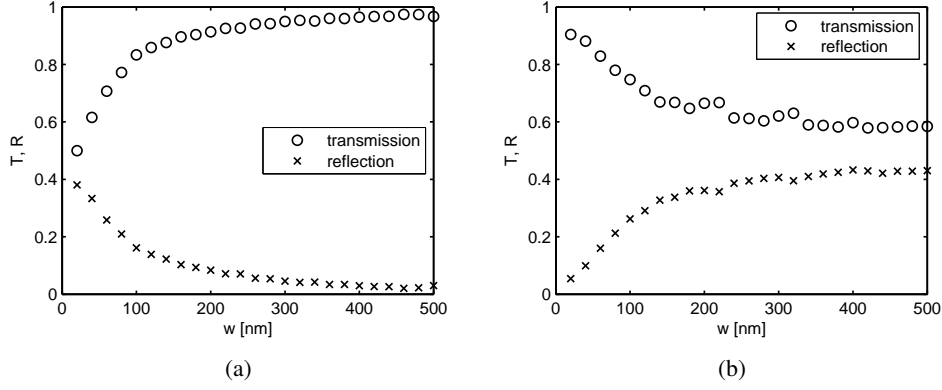
Figure 3.10: *Transmission and reflection of a 40-period-long photonic crystal waveguide as a function of ridge waveguide width for PiA with a) $r_d = 210$ nm and $g = 35.5$ nm, and b) $r_d = 170$ nm and $g = 75.5$ nm.*

effective refractive index of the fundamental guided TM mode of the ridge waveguide and the effective index that corresponds to the PhC modes with even symmetry. The PhC modes are repeated over several Brillouin zones, four of which are represented in the graph. The crosses in the diagram belong to the PhC waveguide mode with $r_d = 210$ nm. It can be seen that a ridge waveguide with a width of $\simeq 200$ nm has an effective index that matches the effective index that can be associated with the guided PhC waveguide mode. For smaller ridge waveguide widths, there is a larger mismatch in effective index. This might be the dominant factor in the decreasing transmission if the width is reduced.

For the PhC waveguide with $r_d = 170$ nm the transmission decreases if the width is increased in the range $0 < w < 120$ nm. Here we can see from Fig. 3.11 that the effective index matches rather well to the present PhC waveguide modes, but from Fig. 3.8 we see a decrease in field overlap. Apparently, this mismatch in field overlap is dominant in the regime of narrower waveguides. For waveguides wider than 120 nm, the effective index matching is reduced and the transmission decreases.

In the case of PiA PhCs with a waveguide defect radius of 210 nm, choosing the width of the access waveguides to equal the diameter of the waveguide pillars results in a high transmission; with the optimized gap of 35.5 nm the losses are 0.15 dB for a 40-period-long PhC waveguide. For $r_d = 170$ nm the choice for the geometrical parameters is not as straightforward. The highest calculated transmission is obtained for $w = 20$ nm. However, in practical applications where substrate leakage and sidewall
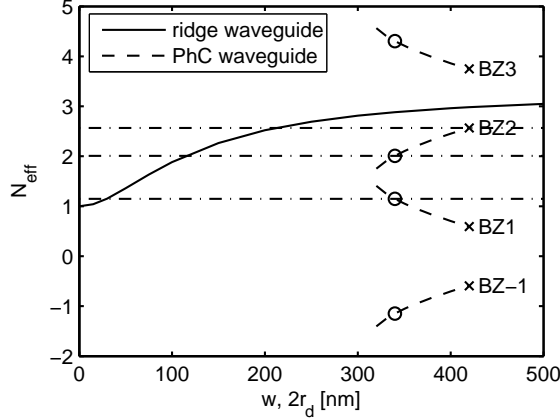
Figure 3.11: *Effective index for the ridge waveguide mode (fundamental TM polarized mode) as a function of the waveguide width and the effective indices of the PhC guided mode (TM mode with even symmetry) as a function of the defect radius.*

roughness will play a role, this waveguide width will not be suitable. Therefore, also for this PhC waveguide the waveguide width is chosen to equal the diameter of the waveguide pillars and the gap is chosen according to Eq. 3.1.

Fig. 3.12 shows the transmission and reflection for the 40-period-long PiA PhC waveguide with $r_d = 210$ nm for $g = 0$ nm and for $g = 35.5$ nm with access waveguides of 420 nm width. Fig. 3.12(b) indeed shows a higher transmission around $\lambda = 1.55$ μm. By introducing a (non-zero) gap between both types of waveguides, an extra cavity is created in the structure. This induces an additional wavelength dependence on the transmission and the bandwidth of the device is reduced. By maximizing the transmission we implicitly minimized the reflections at the transitions between both types of waveguides. Therefore, the losses of the Fabry-Pérot cavity between the transitions are reduced. This causes the modulation to be reduced in the wavelength range for which the coupling was optimized. The transmission and reflection for the PhC waveguide with $r_d = 170$ nm are shown in Fig. 3.13 for $g = 0$ nm and for $g = 75.5$ nm. In both graphs, the reflections are higher than for $r_d = 210$ nm, which is in agreement with earlier simulations. The reflections are reduced by optimizing the gap size, but the transmission has a small bandwidth and does not cover the EDFA window. However, practical issues inhibit the reduction of the waveguide width to increase the transmission in the EDFA window.
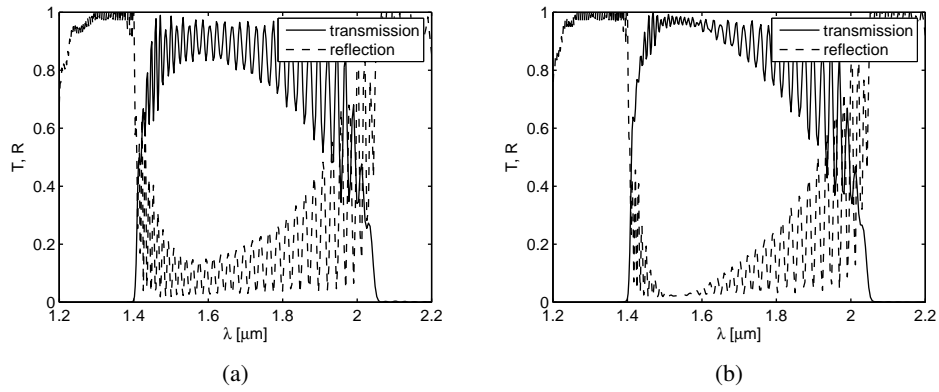
Figure 3.12: *Transmission and reflection spectra of the PiA PhC waveguide with $r_d = 210$ nm with a) $g = 0$ nm, and b) $g = 35.5$ nm.*
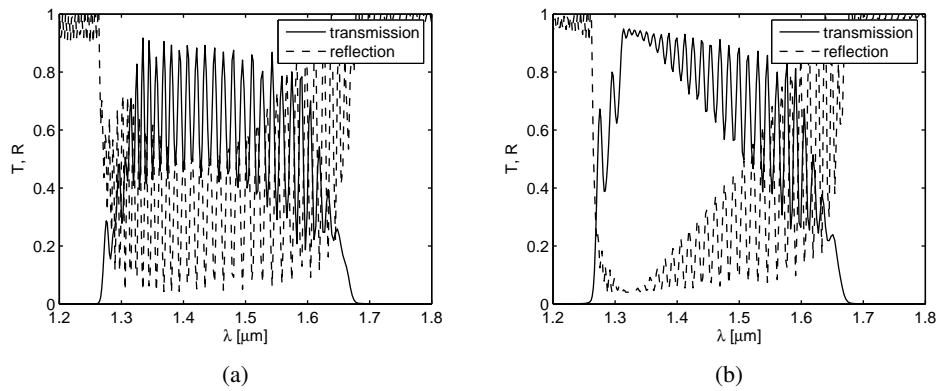
Figure 3.13: *Transmission and reflection spectra of the PiA PhC waveguide with $r_d = 170$ nm with a) $g = 0$ nm, and b) $g = 75.5$ nm.*
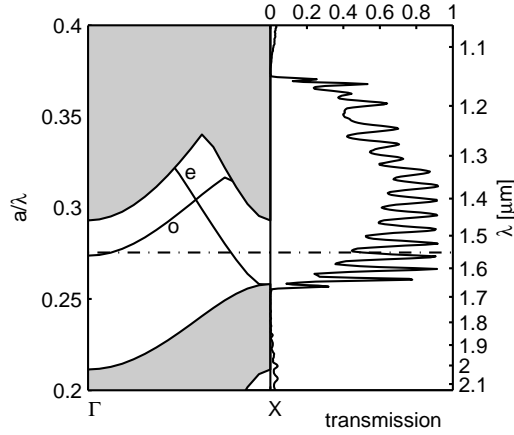
Figure 3.14: *Comparison of the transmission spectrum and the band diagram of the PhC waveguides of pillars in a polymer layer stack with a length of 20 periods with $r_d = 155$ nm, $w = 2r_d$ and $g = 0$ nm. The symmetry of the PhC waveguide modes is denoted by 'e' for even symmetry and 'o' for odd symmetry.*

3.2.2 Waveguides in a polymer layer stack

For the photonic crystal waveguide of pillars in a polymer layer stack the same optimization scheme is followed as for the pillars in air. The geometric parameters of the crystal and the line defect were found in section 2.3.2. The lattice constant is $a = 427$ nm, the radius of the pillars is $r = 107$ nm and the defect pillars have a radius $r_d = 155$ nm. The band diagram is shown in Fig. 3.14, where it is compared to the transmission through the corresponding PhC waveguide with a length of 20 periods. The size of the band gap is smaller than in the case of PiA, and the guided mode with even symmetry has a large tail into the air cladding modes. The transmission outside the band gap is clearly affected by the presence of the cladding modes, but inside the band gap the transmission of the guided mode resembles the transmission of the PiA PhC waveguides in Fig. 3.4.

The Bloch mode at $\lambda = 1550$ nm and the field profiles are given in Fig. 3.15(a). For PiP, the field extends even more into the background photonic crystal than for the PiA PhC waveguide with $r_d = 170$ nm. This is clearly the result of the reduction in index contrast. Since the ridge waveguide in this case also has a cladding with a slightly higher refractive index than in the case of PiA (i.e. 1.5236 instead of 1), the mode profile of the ridge will also be slightly broader.

The calculated overlap of the ridge waveguide mode and the photonic crystal Bloch

(a)   (b)
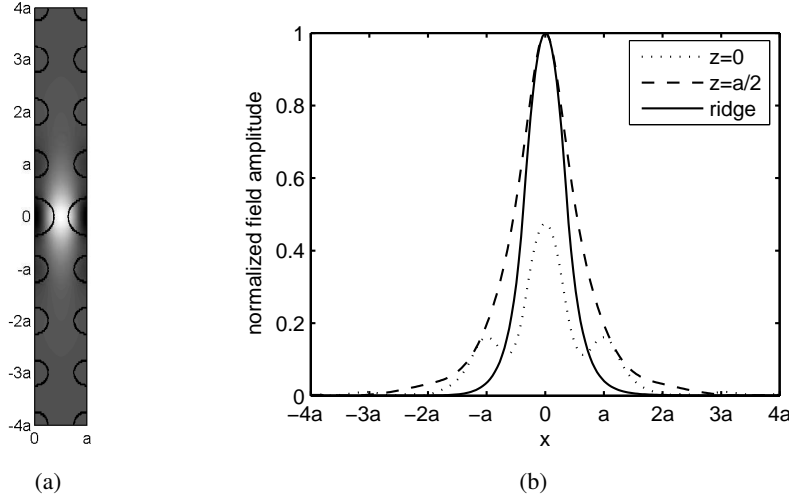
Figure 3.15: *Bloch mode of the PiP PhC waveguide with $r_d = 155$ nm at $\lambda = 1550$ nm, a) the field distribution in the super cell and b) the mode profiles as a function of the transverse coordinate x at $z = 0$ and at $z = a/2$.*

mode at $z = a/2$ is shown in Fig. 3.16. Here it can be seen that the minimum over-lap is slightly shifted towards larger waveguide width with respect to the PiA case (see Fig. 3.8), due to the reduction in lateral index contrast. Furthermore, the overlap curve has the same characteristics as that of PiA with $r_d = 170$ nm. For waveguides smaller than 200 nm the overlap increases, but this regime is in practice not suited for waveguiding, as was discussed before. For waveguides wider than 200 nm, the overlap increases due to the wide mode profile of the PhC Bloch mode.

In Fig. 3.17(a) the transmission of the PiP photonic crystal waveguide is shown as a function of the gap g. The transmission of the structure is around -2.33 dB for gap size $g = 58.5$ nm, which is the optimal value according to Eq. 3.1. The dependence of the transmission on the gap is smaller for PiP than it is for PiA (see Fig. 3.9). Due to the reduction in lateral refractive index contrast by introducing the polymers, the reflections at the interfaces are reduced. This causes the influence of the gap cavity to be reduced. Moreover, the diffraction angle is smaller in the case of a lower index contrast.

In Fig. 3.17(b), the transmission and reflection of the PiP photonic crystal wave-guide are shown as a function of the width of the access waveguides. The transmis-sion reaches a maximum for a waveguide width of $\simeq 80$ nm and decreases for wider
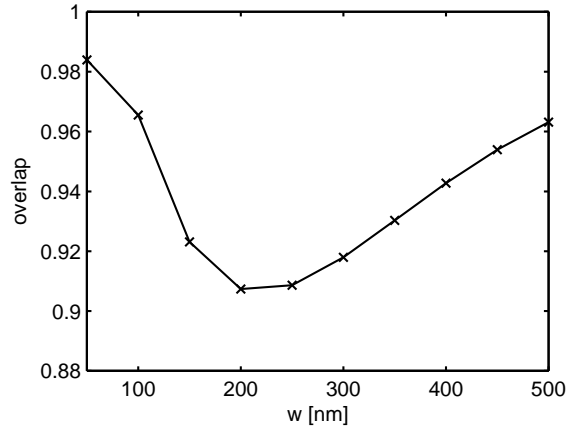
Figure 3.16: *Overlap of the field of the fundamental guided TM mode of a ridge waveguide and the field of a Bloch mode in between two adjacent waveguide pillars at $\lambda = 1550$ nm, for a line defect with $r_d = 155$ nm and varying ridge waveguide width.*

(a)

(b)
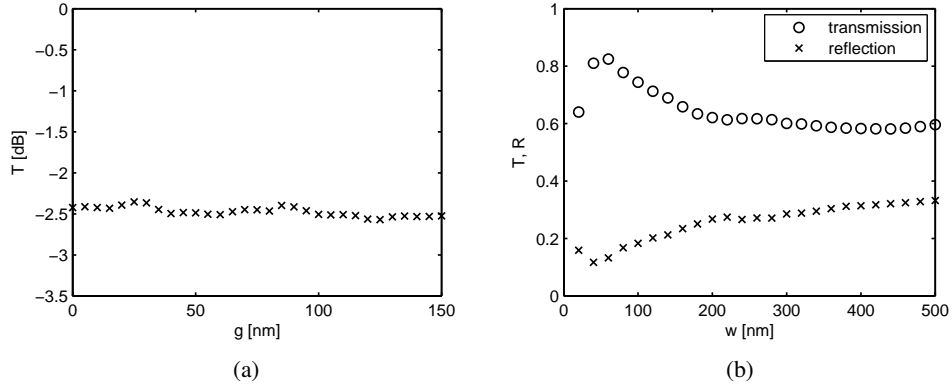
Figure 3.17: *Response of a 40-period-long PiP photonic crystal waveguide with $r_d = 155$ nm averaged over the wavelength range from 1530 to 1570 nm, a) transmission as a function of the gap g with $w = 2r_d$, and b) transmission and reflection as a function of ridge waveguide width w with $g = 0.5(a - 2r_d)$ nm.*
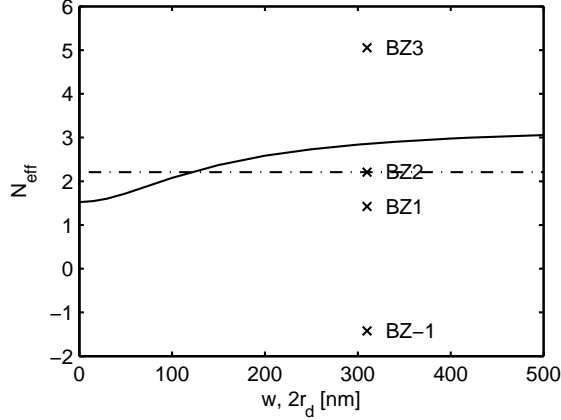
Figure 3.18: *Effective index for the ridge waveguide mode (fundamental TM polarized mode) as a function of the waveguide width and the effective indices of the PhC guided mode (TM mode with even symmetry) as a function of the defect radius.*

waveguides. Fig. 3.18 shows the effective refractive indices of the ridge waveguide mode (fundamental TM polarized mode) and the PhC waveguide mode (TM mode with even symmetry). For small waveguide widths, the effective indices of both waveguide modes are well-matched. From Fig. 3.16 we saw that the mode overlap is large for narrow waveguides. This causes the transmission peak around $w = 80$ nm. For waveguide widths larger than 200 nm the mode overlap increases, but the effective indices have a larger mismatch and the transmission therefore decreases.

At the waveguide width $w = 310$ nm, equal to $2r_d$, the reflection is 33%, accounting for a reduction in the transmission of 1.7 dB. Following the same reasoning as in the previous section, the waveguide width is chosen to equal the diameter of the waveguide pillars and the gap is chosen according to Eq. 3.1. The calculated transmission and reflection for the structure with $w = 2r_d$ is shown in Fig. 3.19 for $g = 0$ nm and $g = g_{opt}$. Again, the influence of the cladding modes is clearly visible for wavelengths < 1320 nm. For this structure, introducing a gap does not influence the transmission considerably, in agreement with Fig. 3.17(a).

3.2.3 3D simulations

Three-dimensional simulations are time consuming and require large computational powers. Therefore, the optimization of the structures was done using 2D simulations at first instance. In this section, the designs of the previous section are verified with
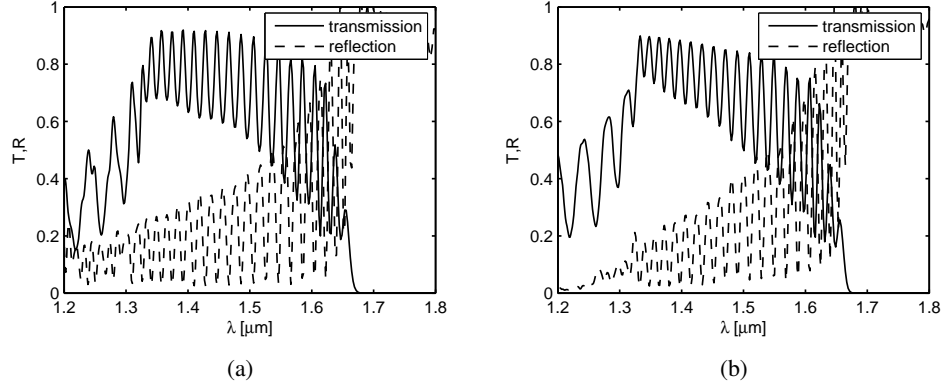
Figure 3.19: *Transmission and reflection spectra of the PiP PhC waveguide with $r_d = 155$ nm with a) $g = 0$ nm, and b) $g = 58.5$ nm.*

3D simulations.

To start with, the photonic crystal waveguides optimized for pillars in air are simulated. The length of the waveguides is chosen to be 20 periods to limit the computation times. With the available computational resources, the smallest grid spacing is $a/16$. The calculated transmission and reflection of TM polarized light are shown in Fig. 3.20.

For the pillar photonic crystal waveguide with $r_d = 210$ nm, the transmission spectrum resulting from the 3D calculation is similar to the spectrum from the 2D simulation that is shown in Fig. 3.12. The transmission is slightly lower in the 3D simulation than it was in the 2D simulations, but still it is above 90% with 90 nm bandwidth (1.47–1.56 µm). The out-of-plane propagation loss in the photonic crystal is the cause of this lower transmission. The propagation loss also causes the Fabry-Pérot modulation to disappear from the transmission spectrum.

For the pillar photonic crystal waveguide with $r_d = 170$ nm, the transmission calculated in a 3D simulation deviates more from the 2D results than for the PhC waveguide with the larger defect of 210 nm radius. The transmission of $\sim 60\%$ at $\lambda = 1.55$ µm in 2D (see Fig. 3.13) is reduced to $< 10\%$ in a 3D simulation. As with the larger defect, the difference in transmission is caused by the out-of-plane losses. However, the out-of-plane losses are much larger for the photonic crystal waveguide with $r_d = 170$ nm. The first reason is the fact that the distance between the adjacent waveguide pillars is larger, which causes an increase in the diffraction losses. Secondly, the slope of the guided mode, and thus the group velocity is smaller for the waveguide with the smaller
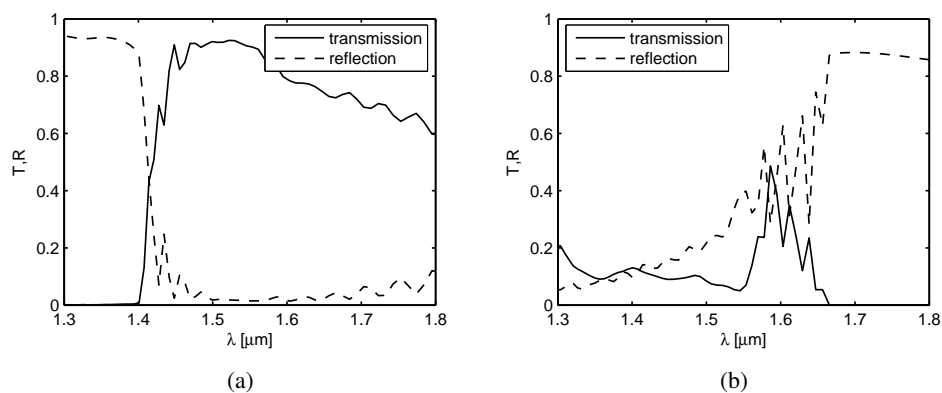
Figure 3.20: *Transmission and reflection spectra of the PiA PhC waveguides resulting from 3D simulations with a) $r_d = 210$ nm and b) $r_d = 170$ nm for TM polarization. In both cases the waveguides were 20 periods long, with $g = 0.5(a - 2r_d)$ and $w = 2r_d$.*

defect radius (see Fig. 3.4 and section 5.3.3), resulting in higher propagation loss [50].

The calculated transmission and reflection spectra of the photonic crystal waveguide that was optimized for pillars embedded in a polymer layer stack are shown in Fig. 3.21. The transmission around $\lambda = 1.55$ μm resulting from the 2D simulation is $\sim 60\%$ (see Fig. 3.19(b)). From the 3D simulation a transmission of 20% is obtained. Although the transmission is lower in the 3D calculation, the difference between the results is smaller than for the pillars PhC waveguide in air with $r_d = 170$ nm. A Fabry-Pérot modulation is present in the 3D simulation results. This indicates that the propagation losses are less than for the pillars in air with a defect radius of 170 nm, but not as small as for the pillars in air with a defect radius of 210 nm.

3.3 Polarization filters

So far only the TM polarization was regarded for waveguiding, since in section 2.2 it was shown that a square lattice of photonic crystal pillars has a band gap for TM polarization only. In this section the possibility of exploiting the polarization selectivity of these photonic crystals for polarization filtering is investigated.

69
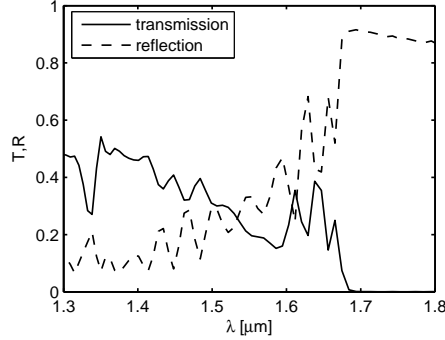
Figure 3.21: *Transmission and reflection spectra of the PiP PhC waveguides resulting from 3D simulations for TM polarization. The length of the waveguide is 20 periods, with $r_d = 155$ nm, $g = 0.5(a - 2r_d)$ and $w = 2r_d$.*

3.3.1   TE filter

A waveguide based on a line defect in a pillar photonic crystal can serve as a TE filter if the TE polarized light does not couple into the photonic crystal waveguide (either if the photonic crystal waveguide has a TE band gap or if the coupling efficiency for TE is very small) or if the TE polarized light is not confined by the crystal, in which case it radiates away from the line defect. At the same time the transmission of TM polarized light should be high.

In the previous section three PhC structures were optimized to give a high transmission for TM polarization. To investigate the suitability of the PhC waveguides as TE filters, the transmission of the three designed PhC waveguides (one in PiP, two in PiA) is calculated as a function of the length of the photonic crystal waveguide for the two polarizations. The results are shown in Fig. 3.22. By extrapolating the simulation data for each waveguide to $N = 0$, it can be seen that the transmission is dominated by the coupling loss and that the propagation loss is very small in this 2D simulation. Especially the PiA PhC waveguide with $r_d = 210$ nm has a low coupling efficiency for TE polarization. At the same time it has a high transmission for TM. Therefore, the performance of this device is the best for TE filtering. The length of the photonic crystal is in this respect not critical, ~ 10 periods is long enough, since the coupling is the mechanism taking care of the filtering.

For the case of $r_d = 170$ nm the TM transmission is lower than for the PhC with $r_d = 210$ nm, corresponding to the simulation results of the previous section. However, the transmission of TE polarized light is larger. The extinction ratio is even worse for
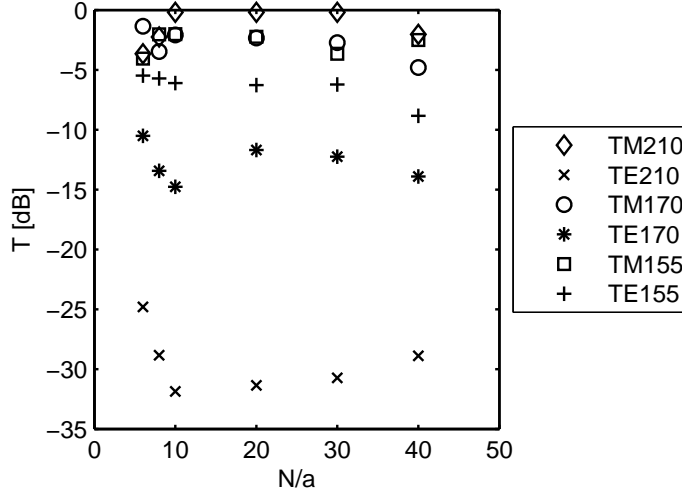
Figure 3.22: *TM and TE transmission of a photonic crystal waveguide based on different line defects as a function of the length of the waveguide in periods.*

the PiP PhC waveguide, for which we had already seen that the TM transmission was worst. The wavelength-dependence of the transmission of both polarizations is shown in Fig. 3.23. Indeed, the transmission of TE is small around $\lambda = 1550$ nm for the PiA PhC waveguide with $r_d = 210$ nm. For the PiA PhC waveguide with $r_d = 170$ nm the center wavelength is found to be in a different regime; right at that wavelength, a continuum of TE polarized modes appears towards longer wavelengths. Although the TE transmission at $\lambda = 1550$ nm is $\simeq -23$ dB, the influence of the continuum of TE modes at longer wavelength is present in the averaging over the wavelengths from 1530 to 1570 nm. At wavelengths ≤ 1550 nm, the suppression of the TE polarization is ≥ 11 dB while the TM transmission is high. Although this design is not suitable for TE filtering at $\lambda = 1550$ nm, it will have a better performance as a TE filter for shorter wavelengths. The PiP PhC waveguide has a broad transmission peak for TE polarization at the desired wavelengths. Since the transmission for TM polarization was small, as was found in the previous section, the design as modeled by 2D simulations is not suitable for TE filtering.

Fig. 3.24 shows the band diagrams for both PiA waveguide defects, including the TE bands. For the larger waveguide defect (Fig. 3.24(a)) there are two TE modes with even symmetry in the irreducible Brillouin zone at the center wavelength of 1550 nm. However, for the smaller waveguide defect (Fig. 3.24(b)) there are three TE modes
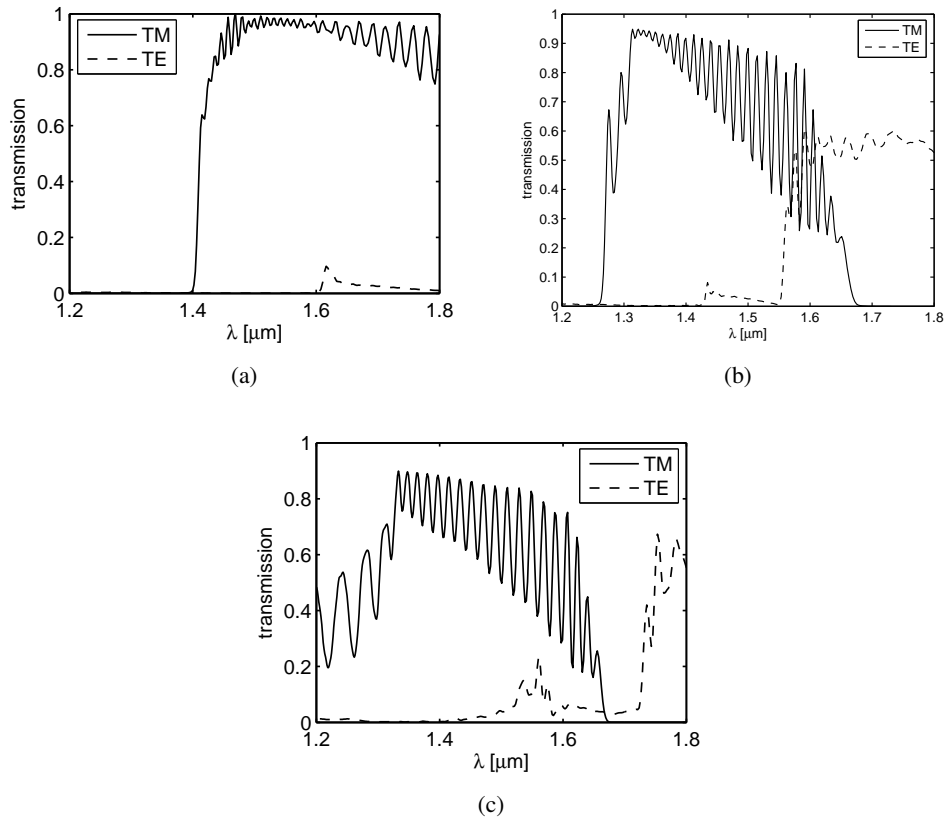
Figure 3.23: *Transmission of TE and TM polarized light (dashed and solid lines, respectively) in a 40-period long photonic crystal waveguide a) PiA with a line defect of $r_d = 210$ nm, b) PiA with $r_d = 170$ nm and c) PiP with a line defect of $r_d = 155$ nm.*

with even symmetry. Since the access waveguides are placed symmetrically in front of the PhC waveguide, only the Bloch modes with even symmetry will be excited in the structure. The smaller number of available TE Bloch modes in the photonic crystal waveguide with $r_d = 210$ nm might reduce the coupling efficiency, since the incoming TE ridge waveguide mode has to distribute its energy over the available photonic crystal waveguide modes. For the PiP PhC waveguide with $r_d = 155$ nm, the band diagram is shown in Fig. 3.25. The situation resembles that of the PiA waveguide with $r_d = 170$ nm, also in this case three TE modes are present with even symmetry. The transmission of TE polarized light is even higher in this case, and at the same time the transmission of TM polarized light is lower, as was found in the previous section.

In these 2D simulations, the polarization filter based on a line defect with $r_d = 210$ nm in a PiA photonic crystal results in a good performance with a TE suppression of > 30 dB while the losses for TM are below 1 dB. In a real device, however, the third dimension plays a role too. As we have seen in section 2.4, the propagation losses are quite high for the pillars in air. For the PiA PhC waveguides the transmission will vary with waveguide length. Since the dominant filtering mechanism is the coupling of the TE polarization, the device should be kept small to have a high performance.

For pillar photonic crystal waveguides with a polymer slab waveguide, the propagation losses are significantly reduced by the implementation of the polymer slab waveguide. Since the difference between TE and TM in coupling efficiency is small, the simulated device will not have a good performance in practical applications. If the waveguide would be much longer, however, the TE polarized light eventually radiates away from the line defect in the photonic crystal because the waveguide modes are not confined by a band gap in the surrounding crystal. Since the propagation loss for TM is low, the device might still result in a good TE filter. Therefore, the devices have been compared to 3D simulations to find the optimal design.

Since the 3D simulations are time-consuming and since the length dependence that is found from 2D simulations is small (see Fig. 3.22), two TE filters with a length of 8 periods are simulated in 3D. Fig. 3.26 shows the TE filter of pillars in air, comparing the results of the 3D simulation with those of the 2D simulation. The results are similar because the device is short and therefore out-of-plane losses are limited.

Fig. 3.27 compares the 3D and 2D simulation results for the pillar photonic crystal waveguide in a polymer layer stack. Also for this device the behavior is comparable for both simulations, due to the limited length of the device.

In summary, the TE filter that has the best performance is the one based on pillars in air. The calculated transmission is -2.3 dB for TM polarization with an extinction ratio for TE of better than 25 dB. The good performance is mainly due to a high coupling efficiency of the TM polarization at the transitions between the ridge waveguide
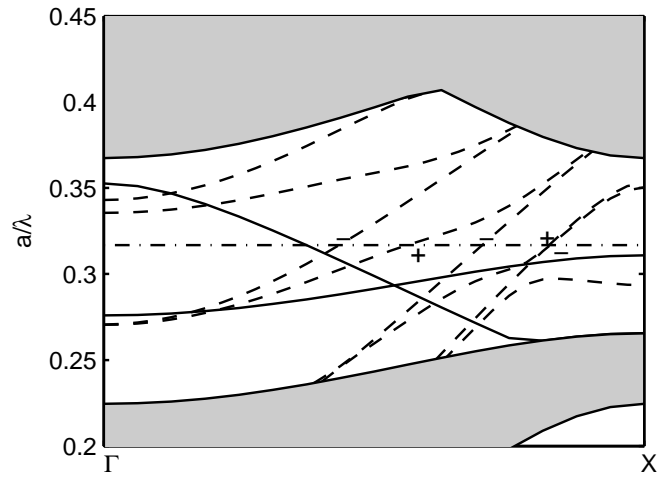
(a)
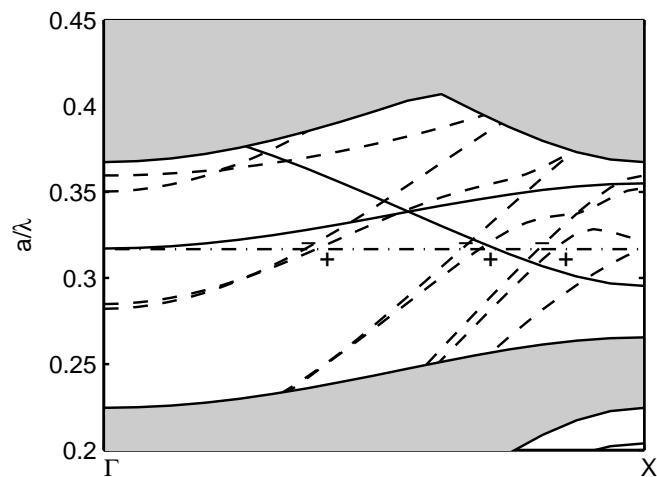
(b)

Figure 3.24: *Band diagrams of both TE and TM modes (dashed and solid lines, respectively) in a PiA photonic crystal waveguide with a line defect of a) $r_d = 210$ nm and b) $r_d = 170$ nm. The symmetry of the Bloch modes at 1550 nm (the dash-dotted line at $a/\lambda = 0.3168$) is indicated by the + signs for even symmetry and − signs for odd symmetry.*
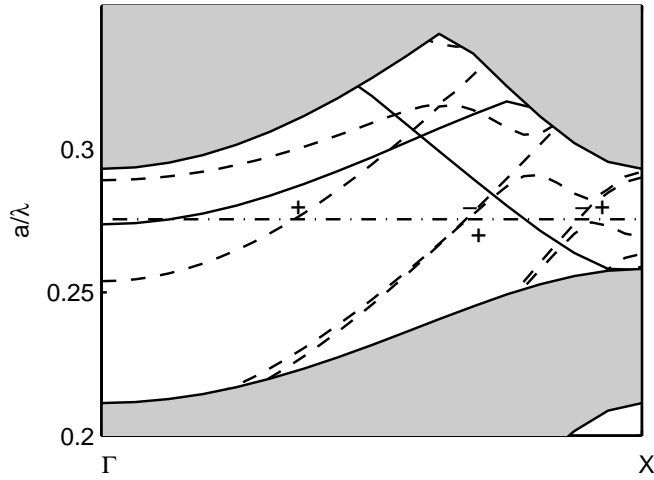
Figure 3.25: *Band diagrams of both TE and TM modes (dashed and solid lines, respectively) in a PiP photonic crystal waveguide with a line defect of $r_d = 155$ nm. The symmetry of the Bloch modes at 1550 nm (the dash-dotted line at $a/\lambda = 0.2755$) is indicated by the $+$ signs for even symmetry and $-$ signs for odd symmetry.*
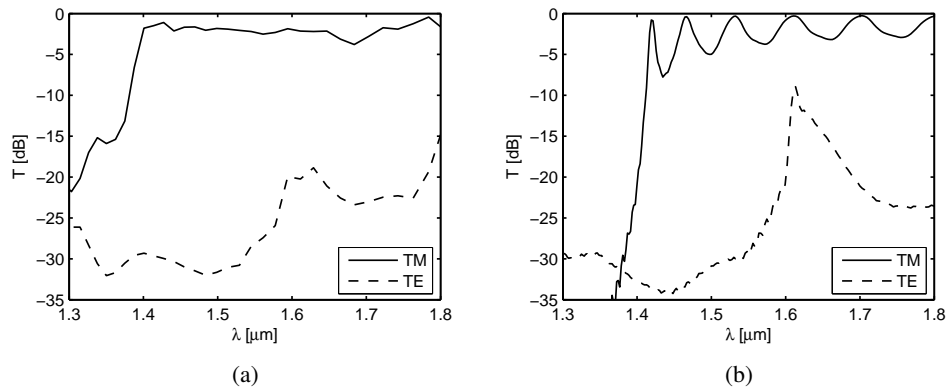
Figure 3.26: *Polarization dependent transmission of a TE filter of pillars in air of 8 periods length, a) from a 3D simulation and b) from a 2D simulation.*
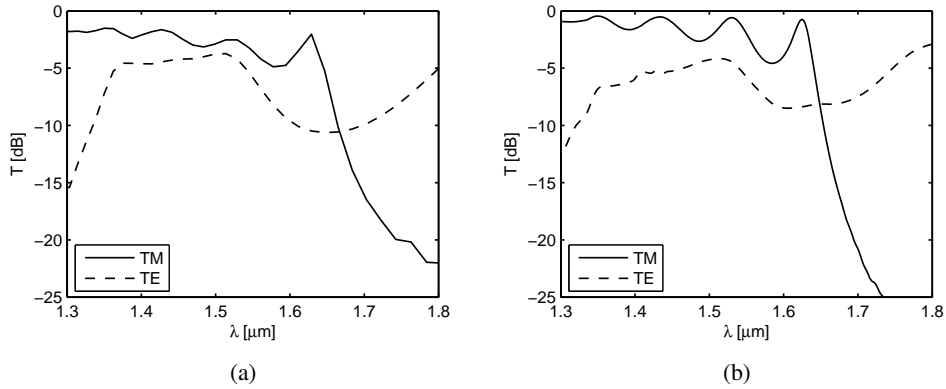
Figure 3.27: *Polarization dependent transmission of a TE filter of 8 periods length, based on the pillar photonic crystal in a polymer layer stack a) from a 3D simulation and b) from a 2D simulation.*
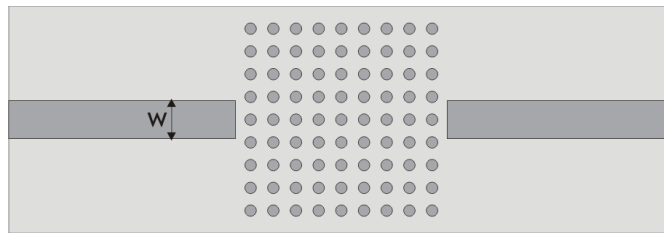
Figure 3.28: *Schematic drawing of a TM filter.*

and the photonic crystal waveguide, while the TE polarization has a poor coupling to the PhC waveguide.

3.3.2 TM filter

The presence of the TM band gap in a square-latticed pillar photonic crystal while TE modes are supported, can alternatively be exploited in a TM filter. TM filtering can be realized by intersecting a classical ridge waveguide with a defect-free photonic crystal as shown in Fig. 3.28. This photonic crystal prevents the TM polarized light to be transmitted. The TE polarized light is not prohibited to pass through, and it is captured by the output ridge waveguide.

To investigate the feasibility of TM filtering with such a structure, the transmission

76
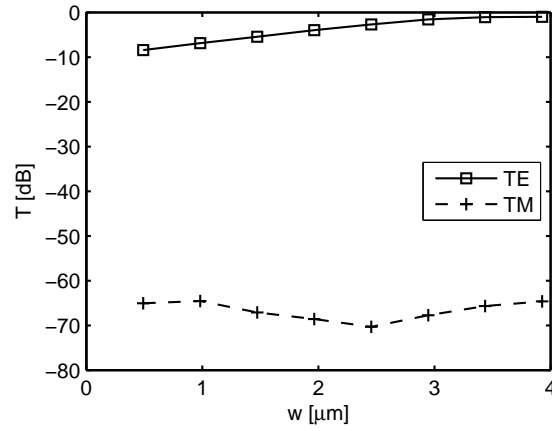
Figure 3.29: *TM and TE transmission of a PiA photonic crystal intersecting a ridge waveguide as a function of the access waveguide width.*

of both polarizations is calculated as a function of the length of the PiA photonic crystal and for varying access waveguide width. In the simulations, the gap is taken to be constant and equal to half the distance between two pillars, i.e. $g = 0.5(a - 2r)$. Fig. 3.29 shows the transmission of TM and TE polarized light as a function of the access waveguide width w. The waveguide with is varied from a to $8a$. The length of the photonic crystal is 10 periods, as this is enough to prevent the TM polarization to pass through the photonic crystal. As was discussed before, a shorter photonic crystal has advantages with respect to the out-of-plane losses in actual applications.

The photonic crystal with the waveguide width of $7a$ results in a high transmission for TE polarization, i.e. -1.1 dB, while the TM polarization is completely blocked by the filter. Fig. 3.30 shows the wavelength-dependence of the selected TM filter from a 2D as well as from a 3D calculation. The results are similar, and the transmission of TE from the 3D simulation is as high as -3.4 dB, with an extinction ratio of almost 20 dB. The transmission of the TE polarization is high over a broad wavelength range, so the TM filter has a high bandwidth.

For the case of pillars in a polymer layer stack, the transmission of the TM filter as a function of the width of the access waveguides is shown in Fig. 3.31. Again, the transmission of the TM polarization is sufficiently suppressed after a photonic crystal length of 10 periods. The design with the highest transmission for TE is the one with an access waveguide width of $7a$, having a TE transmission of -11.5 dB. The lower TE transmission for the PiP TM filter as compared to the PiA TM filter is due to the
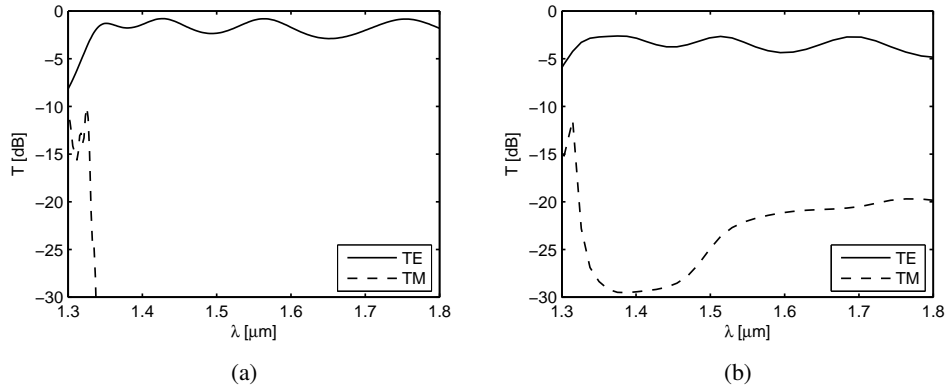
Figure 3.30: *TM and TE transmission spectra of a PiA photonic crystal-based TM filter of ten periods length and access waveguide width 7a, a) from a 2D simulation and b) from a 3D simulation.*

absence of a TE mode in the ΓX-direction in the wavelength region of interest, as can be seen in Fig. 2.6. The transmission spectra for TE and TM polarization of this design are shown in Fig. 3.32. These graphs reflect the fact that in ΓX-direction the TE modes have a stop band around $\lambda = 1.55$ µm. Therefore, the structure based on pillars in air has a better performance as a TM filter than the structure based on pillars in a polymer layer stack. However, the design could be adapted in such a way that at in the wavelength region of interest, the PiP photonic crystal has a band gap for TM polarization and a TE mode in the propagation direction.

3.4 Conclusions

In this chapter, several components were modeled and designed. The coupling between classical ridge waveguides and photonic crystal waveguides was optimized. For a simple butt coupler, the width of the access waveguide influences the coupling efficiency in two ways. The field profile of the ridge waveguide depends on its width, and also the effective refractive index or impedance of the the waveguide. The transmission of the coupler is affected by both properties. The gap between the classical waveguide and the photonic crystal waveguide only has a large influence in the case where both field profile and effective refractive index are well-matched to each other.

   Furthermore, the feasibility of using pillar photonic crystals for polarization filtering was demonstrated. Very short and efficient polarization filters can be realized with
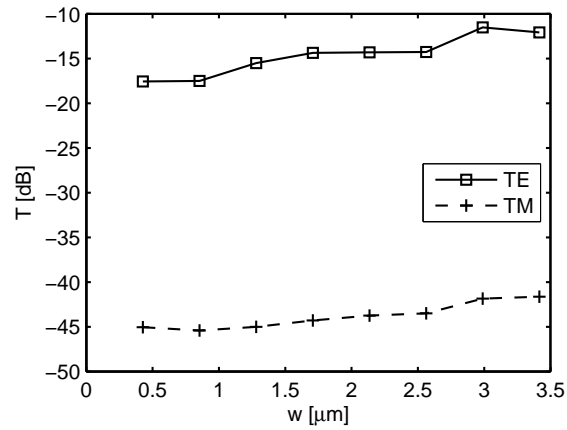
Figure 3.31: *TM and TE transmission of a PiP photonic crystal intersecting a ridge waveguide as a function of the access waveguide width.*

(a)	(b)
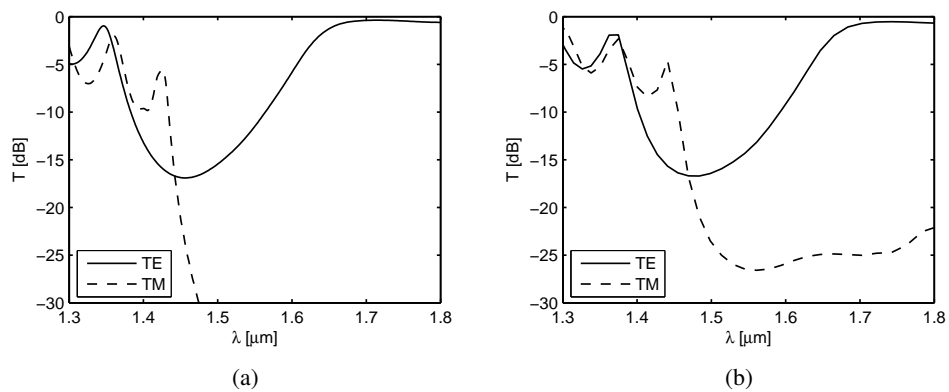
Figure 3.32: *TM and TE transmission spectra of a PiP photonic crystal-based TM filter of ten periods length and access waveguide width 7a, a) from a 2D simulation and b) from a 3D simulation.*

photonic crystals.

Chapter 4
Integration technology

The challenges of the integration of pillar photonic crystals with photonic integrated circuits that are based on classical waveguide technology, are describes in this chapter. Section 4.1 starts with an overview of the processing of the InP-based layer stack. A critical step in the control over the dimensions of the photonic crystals is the electron beam lithography, which is treated in detail in section 4.2. The combination of this type of pattern definition with the optical lithography that is normally used in classical integrated circuits is described in section 4.3. Finally, section 4.4 focuses on the implementation of the polymer layer stack.

4.1   Fabrication of photonic integrated circuits

In practical applications of photonic crystal based components, the integration with classical photonic integrated circuits is an important issue. In general, starting with an epitaxially grown InP/InGaAsP/InP layer stack, the fabrication of a PIC involves three main process steps: the deposition of the etch masking layers, the patterning of those masking layers and finally the etching of the waveguides and photonic crystals. These main process steps are first described in short, and once we have introduced the complete process flow the consecutive steps will be treated in more detail.

4.1.1   Basic processes

The fabrication process is a repetition of three general steps. Before describing the process flow these process steps are briefly introduced in this section.

Hard mask deposition. The first step in the fabrication process of integrated circuits is the masking layer deposition. Depending on the application, we can make use of metal and dielectric layers. Metal layers can be sputtered or evaporated on the sample. In our case, an e-beam evaporation tool is available for the evaporation of chromium (Cr). Dielectric layers, like silicon oxide (SiO_2), are applied using plasma enhanced chemical vapor deposition (PECVD).

Lithography. The second basic fabrication step is the pattern definition. To transfer the designed pattern onto the masking layers, either optical or electron beam (e-beam) lithography is used [51]. The sample is spin coated with a resist that is photosensitive in the case of optical lithography or electronsensitive if e-beam lithography is used. After exposure and developing, the desired pattern is transferred to the resist layer.

Etching. After the lithography, the patterned resist can either directly be used as a mask for etching the underlaying layers, or it can be used to define a metal mask by lift-off. In the latter case, a metal is evaporated on the sample with patterned resist. If the resist is now removed by a solvent, a patterned metal layer remains on the sample, which can then be used as a mask layer for etching.
Four different etching processes are used, depending on the specific application. A reactive ion etching (RIE) process with a CHF_3 is used to transfer the pattern of a metal layer to a SiO_2 masking layer. A second RIE process uses methane-hydrogen ($CH_4 : H_2$) chemistry to etch InP at relatively low etching speed [7]. An inductively coupled plasma (ICP) RIE system can be applied
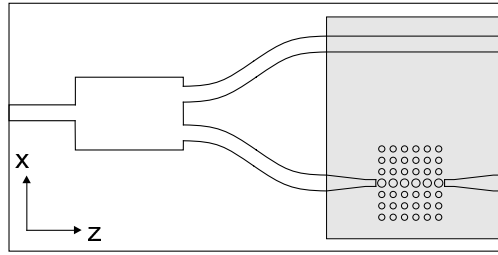
Figure 4.1: *Schematic drawing of the PIC where the gray area is defined by e-beam lithography.*

either to open Cr layers with chlorine-oxygen ($Cl_2 : O_2$) chemistry or to perform the deep etch of the InP/InGaAsP/InP layer stack with a chlorine-argon-hydrogen ($Cl_2 : Ar : H_2$) plasma [52].

In the next section, the full process flow until the deep etch of the pillars will be described in more detail.

4.1.2 Description of the fabrication process

A schematic top view drawing of the photonic integrated circuit including the photonic crystal component is shown in Fig. 4.1. To fabricate the photonic crystals along with the classical ridge waveguides in the same photonic circuit, the process is used that is shown in Fig. 4.2 and described in the following.

a) The fabrication process starts with an epitaxially grown InP/InGaAsP/InP wafer.

b) A silicon dioxide layer is deposited with PECVD (Oxford PlasmaLabsystem100) and a chromium layer is evaporated on top of that (Airco evaporator). The SiO_2 is a thick layer ($\simeq 430$ nm) which will be used as a mask layer for the final deep etching of the semiconductor stack. The Cr is used to open the underlying SiO_2 layer. It is a thin layer (50 nm), since its selectivity in the etching process with respect to SiO_2 is very high.

c) The second step is an optical lithography (Karl-Süss MA6) to define the ridge waveguides and the alignment markers for the following lithography steps (optical as well as e-beam, each requiring their own specific alignment markers – see also section 4.3). The resist pattern is used to open the thin Cr mask in the $Cl_2 : O_2$ ICP process (Oxford PlasmaLabsystem100).

83

(a) epitaxially grown semiconductor layer stack

(b) SiO$_2$ deposition

(c) waveguide definition

(d) etching markers in SiO$_2$

(e) opening Cr layer at e-beam fields

(f) etching markers in InP

(g) definition of photonic crystals

(h) Cr evaporation

(i) lift-off

(j) opening SiO$_2$ of completed waveguide pattern

(k) deep etching of the circuit

(l) implementation of the polymers

SiO$_2$ Cr   resist

InP   InGaAsP   PHFIPMA   Polyimide

Figure 4.2: *Process flow for the integration of ridge waveguides and pillar photonic crystals.*

d) After the pattern transfer to the Cr, the resist is removed and the sample is covered with a new photoresist layer. In the second optical lithography step, the e-beam write fields and e-beam markers are opened. The sample is first etched in the CHF_3 RIE process to open the SiO_2 of the e-beam markers. In this step, the areas that will be defined by e-beam lithography are covered by Cr and the ridge waveguides are protected by the optical resist.

e) Since the photonic crystal components will be defined by a lift-off process, the Cr in the e-beam write fields has to be removed. This is done in a second run of the $Cl_2 : O_2$ ICP process, which does not affect the InP surface of the e-beam markers that is now exposed to the etching plasma.

f) The markers are etched ~ 800 nm into the InP top cladding (Oxford PlasmaLabsystem100). For this etching step, the $CH_4 : H_2$ RIE process is used, to which the exposed SiO_2 of the e-beam write fields is very resistant.

g) The next step is the e-beam lithography (RAITH150). This is the most critical step in the processing, as it defines the photonic crystal components. It is treated in detail in section 4.2.

h) After the resist has been patterned, a new Cr layer of 50 nm is evaporated.

i) The lift-off is performed. The sample is now covered with a thick SiO_2 layer, on which a patterned Cr layer defines the classical ridge waveguides as well as the photonic crystal components. In Fig. 4.3 a SEM photograph of the Cr mask after lift-off is shown.

j) The Cr pattern is transferred to the SiO_2 by a CHF_3 RIE process (Oxford PlasmaLabsystem100).

k) Finally, $Cl_2 : Ar : H_2$ ICP plasma is used to perform the deep etch of the complete waveguide pattern [52]. Fig. 4.4 shows a SEM image of a cross section of a photonic crystal waveguide after the final ICP etch. The required etchdepth of 3 µm, as calculated in section 2.4.2, is reached using this process. The photonic crystal waveguide is connected to a ridge waveguide that is also visible in the SEM picture. After removal of the remaining SiO_2, the semiconductor chip is finished.

l) a uniform polymer or a three-layer polymer stack can be implemented. This is described in section 4.4.

85
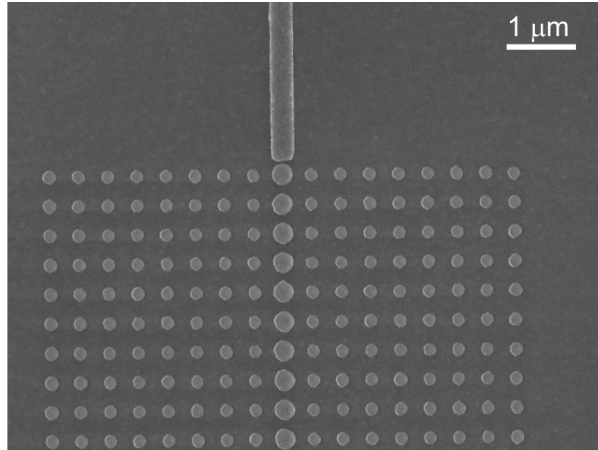
Figure 4.3: *SEM image of the Cr mask of a PhC waveguide and an access ridge waveguide directly after lift-off.*
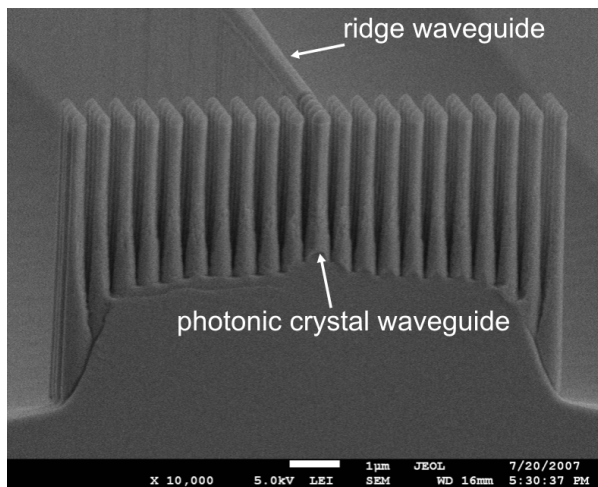
Figure 4.4: *SEM image of a cross section of the etched photonic crystal waveguide that is connected to a ridge waveguide. The etch depth is ≥ 3 μm. The SiO_2 mask has not yet been removed.*

After these process steps the chips can be cleaved and are ready for characterization.

4.2 Electron beam lithography

The structures with critical dimensions, i.e. the photonic crystals and the coupling structures with classical ridge waveguides, are defined using electron beam lithography (EBL). Since it is more convenient to expose the access waveguides and the pillars, instead of the surrounding area, and taking into account that a positive tone e-beam resist is available, we chose a lift-off process to define the etching mask (see Figs. 4.2(g)–4.2(i)).

In e-beam lithography, a beam of electrons scans a part of a sample covered with e-beam resist and directly 'writes' the desired pattern onto the sample. The beam consists of electrons that are accelerated with a voltage of 20 keV. The beam is switched on an off by a pattern generator. The maximum area that can be written in by the in-plane movement of the beam, at a fixed position of the sample stage, is the so-called write field. The write field size can be chosen from several micrometers up to several hundreds of micrometers. The magnification depends on the size of the write field. The smaller the write fields, the larger the magnification and the better the resolution. However, if a pattern design is larger than the size of a write field, the sample holder has to move from one write field to the other. This movement may cause stitching errors: offsets in the pattern at the write field boundaries. In this work, a write field size of 200 µm is chosen. The photonic crystal devices fit completely in the area of the write fields, even including the access ridge waveguides and tapers. Therefore, stitching errors are no issue in our fabrication process. The minimum possible beam step size is determined by the write field size and the pattern generator. In the realizations, a beam step size of 6.4 nm is used.

To prevent charging of the resist layer by the incoming electrons, the resist is covered with a thin layer of gold ($\simeq 12.5$ nm) prior to the exposure. In an e-beam evaporator, the resist might be unintentionally exposed to electrons. Therefore, the gold has to be evaporated thermally. After the resist has been exposed, the gold layer is removed by a $KI : I_2$ solution and the resist can be developed.

In e-beam lithography, the beam of electrons is focussed onto the resist surface to a diameter of about 2 nm according to specifications. In reality the resolution of the exposure is limited by forward scattering and the generation of secondary electrons. The forward scattering can be reduced by decreasing the resist thickness or by increasing the acceleration voltage. However, since the resist is used for lift-off, the forward

87

scattering might be of an advantage since a slight overhang creates a better lift-off profile in the resist. In a lift-off process, as a rule of thumb the resist should be at least two times as thick as the metal layer that will be evaporated. For the evaporation of a Cr metal layer of 50 nm, a PMMA resist layer of 200 nm is used, which is exposed with an acceleration voltage of 20 keV. With these exposure parameters, the effects of forward scattering and secondary electron generation together induce a beam broadening in the order of 20 nm, as is confirmed by measurements. For small features, this critical dimension loss should be compensated for by reducing the dimensions in the design.

Apart from secondary electrons, primary electrons can have energies that are high enough to fully penetrate the resist and be reflected at the interfaces of the underlying material stack. If the pattern features are close together, these so-called backscattered electrons can add an extra dose to the neighboring features. This is called the proximity effect. The software of the available e-beam lithography tool is accompanied by proximity effect correction software, which corrects the doses that are attributed to the features in the design for proximity effects. The proximity effect largely depends on the layer stack that is exposed, therefore the parameters for the proximity effect correction program have to be determined experimentally for each layer stack.

4.3   Combining optical and e-beam lithography

For the optical lithography, a mask aligner with a mercury light source is used ($\lambda =$ 405 nm). The resolution of the optical lithography is good enough to meet the requirements for the classical waveguides and devices, and it is a relatively fast process. However, the resolution is not sufficient for devices based on photonic crystals, with typical lattice constants of 0.5 µm. For these devices electron beam (e-beam) lithography is applied. The resolution of e-beam lithography is better than that of optical lithography, at the cost of process speed.

The alignment accuracy of optical lithography is at best in the order of 200 to 300 nm, whereas that of the e-beam lithography can be as good as 10 nm. Therefore, the best alignment is obtained by first defining the waveguides and alignment markers in the same optical lithography step, and aligning the e-beam to this pattern for the definition of the critical features.

The alignment accuracy of the e-beam largely depends on the quality of the markers. The markers are crosses with arms that are 10 µm long and 0.5 µm, wide as shown in Fig. 4.5. The secondary electrons coming from the marker areas are detected with an in-lens detector. In an automatic alignment procedure, the electron beam scans over one of the arms of a marker, while the contrast in secondary electrons is recorded.
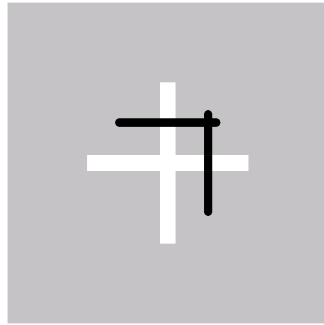
Figure 4.5: *Alignment marker for e-beam lithography. The gray area is defined in the same optical lithography step as the waveguides. The black lines are the automatic scans to locate the center of the marker.*

From this scan, the center line of the cross' arm can be determined. By scanning two of the arms of the marker cross, the position of its center can be determined. This procedure results in a highly accurate alignment, but it requires a high contrast between the marker cross and its background.

Ideally, the opened Cr pattern in Fig. 4.2(b) would have a good enough contrast with the underlying SiO_2 in the SEM, even when covered with the e-beam resist. The contrast is determined by the secondary electron yields of the different materials, and on the topography of the sample. Although Cr has a higher atomic number than Si and O, the masking layer is only 50 nm thick and it is almost transparent to electrons at an acceleration voltage of 20 keV. Opening the SiO_2 layer of $\simeq 430$ nm does not give enough contrast to the underlying InP either. Therefore, the markers have to be etched in the InP ($\simeq 800$ nm) to give sufficient contrast for an automatic alignment procedure. The additional optical lithography steps that are needed to etch the markers are not critical and they do not induce additional alignment inaccuracy to the process.

Fig. 4.6 shows two photographs of the transition between ridge waveguides defined with optical lithography and ridge waveguides defined by EBL. The optically defined ridge waveguides have a width of 0.8 μm, whereas the ridge waveguides in the e-beam write field are slightly wider. An offset, however, is not visible by optical microscopy. This means that the alignment accuracy is better than 50 nm.

(a)   (b)
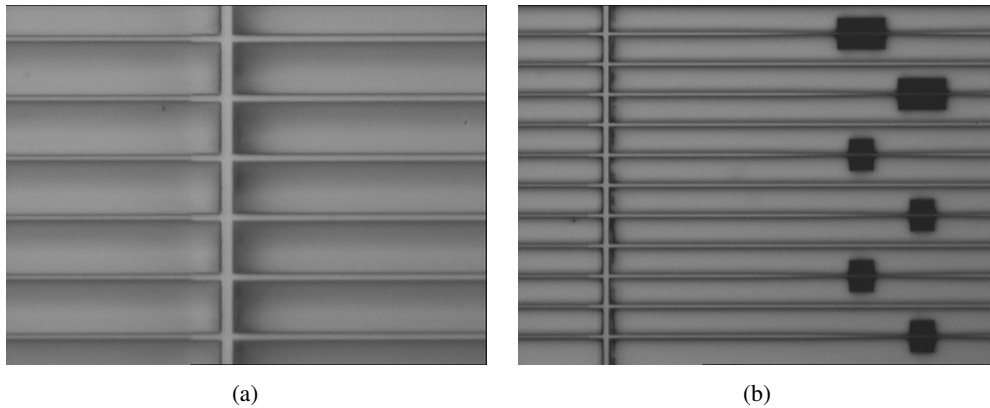
Figure 4.6: *Optical microscope pictures of the transition between optically defined waveguides (left-hand sides of both photographs) and structures defined by EBL (right-hand sides). The ridge crossing the waveguides at the border of the e-beam write field is due to the mask set which was not optimized for this process flow. It can and should be removed in future designs to reduce losses and reflections at the transitions.*

4.4 Implementation of a polymer layer stack

The implementation of the polymer layer stack is schematically shown in Fig. 4.7. The semiconductor structures are first planarized by spin coating a low-index polymer. After the spin coated polymer layer is cross linked by a hard bake, it is etched back to the desired height between the pillars. The second, high-index polymer, is applied in the same way, and the layer stack is finished by spin coating the third layer, which is again the low-index polymer. For passive structures there is no need to etch back the last polymer layer. However, metal contacts can be placed on top of the pillars if the third polymer layer is etched back to their top surface level. This opens possibilities for realizing active photonic crystal components in pillar-based structures. In the next sections, the processing of the two types of polymers is treated.

4.4.1 PHFIPMA – the low index polymer

The low-index polymer is poly(1,1,1,3,3,3-hexafluoroisopropyl) methacrylate (PH-FIPMA). It is selected because of its low index (1.38) and its transparency for wavelengths around 1550 nm[1]. The polymer is dissolved in tetrahydrofuran (THF) at a

---

[1]The selection of the low-index polymer was done in collaboration with the Polymer Technology group of the Faculty of Chemical Engineering at the TU/e.

(a)

(b)

(c)

(d)

(e)

(f)

InP InGaAsP PHFIPMA Polyimide
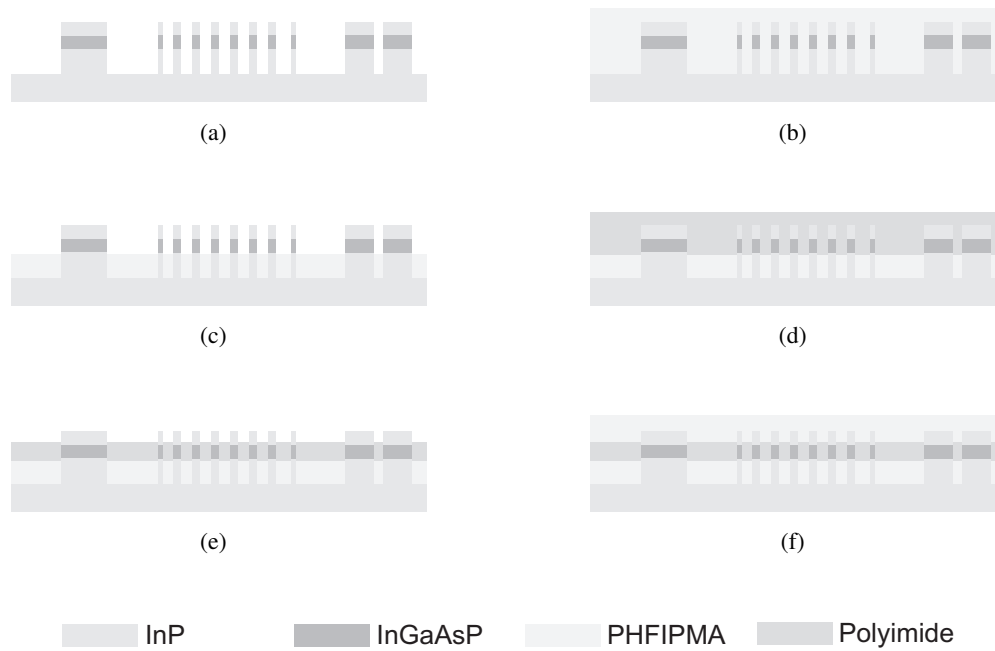
Figure 4.7: *Process steps for the implementation of the polymer layer stack.*
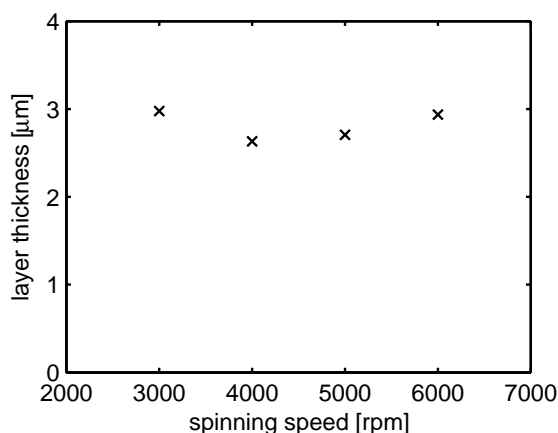
Figure 4.8: *PHFIPMA layer thickness as function of spinning speed. Thickness is measured by ellipsometry after soft bake.*

weight ratio of 1:2. After spin coating we apply a soft bake to remove the solvent from the polymer layer. The soft bake consists of five minutes at 30°C on a hotplate, increasing the temperature to 40°C and then increasing the temperature in steps of 20°C up to 100°C, keeping the temperature constant for five minutes at each step. If the temperature increases too fast, bubbles are captured in the polymer layer.

The layer thickness that is obtained after spin coating and soft baking the polymer, depends on the spin speed. Fig. 4.8 shows the spin curve of the low index polymer after the soft bake, giving the layer thickness after the soft bake as a function of the spin speed.

To determine the thermal stability of the polymer, especially the hard bake temperature to cross link the polymer, a thermogravimetric analysis (TGA) is carried out. A sample of the polymer is kept under a constant nitrogen flow. The weight of the sample is monitored on a sensitive balance as the sample temperature is continuously increased at a rate of 10°C/min. Fig. 4.9 shows the TGA result up to 500°C. The steep descent at temperatures below 50°C indicates evaporation of the solvent THF. At temperatures above 200°C, where the slope of the curve bends further downwards, the polymer decomposes. The steep descent of the curve above 300°C indicates evaporation.

The polymer layer is hard baked in an oven under nitrogen flow. As can be seen from the TGA graphs, the polymer should not be heated above 200°C during hard baking, to prevent degradation. To determine the required hard bake time, a sample is
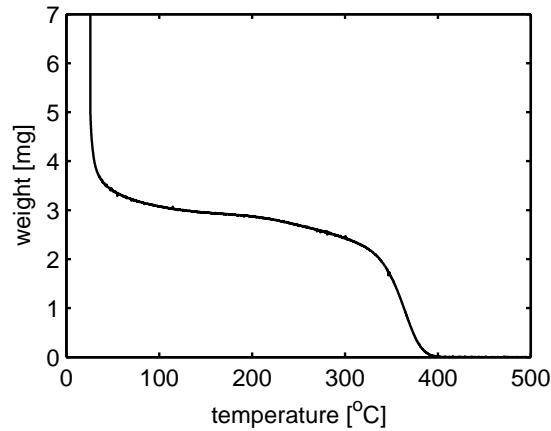
Figure 4.9: *Thermogravimetric analysis of the low-index polymer PHFIPMA.*

baked for two hours in steps of 30 minutes, measuring layer thickness and refractive index after each bake step using ellipsometry, see Fig. 4.10(a). As the sample was not measured at exactly the same location after every bake step, the thickness slightly varies. The graph shows that the influence of the hard bakes on the layer thickness and on refractive index is small. If the structure is not sufficiently planarized, more layers can be spin coated onto the sample. The additional hard bakes that are thus involved, do not significantly influence the eventual refractive index of the PHFIPMA. Fig. 4.10(b) gives the dispersion curve, i.e., the refractive index as function of wavelength, of PHFIPMA after 60 minutes hard baking at 200°C. In the wavelength region of interest (1530–1570 nm), the refractive index is constant, although slightly higher than specified by the supplier (i.e. 1.386 instead of 1.38).

After planarizing a photonic crystal sample with PHFIPMA, the polymer is etched back to the desired height. To accurately control the thickness of the layer between the pillars, the polymer is etched isotropically by a plasma of a O_2 and CF_4 mixture, until the desired thickness is reached. The etch rate of the selected polymers is controlled by adapting the etching gas ratio of O_2 and CF_4, where the total gas flow is kept constant at 100 sccm. In the etching back, a gas mixture of 70 sccm O_2 and 30 sccm CF_4 was used, resulting in a pressure of 1.6 mbar. The power is 70 W. For these conditions, the etch rate hardly depends on gas composition. In this way, the polymer layer will remain flat even close to the pillars, where gas composition might change due to the near presence of the InP surface. The sample is etched no longer than two minutes at a time to prevent heating effects.
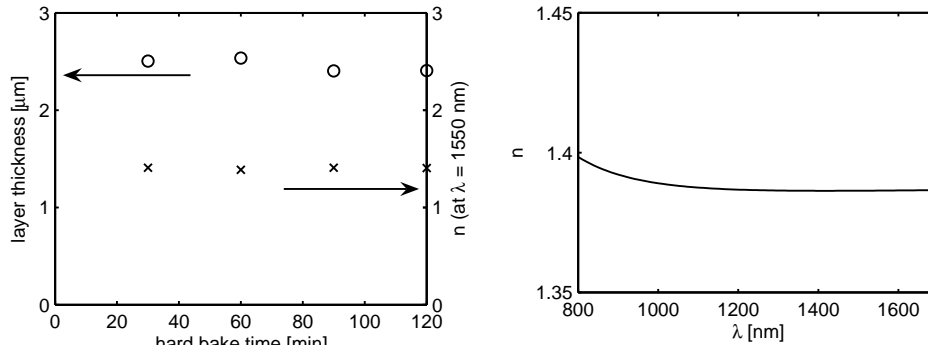
Figure 4.10: *a) PHFIPMA layer thickness and refractive index (at* $\lambda = 1550nm$) *as a function of hard bake times. The sample is baked at 200°C under nitrogen flow in steps of 30 minutes. b) PHFIPMA dispersion curve after 60 minutes hard bake at 200°C under nitrogen flow.*

The etching back of the polymer using the $O_2 : CF_4$ plasma causes roughness at the surface of the polymer. This roughness can be reduced by applying an extra hard bake. This hard bake should be carried out when the polymer is still covering the semiconductor structures. To limit the number of (roughness-inducing) etch back steps after the final hard bake, it should be performed when the colored interference pattern is just visible.

Fig. 4.11 shows two SEM image of an InP sample with an etched photonic crystal that was planarized by spin coating several layers of PHFIPMA. After planarization the PHFIPMA was etched back using the described recipe. The etching between the pillars and in the large open area next to it, does not significantly vary in etch rate. Therefore, the etch depth in the photonic crystal fields can be accurately controlled by monitoring the etch depth of larger structures that can be scanned using a conventional profilometer.

4.4.2   PI2737 – high index polymer

For the high-index polymer layer, the polyimide PI2737 was selected. It is used in other processes for planarization and passivation purposes [53]. It is transparent at the operating wavelength [54], having a refractive index of 1.64.

Due to the etching back with a $O_2 : CF_4$ plasma, the top surface of the low-index polymer is oxidized. A good adhesion of the polyimide onto the PHFIPMA is obtained by exposing the low-index polymer to a CHF_3 plasma at 50 W for 1 minute (60 sccm gas flow and $P = 15$ mTorr). This treatment does not change the thickness of the
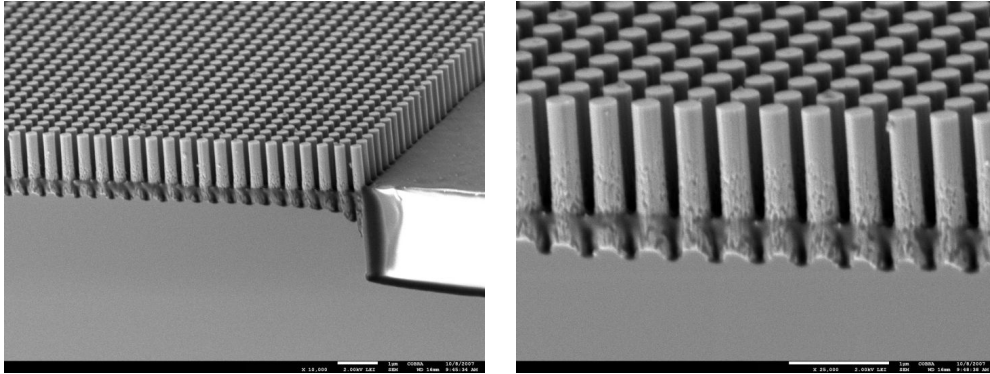
Figure 4.11: *SEM pictures of a PhC field that was planarized with PHFIPMA and etched back to a depth of ∼1.65 µm. The lattice constant of the photonic crystal is 443 nm.*

low-index polymer layer, but instead it deposits a very thin layer of polymer, covering the oxide on the polymer surface. The thin polymer layer increases the contact angle of a droplet of water from $\sim 70°$ to 95°, so it makes the surface less polar. It then provides a good adhesion of the non-polar polyimide. Fig. 4.12 shows a SEM image of a planarized polyimide layer on a pillar photonic crystal in which the PHFIPMA had been etched back before. The photograph shows no air bubbles being captured between the layers and the adhesion is excellent.

For the planarization with PI2737 the standard process is applied [55]. However, in the standard hard bake the sample is heated to 350°C for 45 minutes, while the low-index polymer is not to be heated to a temperature higher than 200°C. At a lower temperature, the cross-linking of the polyimide is slower, so the hard bake time should be increased. Therefore, the hard bake is changed to two hours at 200°C under nitrogen flow. After two hours the polyimide is stable. Several layers have to be spin coated onto the sample to planarize the step heights of ~ 1.65 nm.

The dispersion curve of the polyimide using this recipe is shown in Fig. 4.13. The refractive index at 1550 nm is $\simeq 1.61$. This is lower than expected due to the lower hard bake temperature of 200°C instead of the standard 350°C.

The etching back of the polyimide is based on the same principles as for the low-index polymer. A gas mixture of O_2 and CF_4 is used, but now at a power of 300 W and a total gas flow of 50 sccm.
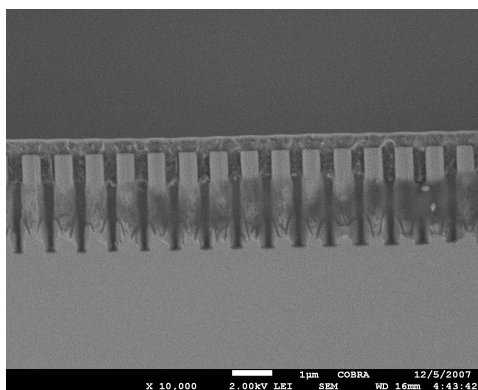
Figure 4.12: *A photonic crystal with an etched back layer of PHFIPMA and a planarized layer of PI2737.*
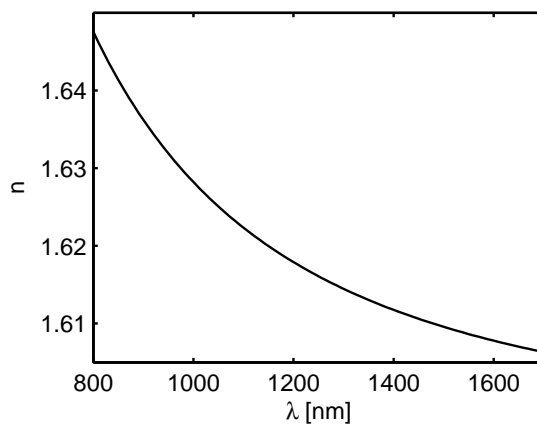
Figure 4.13: *Measured PI2737 dispersion curve after hardbake.*
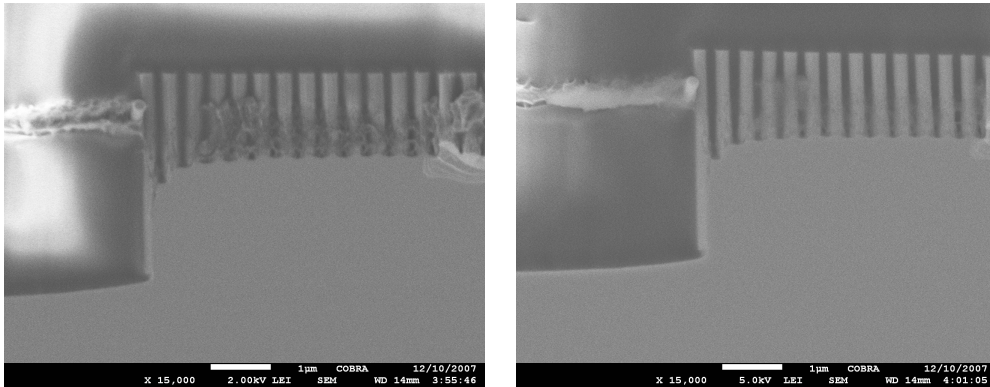
Figure 4.14: *SEM pictures of a PhC field with the three polymer layers. The lattice constant of the photonic crystal is 443 nm.*

4.4.3 Three-layer stack

To complete the layer stack, the low-index polymer is spin coated onto the sample after the etching back of the polyimide. The adhesion of the PHFIPMA onto the polyimide after etching back is excellent, implying that no additional process steps are needed. Fig. 4.14 shows the SEM photograph of a pillar photonic crystal with the full polymer layer stack.

If the polyimide would not have been present (e.g. if the polyimide would have been thinner inside the photonic crystal), the PHFIPMA would have been underetched in the $O_2 : CF_4$ plasma over a distance of micrometers. The resulting holes underneath the polyimide would not have been completely filled with the last layer of PHFIPMA. This leads to the conclusion that the polyimide layer is present between the low-index layers also inside the photonic crystal, although it may not be clearly visible from the SEM pictures.

Chapter 5
Chip design and characterization

In the previous chapters, different photonic crystal waveguides were designed and modeled. Furthermore, a fabrication technology was developed that combines the realization of photonic crystals and that of ridge waveguides in a compatible process. In this chapter, the realized devices are described, along with the results that are obtained by transmission measurements.

In section 5.1, the design of a chip is described on which both types of waveguides are integrated, with an overview of the designed photonic crystal waveguides. The measurement setup is described in section 5.2. The results of the characterized devices are given in section 5.3. In section 5.4, conclusions are drawn.
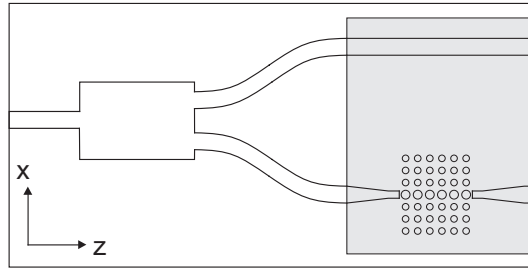
Figure 5.1: *Schematic drawing of the chip layout (not to scale), where the grey area is defined by e-beam lithography.*

5.1 Circuit design

The optical circuit design, as schematically shown in Fig. 5.1, consists of a 2-μm-wide input ridge waveguide, followed by a 1×2 multimode interference coupler (MMI) splitting the light into two branches. In the reference branch, the light propagates through a classical ridge waveguide towards the output side of the chip. The other branch contains a photonic crystal waveguide. This configuration has two major advantages; first, the incoupling of light into the input waveguide can easily be optimized using the reference branch, even if the photonic crystal waveguide has high losses, and secondly, the transmission of the photonic crystal waveguide can directly be calculated from a comparison with the transmission of the reference arm.

The optically defined waveguides on the realized chip have a width of 1.8 μm instead of the designed 2 μm. This critical dimension loss is due to deviations in the fabrication process, mainly a slight overexposure in the optical lithography defining the waveguides. At the chip facets, the waveguides are 25 μm apart, which is enough to separately determine the optical output powers. The MMIs are designed to have a large bandwidth. Reflections from the MMI are reduced by adapting the design to have tilted corners [56].

The e-beam write fields are 200×200 μm^2 in size. Markers need to be placed in each corner of the write fields. The size of the markers is 20×20 μm^2, leaving a width of 160 μm for the waveguides that are defined by e-beam lithography. The waveguides are placed next to each other with a pitch of 10 μm. Since the waveguides are deeply etched into the InP substrate, this spacing assures that cross talk between the waveguides is prevented. At the transitions, the optically and e-beam defined waveguides have a longitudinal overlap of 5 μm. The width of the waveguides at the transitions is designed to be 1 μm, but due to fabrication errors this width is reduced to about

800 nm in the realized devices.

Within the e-beam write fields, the reference waveguide is a straight waveguide, directly connected to the opposite output waveguide. Its width remains 1 μm over this distance. The other ridge waveguide is first adiabatically tapered to the width that matches the diameter of the photonic crystal waveguide (i.e., $w = 2r_{\mathrm{d}}$). The waveguide width is then kept constant over a distance of 4 μm, after which the photonic crystal waveguide starts. At the opposite side of the photonic crystal waveguide, the width of the ridge waveguide is kept equal to the diameter of the pillars of the photonic crystal waveguide over a distance of 4 μm, and then adiabatically tapered to the width at the transition to the optically defined ridge waveguide. The photonic crystal waveguides are placed 10 μm off the center of the write fields. If the reflections at the transitions are high, and so are the reflections at the interfaces between ridge and PhC waveguides, this can be identified by two cavities which can be distinguished.

For the photonic crystal waveguides that were optimized for pillars in air, two waveguide defects were selected, both having a lattice constant $a = 491$ nm and a background pillar radius $r = 123$ nm. One waveguide defect has a radius of $r_{\mathrm{d}} = 170$ nm and the other one has $r_{\mathrm{d}} = 210$ nm (see chapter 2). Photonic crystal waveguides of 8, 16 and 32 periods length are placed on the mask for both of these designs. From the transmission measurements on these structures, the insertion loss can be determined as a function of the length of the PhC waveguide. Furthermore, photonic crystal waveguides with a fixed length of 16 periods and with varying defect radius are placed on the mask. With these structures, the transmission of the photonic crystal waveguides can be compared to the band diagrams of the corresponding waveguides. Furthermore, if the fabrication process introduces deviations on the dimensions of the structures, these can be determined by characterizing the PhC waveguides with varying defect radii. PhC waveguides with $r_{\mathrm{d}} = 160, 170, 180, 190, 200$ and 210 nm are designed.

The photonic crystal waveguide that was optimized for pillars with a polymer slab waveguide in between, only one defect radius was selected, consisting of a lattice with $a = 427$ nm, $r = 107$ nm and a defect radius of $r_{\mathrm{d}} = 155$ nm (see chapter 2). PhC waveguides with lengths of 4, 8, 16, 32 and 64 periods are present on the mask. As with the PhC waveguides that were optimized for pillars in air, the defect radius is also varied. In this case, waveguides with $r_{\mathrm{d}} = 145, 155, 165, 185, 195$ and 205 nm are present.

5.2 Measurement setup

Light from a tunable laser source is coupled into the input waveguide using a microscope objective. The polarization is fixed to TM or TE by use of a polarizer. At the

output side, the transmitted light is collected with a lensed fiber. The collected light is measured by a photoreceiver. After optimization of the in- and outcoupling alignment at $\lambda = 1550$ nm, the tunable laser scans the wavelength from 1530 to 1570 nm in steps of 0.1 nm.

The cleaved facets of the chip introduce Fabry-Pérot fringes on the measured spectrum. These are averaged out by taking a running average over 10 data points of the spectrum. From the averaged spectra of both the branches, the transmission of the photonic crystal waveguide is determined. The transmission losses include the tapering of a waveguide from 0.8 μm width down to the diameter of the defect pillars, the coupling to and from the photonic crystal waveguide and the propagation loss of the photonic crystal waveguide.

5.3 Transmission of photonic crystal waveguides in air

5.3.1 Transmission as a function of the waveguide length

The measured transmission as a function of the length of the photonic crystal waveguides (in periods) is shown in Fig. 5.2. The transmission of each PhC waveguide is averaged over the scanned wavelength range, and the bars indicate the standard deviation from the mean value over this wavelength range. The transmission of the photonic crystal waveguides that are 32 periods long is so small, that it can not be measured very accurately. However, it can be concluded that the propagation losses dominate over the coupling loss between both types of waveguide.

Extrapolating the measurement data of the shorter waveguides ($N = 8$ and $N = 16$ periods) for both waveguides, the coupling loss for $r_d = 170$ nm seems slightly higher than in the case of $r_d = 210$ nm. This is in agreement with the simulations that are described in section 3.2. Furthermore, the propagation losses of the waveguide with $r_d = 170$ nm is 1.5 dB/period, whereas that of the waveguide with $r_d = 210$ nm is 1.2 dB/period. This difference will be partly due to the difference in diffraction losses; the smaller the radius of the defect pillars, the larger the air region in between the adjacent pillars. The effect of the defect radius on the transmission is further discussed in section 5.3.3. The losses are too high for practical applications, but the implementation of the polymer layer stack is expected to impose a huge reduction of the propagation losses (see section 2.4.3).
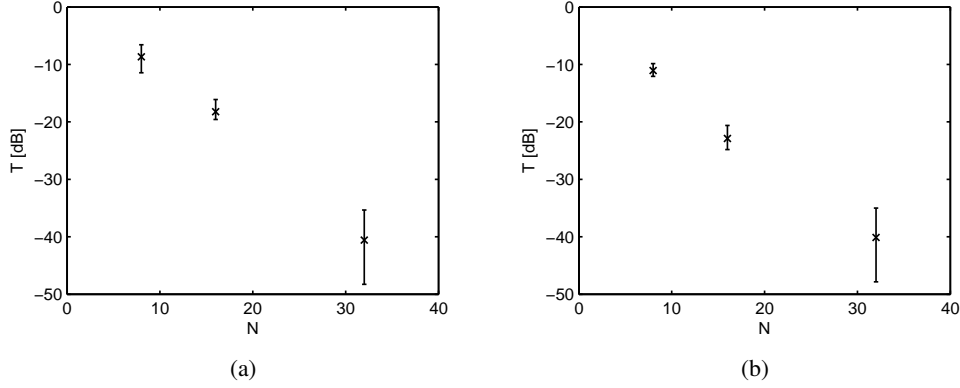
Figure 5.2: *Transmission of pillar photonic crystal waveguides as a function of the length of the waveguide in periods with a defect radius of a)* $r_d = 210$ *nm, and b)* $r_d = 170$ *nm.*

5.3.2 Polarization dependence of a photonic crystal waveguide

In section 3.3 the suitability of pillar photonic crystal waveguides as polarization filters was discussed. From 2D simulations, the TE filter giving the best performance was the structure of pillars in air with $a = 491$ nm, $r = 123$ nm and $r_d = 210$ nm (see Fig. 3.23). In Fig. 5.3(a), the simulated transmission of an 8-period-long photonic crystal waveguide with the same geometrical parameters is plotted on a logarithmic scale. The measured transmission of such a structure is given in Fig. 5.3(b).

The modulation on the TE polarized transmission is due to the reflections at the transitions between the ridge waveguides and the PhC waveguides, and to the reflections at the transitions between the optically defined waveguides and the e-beam defined ones. The latter reflections can be eliminated by adapting the design of the chip. The average transmission for TE polarization is -26.5 dB, whereas that of TM polarized light is -8.7 dB. This implies that an extinction ratio of about 18 dB should be feasible if the reflections are reduced, while the length of the device is limited to $8 \cdot 0.491 \simeq 3.9$ µm.

5.3.3 Effect of defect radius and band structure on the transmission of a photonic crystal waveguide

Photonic crystal waveguides with varying defect radii were realized on the chip. Each waveguide defect has different guided modes inside the band gap. Fig. 5.4 shows the calculated 2D band diagrams of line defects with varying radius of the defect pillars
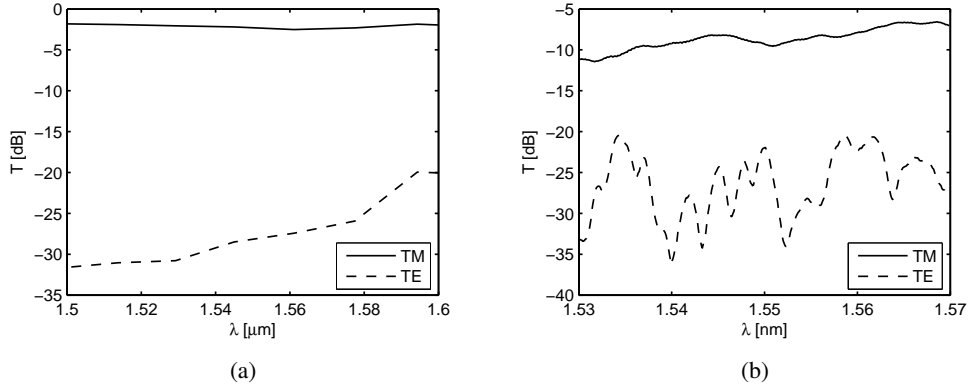
Figure 5.3: *Transmission of a TE filter based on a pillar photonic crystal waveguide in air, a) simulated TE and TM transmission and b) measured TE and TM transmission of a waveguide of 8 periods length and a defect radius of $r_d = 210$ nm.*

(r_d). To account for the third dimension, the effective refractive index of the pillars is used. The waveguide mode with a monotonically decreasing dispersion curve has an even mode profile, whereas the mode with the increasing dispersion curve has an odd symmetry. For increasing defect pillar radius, the frequencies of both the modes are reduced due to the higher average refractive index of the line defect.

Fig. 5.5 shows the measured transmission through a 16-period-long PhC waveguide as a function of the defect pillar radius. The transmission of each PhC waveguide is averaged over the scanned wavelength range, and the bars indicate the standard deviation from the mean value over this wavelength range. As we saw in section 5.3.1, the transmission is dominated by the propagation losses. The dependence of the loss on the defect pillar radius can not be explained by only diffraction effects, since in that case the transmission would monotonically increase with the defect radius. However, it can be understood by comparison with the in-plane propagation constants k_z and the group velocities v_g of the guided modes. For convenience, the calculated group velocities of the guided modes are plotted in Fig. 5.6. Note that the even mode has a higher group velocity than the odd mode. If the group velocity is low, the light propagates relatively slowly through the waveguide, resulting in longer interaction times with the crystal and therefore in higher losses [50].

For a defect radius as small as $r_d = 160$ nm the even mode is the only guided mode (see Fig. 5.4(a)), but this mode is approaching the slow light regime and therefore exhibits the lowest transmission. Also, the mode is very close to cut-off, and if the
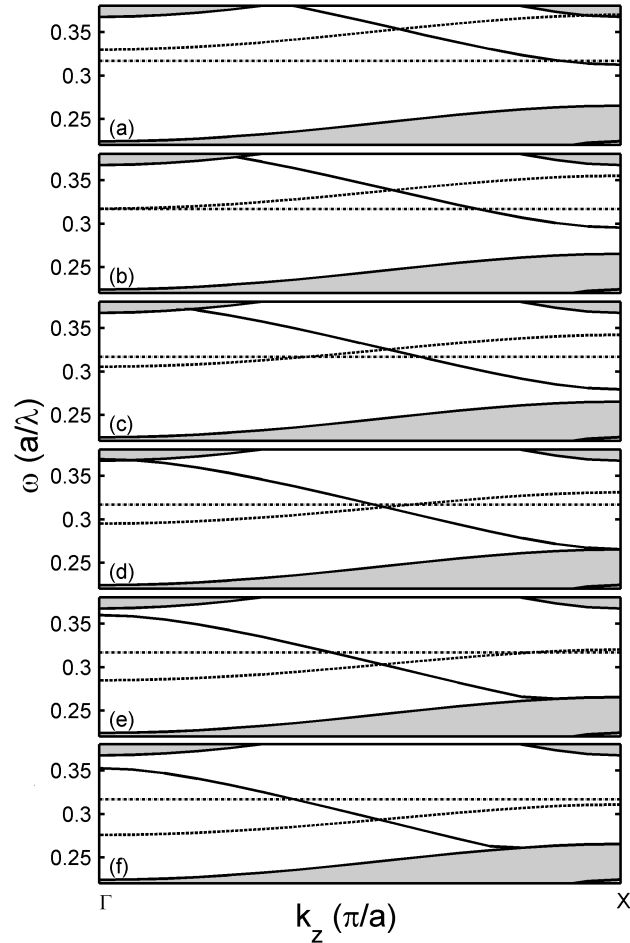
Figure 5.4: *Comparison of band diagrams for varying defect pillar radius: a) $r_d = 160$ nm, b) $r_d = 170$ nm, c) $r_d = 180$ nm, d) $r_d = 190$ nm, e) $r_d = 200$ nm and f) $r_d = 210$ nm. The grey areas indicate the PhC modes supported by the surrounding photonic crystal. The solid lines belong to the even waveguide mode, the dashed line to the odd waveguide mode, and the dash-dotted line represents the frequency corresponding to $\lambda = 1550$ nm. Note that both guided modes are pushed down in frequency, caused by the increase in average refractive index as the defect radius gets larger.*
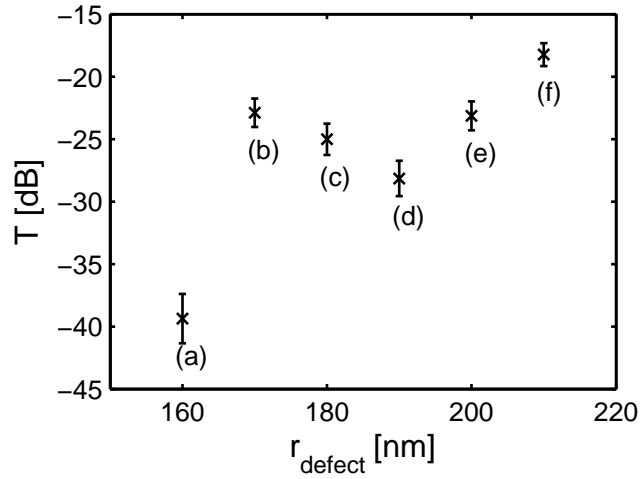
Figure 5.5: *Measured transmission of a 16-period-long photonic crystal waveguide as a function of the radius of the defect pillars. The notations (a) to (f) refer to the corresponding band diagrams of Fig. 5.4.*
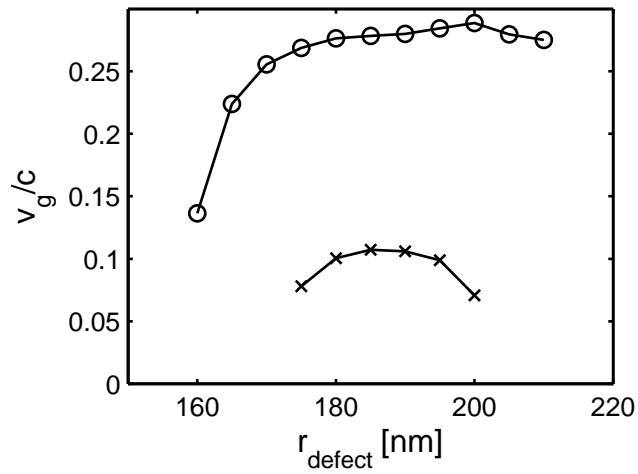
Figure 5.6: *Group velocities of both the even mode (circles) and the odd mode (crosses) as a function of the defect pillar radius at $\lambda = 1550$ nm.*

defect radius is only 5 nm smaller in the realized device, no guided mode is present and the PhC has a band gap at $\lambda = 1550$ nm. For a defect radius of 170 nm, as shown in Figs. 5.4(b) and 5.6, the odd mode is absent at $\lambda = 1550$ nm and the even mode has a high group velocity. This results in relatively low PhC waveguide losses. Increasing the defect radius to 180 nm introduces the odd mode at $\lambda = 1550$ nm (see Fig. 5.4(c)), which might be excited if the symmetry of the structure is broken, e.g. by fabrication imperfections. Apart from the lower group velocity, this mode is not matched to the output ridge waveguide, and it will exhibit high coupling losses. Indeed, the measured losses are higher than those of a waveguide with $r_\mathrm{d} = 170$ nm.

For a waveguide with $r_\mathrm{d} = 190$ nm, the crossing of the even and the odd mode is close to the frequency corresponding to $\lambda = 1550$ nm. The k_z-vectors of both the modes are nearly equal, and light can easily couple from one mode to the other (e.g. induced by fabrication imperfections), resulting in even higher loss. Increasing the defect radius to $r_\mathrm{d} = 200$ nm increases the difference between the k_z-vectors of the modes and the situation is comparable to that of $r_\mathrm{d} = 180$ nm. Finally, for $r_\mathrm{d} = 210$ nm, the odd mode is cut off and the even mode has a high group velocity. This is the PhC waveguide with the highest transmission.

The measured transmission of a PhC waveguide based on pillars is in good agreement with the 2D band diagram simulations of the line defects. This implies that the fabrication technology can be accurately controlled, which is crucial if more complicated PhC components are designed. The highest transmission, -18 dB for a 16-period-long photonic crystal waveguide, is obtained for waveguides where mode crossings and slow light propagation are avoided.

5.4 Conclusions and discussion

Pillar-based photonic crystal waveguides can successfully be integrated in photonic integrated circuits. Photonic crystal waveguides based on single line defects of different lengths are characterized and their behavior is in agreement with simulations. The propagation losses are 1.2–1.5 dB/period. The large difference of the measured propagation loss and the predicted values from the simulations, can have various causes. First, the scattering losses may play a role due to sidewall roughness of the structures. Second, the pillars may to some extend be conically shaped, resulting in high loss due to substrate leakage [57, 58]. And finally, small irregularities may be introduced in the photonic crystal lattice causing a distortion of the guided Bloch mode. These issues can all be solved by further development and optimization of the fabrication technology.

A short ($<$ 4 µm) TE polarization filter was realized and characterized. The extinction ratio is in the order of 9.7 dB with an insertion loss for TM polarized light of 8.7 dB. However, by optimizing the design of the chip, the extinction ratio can be increased to about 18 dB.

The measured transmission of a PhC waveguide based on pillars as a function of the defect radius is in good agreement with the 2D band diagram simulations of the line defects. This implies that the fabrication technology can be accurately controlled, which is crucial if more complicated PhC components are designed. The highest transmission is obtained for PhCs where mode crossings and slow light propagation are avoided. By developing a technology platform for pillar PhCs, a huge number of new applications in classical PICs is within reach.

The implementation of the polymer layer stack in between the photonic crystal pillars, as described in section 4.4, could not be finished before the publication of this thesis due to time constraints. Therefore, the promising theoretical results of section 2.4 could not yet be confirmed by optical measurements. However, the experimental data are expected to be available soon, after which they will be submitted for publication on a short term.

Chapter 6
Conclusions and recommendations

The aim of this work, as was stated in chapter 1, is to investigate the feasibility of the integration of pillar photonic crystals in InP-based waveguide technology. In this final chapter, the outcome of this study is summarized in section 6.1. In section 6.2, recommendations for future work are given.

6.1 Conclusions

In this thesis, several aspects of photonic crystals and their integration in photonic circuits are investigated. To start with, the theoretical properties of line defects in pillar photonic crystal are studied. These line defects are suited for photonic crystal waveguides for TM polarization. The photonic band gap properties of the crystal induce the in-plane confinement, whereas out-of-plane confinement is due to total internal reflection. By analyzing the excited Bloch modes in a 1D grating structure, it is shown that the implementation of a polymer layer stack between the pillars can significantly reduce the propagation losses of PhC waveguides. This reduction in propagation losses opens up a whole range of possibilities for practical applications. Although the implementation of a polymer slab waveguide reduces the lateral refractive index contrast, i.e. the index contrast within the unit cell of the photonic crystal, the remaining band gap gives enough freedom to design a variety of components.

Another crucial parameter in the application of photonic crystals in real circuits, is their coupling efficiency to classical ridge waveguides. The width of the access ridge waveguides and the gap between the end facet of the ridge waveguide and the first photonic crystal pillar are found to have a large influence on this coupling efficiency. Furthermore, the feasibility of using pillar photonic crystals for polarization filtering is demonstrated. Short and efficient polarization filters can be realized with photonic crystals.

A fabrication scheme has been developed to integrate the photonic crystals in circuits based on conventional waveguide technology. In this process, optical lithography is used for the part of the classical waveguide circuit with non-critical dimensions. Only in the areas with strong requirements on the feature dimensions, electron beam lithography is applied. Additionally, a fabrication process was developed for the implementation of the polymer slab waveguide. With the developed fabrication scheme, it is demonstrated that pillar-based photonic crystal waveguides can successfully be integrated in photonic circuits.

Photonic crystal waveguides based on single line defects of different lengths and different defect radii are characterized and their behavior is in agreement with simulations. A short TE polarization filter was realized and characterized. The measured transmission of a photonic crystal waveguide based on pillars is in good agreement with the 2D band diagram simulations of the line defects. This implies that the fabrication technology can be accurately controlled, which is crucial if more complicated photonic crystal components are designed.

Transmission losses of pillar waveguides in air have been characterized. A technology has been developed for filling the space between the pillars with a polymer

waveguide stack, which demonstrates that it is feasible to realize a highly planar and uniform waveguide stack between the pillars. First experiments on transmission losses of this structure are expected on a short term.

Within this project, the feasibility of pillar photonic crystals and their integration in integrated circuits has been shown. The strong confinement of light in small volumes and the wavelength and polarization dependence lead to a very high density of functions on optical chips.

6.2 Recommendations

The research that was carried out within the framework of this project was meant to explore the field of two-dimensional pillar photonic crystals. With respect to further research towards applications of these crystals in actual photonic integrated circuits, the following issues could be considered.

To optimize the coupling between classical ridge waveguides and photonic crystal waveguides, other geometries can be studied. For example, the introduction of an additional defect at the transition could further increase the coupling efficiency, or a gradual transition between both types of waveguides can be developed. Furthermore, for TE polarization filters we used the photonic crystal waveguide designs that were optimized for TM transmission. The extinction ratio can be improved if the transmission for TE polarized light is minimized at the same time.

A reliable, reproducible process should be developed for the implementation of the polymer layer stack in between the etched pillars. There are several possibilities to improve the implementation of the polymer slab waveguide. One is to adapt the geometry of the circuit which has an influence on the spinning of the polymers. Additionally, the temperature behavior of the two selected polymers is very different; the high-index polymer starts cross-linking at 200°C and at that temperature the low-index polymer behaves as a liquid. To this end, polymers should be selected with compatible temperature behavior, and the geometry of the structures on the chip should be carefully designed. Alternatively, the polymer slab waveguide can be replaced by a SiO/SiON layer stack. An important issue in that case is the lateral effective refractive index contrast, which should be high enough to ensure the presence of a photonic band gap. Another issue is the technology, special techniques may be needed to fill the area between the pillars.

After further development, the layer stack in between the pillar photonic crystal opens up the possibility of electrically contacting the devices. Photonic crystal components can be contacted to make switches if an electric field is applied over the passive semiconductor layer stack. A semiconductor stack with an active core layer can

111

be electrically contacted to create a laser, either based on a cavity inside a photonic crystal, or based on the band edge properties of a defect-free photonic crystal.

Finally, functional polymers can be applied to create active components such as switches or tunable filters. They could for instance contain liquid crystals of which the refractive index can be tuned by applying an electric field over the polymer layer stack. A change in refractive index slightly changes the wavelength range of the photonic band gap of the crystal. In this way switching or modulation of optical signals can be achieved. Another option is to use non-linear polymers. Combined with the control over propagation properties offered by PhCs, this would open up the way to a platform for non-linear optical signal processing, such as opto-optical switching, four-wave mixing, frequency doubling, etc.

Appendix A
Complex field amplitude

An FDTD calculation provides us with the real field amplitude at each grid point in the calculation window. At a certain position in the calculation window, the real field is given by

$$E(t_0) = A\cos(\phi - \omega t_0) \tag{A.1}$$

However, to obtain the correct modes and their corresponding propagation directions from the Fourier transform of a calculated field distribution, we need to know the complex field amplitude including the phase information. The complex field is given by

$$\tilde{E}(t_0) = Ae^{j(\phi - \omega t_0)} = Ae^{j\phi}e^{-j\omega t_0} \tag{A.2}$$

Thus, to obtain the complex field amplitude we need to find A and ϕ separately from the FDTD field calculation. This can be achieved by comparing the real fields at two different instances in time that are a quarter of a period apart. If $\omega\Delta t = \pi/2$, then the field at $t_0 + \Delta t$ is

$$E(t_0 + \Delta t) = A\cos(\phi - \omega t_0 - \omega\Delta t) = A\sin(\phi - \omega t_0) \tag{A.3}$$

The reference time t_0 can be chosen arbitrarily, so let $t_0 = 0$ fs, then the phase ϕ can be obtained by

$$\phi = \arctan\left(\frac{E(t_0 + \Delta t)}{E(t_0)}\right) \tag{A.4}$$

113

Since the arctan-function gives ϕ in the range from $-\pi/2$ to $\pi/2$, the cosine of the phase will always be found to be positive. However, in reality the phase can have any value and its cosine might be negative. Therefore, the sign of the cosine needs to be compared with the field and if the sign is not the same, we need to mirror the phase by increasing it with π:

$$\phi = \begin{cases} \phi & \text{if } E\left(t_0\right)\cos\left(\phi\right) \geq 0 \\ \phi + \pi & \text{if } E\left(t_0\right)\cos\left(\phi\right) < 0 \end{cases} \tag{A.5}$$

The complex field amplitude is now given by

$$\tilde{E}\left(t_0\right) = Ae^{j\phi} = \frac{E\left(t_0\right)}{\cos\left(\phi\right)}e^{j\phi} \tag{A.6}$$

The time difference Δt that should be chosen for the FDTD calculations is

$$\Delta t = \frac{\pi}{2}\omega^{-1} = \frac{\pi}{2}\left(2\pi f\right)^{-1} = \frac{\lambda}{4c} \tag{A.7}$$

In our simulations, this evaluates to $\Delta t \simeq 1.29$ fs. The time steps in our FDTD calculation is determined by the spatial grid spacing. Since we chose the grid spacing to be 15 nm in both y and z direction, the time steps are 0.0286 fs. This implies that to obtain a $\pi/2$ phase difference, we need a difference of 45.2 time steps in the FDTD calculations. In practice, the time duration of a calculation has to be an integer number of time steps. Therefore, we chose to have a time difference of 226 time steps, corresponding to 6.5 fs or a phase difference of $5\pi/2$. Since $\cos\left(x - 5\pi/2\right) = \cos\left(x - \pi/2\right) = \sin\left(x\right)$, this gives the same result in the calculation of the complex amplitude.

References

[1] K. Sakoda, *Optical Properties of Photonic Crystals*. Berlin Heidelberg, Germany: Springer-Verlag, 2001. ISBN 3-540-41199-2.

[2] E. Yablonovitch, "Inhibited spontaneous emission in solid-state physics and electronics," *Phys. Rev. Lett.*, vol. 58, pp. 2059–2062, May 1987.

[3] S. Noda, K. Tomoda, N. Yamamoto, and A. Chutinan, "Full three-dimensional photonic bandgap crystals at near-infrared wavelengths," *Science*, vol. 289, pp. 604–606, July 2000.

[4] J. D. Joannopoulos, R. D. Meade, and J. N. Winn, *Photonic crystals: molding the flow of light*. Princeton: Princeton university press, 1995.

[5] S. G. Johnson, S. Fan, P. R. Villeneuve, and J. Joannopoulos, "Guided modes in photonic crystal slabs," *Phys. Rev. B*, vol. 60, pp. 5751–5758, Aug. 1999.

[6] W. Bogaerts, *Nanophotonic Waveguides and Photonic Crystals in Silicon-on-Insulator*. PhD thesis, Ghent University, Ghent, Belgium, 2003.

[7] E. Patent, *Optical Self-Switching Effects in Mach-Zehnder Interferometers*. PhD thesis, Technische Universiteit Eindhoven, Eindhoven, The Netherlands, 2005. ISBN 90-744-4571-3.

[8] L. Soldano, *Multimode Interference Couplers. Design and Applications*. PhD thesis, Delft University of Technology, Delft, The Netherlands, 1994. ISBN 90-407-1044-9.

[9] D. Maat, *InP-based integrated MZI switches for optical communications*. PhD thesis, Delft University of Technology, Delft, The Netherlands, 2001. ISBN 90-9014700-4.

[10] M. Smit, *Integrated Optics in silicon-based aluminum oxide*. PhD thesis, Delft University of Technology, Delft, The Netherlands, 1991. ISBN 90-9004261-X.

[11] L. Augustin, J. van der Tol, R. Hanfoug, W. de Laat, M. van de Moosdijk, P. van Dijk, Y. Oei, and M. Smit, "A single etch-step fabrication-tolerant polarization splitter," *J. Lightwave Technol.*, vol. 25, pp. 740–746, Mar. 2007.

[12] H. El-Refaei, D. Yevick, and T. Jones, "Slanted-rib waveguide InGaAsP-InP polarization converters," *J. Lightwave Technol.*, vol. 22, pp. 1352–1357, May 2004.

References

[13] J. den Besten, *Integration of Multiwavelength Lasers with Fast Electro-Optical Modulators*. PhD thesis, Technische Universiteit Eindhoven, Eindhoven, The Netherlands, 2004. ISBN 90-386-1643-0.

[14] T. P. Ed., *GaInAsP alloy semiconductors*. John Wiley and Sons, 1982.

[15] P. Bienstman, *Rigorous and efficient modelling of wavelength scale photonic components*. PhD thesis, Ghent University, Ghent, Belgium, 2001.

[16] L. Wu, M. Mazilu, J.-F. Gallet, T. Krauss, A. Jugessur, and R. D. L. Rue, "Planar photonic crystal polarization splitter," *Opt. Lett.*, vol. 29, pp. 1620–1622, July 2004.

[17] V. Zabelin, L. Dunbar, N. L. Thomas, R. Houdré, M. Kotlyar, L. O'Faolain, and T. Krauss, "Self-collimating photonic crystal polarization beam splitter," *Opt. Lett.*, vol. 32, pp. 530–532, Mar. 2007.

[18] Y. Shi, D. Dai, and S. He, "Proposal for an ultracompact polarization-beam splitter based on a photonic-crystal-assisted multimode interference coupler," *IEEE Photon. Technol. Lett.*, vol. 19, pp. 825–827, June 2007.

[19] H. Kosaka, T. Kawashima, A. Tomita, M. Notomi, T. Tamamura, T. Sato, and S. Kawakami, "Superprism phenomena in photonic crystals: Toward microscale lightwave circuits," *J. Lightwave Technol.*, vol. 17, pp. 2032–2038, Nov. 1999.

[20] R. Sinha and Y. Kalra, "Design of optical waveguide polarizer using photonic band gap," *Optics Express*, vol. 14, pp. 10790–10794, Oct. 2006.

[21] V. Rinnerbauer, J. Schermer, and K. Hingerl, "Polarization splitting based on planar photonic crystals," in *Proc. Eur. Conf. on Opt. Comm. (ECOC '04)*, p. We2.1.3, Stockholm, Sweden, Sep. 5–9 2004.

[22] D. Mori and T. Baba, "Dispersion-controlled optical group delay device by chirped photonic crystal waveguides," *Appl. Phys. Lett.*, vol. 85, pp. 1101–1103, Aug. 2004.

[23] S. Kwon, H. Ryu, G. Kim, Y. Lee, and S. Kim, "Photonic bandedge lasers in two-dimensional square-lattice photonic crystal slabs," *Appl. Phys. Lett.*, vol. 83, pp. 3870–3872, Nov. 2003.

[24] D. N. Chigrin, A. V. Lavrinenko, and C. M. S. Torres, "Nanopillars photonic crystal waveguides," *Optics Express*, vol. 12, pp. 617–622, Feb. 2004.

[25] L. Spiekman, *Compact Integrated Optical Components for Telecommunication Networks*. PhD thesis, Delft University of Technology, Delft, The Netherlands, 1996. ISBN 90-9009718-X.

[26] A. Xing, M. Davanco, D. Blumenthal, and E. Hu, "Fabrication of InP-based two-dimensional photonic crystal membrane," *J. Vac. Sci. Technol. B*, vol. 22, pp. 70–73, Jan. 2004.

[27] M. Shih, W. Kim, W. Kuang, J. Cao, H. Yukawa, S. Choi, J. O'Brien, and P. Dapkus, "Two-dimensional photonic crystal mach-zehnder interferometers," *Appl. Phys. Lett.*, vol. 84, pp. 460–462, Jan. 2004.

[28] H. Park, J. Hwang, J. Huh, H. Ryu, S. Kim, J. Kim, and Y. Lee, "Characteristics of modified single-defect two-dimensional photonic crystal lasers," *IEEE J. Quantum Electron.*, vol. 38, pp. 1353–1365, Oct. 2002.

[29] R. van der Heijden, *InP-based planar photonic crystals: process development, characterization and infiltration.* PhD thesis, Eindhoven University of Technology, Eindhoven, The Netherlands, 2006. ISBN 90-386-2102-9.

[30] P. Strasser, R. Wuest, F. Robin, K. Rauscher, B. Wild, D. Emi, and H. Jackel, "An ICP-RIE etching process for InP-based photonic crystals using Cl2/Ar/N2 chemistry," in *Proc. IPRM*, pp. TuP–24, Glasgow, Scotland, 2005.

[31] M. Mulot, S. Anand, M. Swillo, M. Qiu, B. Jaskorzynska, and A. Talneau, "Low-loss inp-based photonic-crystal waveguides etched with ar/cl2 chemically assisted ion beam etching," *J. Vac. Sci. Technol. B*, vol. 21, no. 2, pp. 900–903, 2003.

[32] M. Kotlyar, T. Karle, M. Settle, L. O'Faolain, and T. Krauss, "Low-loss photonic crystal defect waveguides in InP," *Appl. Phys. Lett.*, vol. 84, pp. 3588–3590, May 2004.

[33] A. Talneau, L. Le Gouezigou, and N. Bouadma, "Quantitative measurement of low propagation losses at 1.55 um on planar photonic crystal waveguides," *Opt. Lett.*, vol. 26, no. 16, pp. 1259–1261, 2001.

[34] J. Lee, S. Oh, C. Lee, H. Ko, S. Park, K. Kim, and M. Park, "Nanofabrication of InGaAsP periodic 2D columns with square and hexagonal lattices by reactive ion etching," *Thin. Solid. Films*, vol. 475, pp. 189–193, 2005.

[35] C. Chen, C. Chen, W. Wang, F. Huang, C. Lin, W. Chiu, and Y. Chan, "Photonic crystal directional couplers formed by InAlGaAs nano-rods," *Optics Express*, vol. 13, pp. 38–43, Jan. 2004.

[36] S. Assefa, P. T. Rakich, P. Bienstman, S. G. Johnson, G. S. Petrich, J. D. Joannopoulos, L. A. Kolodziejski, E. P. Ippen, and H. I. Smith, "Guiding 1.5 μm light in photonic crystals based on dielectric rods," *Appl. Phys. Lett.*, vol. 85, no. 25, pp. 6110–6112, 2004.

[37] T. Tada, V. V. Poborchii, and T. Kanayama, "Channel waveguides fabricated in 2D photonic crystals of Si nanopillars," *Microelectronic Engineering*, vol. 63, pp. 259–265, 2002.

[38] M. Tokushima, H. Yamada, and Y. Arakawa, "1.5-μm-wavelength light guiding in waveguides in square-lattice-of-rod photonic crystal slab," *Appl. Phys. Lett.*, vol. 84, pp. 4298–4300, May 2004.

[39] M. Tinker, E. Schonbrun, J.-B. Lee, and W. Park, "Process integration and development of inverted photonic crystal arrays," *J. Vac. Sci. Technol. B*, vol. 24, pp. 705–709, Mar. 2006.

[40] M. Qiu, "Effective index method for heterostructure-slab-waveguide-based two-dimensional photonic crystals," *Appl. Phys. Lett.*, vol. 81, pp. 1163–1165, Aug. 2002.

[41] Photon Design. CrystalWave. http://www.photond.com.

[42] Peter Bienstman. CAMFR. http://camfr.sourceforge.net.

[43] W. Bogaerts, P. Bienstman, D. Taillaert, R. Baets, and D. de Zutter, "Out-of-plane scattering in 1-d photonic crystal slabs," *Opt. and Quantum Electron.*, vol. 34, pp. 195–203, 2002.

[44] W. Kuang, W. J. Kim, A. Mock, and J. O'Brien, "Propagation loss of line-defect photonic crystal slab waveguides," *IEEE J. Sel. Topics in Quantum Electron.*, vol. 12, pp. 1183–1195, nov 2006.

[45] P. Sanchis, P. Bienstman, B. Luyssaert, R. Baets, and J. Marti, "Analysis of butt coupling in photonic crystals," *IEEE J. Quantum Electron.*, vol. 40, pp. 541–550, May 2004.

[46] R. Wuest, *Nanometer-scale technology and near-field characterization of InP-based planar photonic crystal devices*. PhD thesis, ETH Zurich, Zurich Switzerland, 2007.

[47] S. Boscolo, C. Conti, M. Midrio, and C. Someda, "Numerical analysis of propagation and impedance matching in 2-D photonic crystal waveguides with finite length," *J. Lightwave Technol.*, vol. 20, pp. 304–310, Feb. 2002.

[48] R. Biswas, Z. Li, and K. Ho, "Impedance of photonic crystals and photonic crystal waveguides," *Appl. Phys. Lett.*, vol. 84, pp. 1254–1256, Feb. 2004.

[49] P. Bienstman, S. Assefa, S. Johnson, J. Joannopoulos, G. Petrich, and L. Kolodziejski, "Taper structures for coupling into photonic crystal slab waveguides," *J. Opt. Soc. Am. B*, vol. 20, Sept. 2003.

[50] S. Hughes, L. Ramunno, J. Young, and J. Sipe, "Extrinsic optical scattering loss in photonic crystal waveguides: role of fabrication disorder and photon group velocity," *Phys. Rev. Lett.*, vol. 94, Jan. 2005.

[51] K. Suzuki and B. W. Smith, *Microlithography: science and technology*. Boca Raton, US: CRC Press, 2007. ISBN 0-8247-9024-3.

[52] B. Docter, E. Geluk, M. Sander-Jochem, F. Karouta, and M. Smit, "Deep etched DBR gratings in InP for photonic integrated circuits," in *Proc. IPRM*, pp. 226–228, Matsue, Japan, 2007.

[53] T. de Vries. Personal communication.

[54] G. Roelkens, P. Dumon, W. Bogaerts, D. van Thourhout, and R. Baets, "Efficient silicon-on-insulator fiber coupler fabricated using 248-nm-deep UV lithography," *IEEE Photon. Technol. Lett.*, vol. 17, pp. 2613–2615, Dec. 2005.

[55] M. Heck, *Ultrafast integrated semiconductor laser technology at 1.55 μm*. PhD thesis, Eindhoven University of Technology, Eindhoven, The Netherlands, 2008. ISBN 978-90-386-1694-0.

[56] R. Hanfoug, L. Augustin, Y. Barbarin, J. van der Tol, E. Bente, F. Karouta, D. Rogers, S. Cole, Y. Oei, X. Leijtens, and M. Smit, "Reduced reflections from multimode interference couplers," *Electron. Lett.*, vol. 42, pp. 465–466, Apr. 2006.

[57] R. Ferrini, B. Lombardet, B. Wild, R. Houdre, and G. Duan, "Hole depth- and shape-induced radiation losses in two-dimensional photonic crystals," *Appl. Phys. Lett.*, vol. 82, pp. 1009–1011, Feb. 2003.

[58] R. Ferrini, R. Houdre, H. Benisty, M. Qiu, and J. Moosburger, "Radiation losses in planar photonic crystals: two-dimensional representation of hole depth and shape by an imaginary dielectric constant," *J. Opt. Soc. Am.*, vol. 20, pp. 469–478, Mar. 2003.

List of symbols and acronyms

Symbols

ε	dielectric constant
$\varepsilon_{h,1}$	InGaAsP dielectric constant
$\varepsilon_{h,2}$	InP dielectric constant
$\varepsilon_{h,eff}$	effective dielectric constant of the semiconductor layer stack
$\varepsilon_{l,eff}$	effective dielectric constant of the polymer layer stack
$\Delta\varepsilon_{hor}$	horizontal contrast in dielectric constant
$\Delta\varepsilon_{vert}$	vertical contrast in dielectric constant
ϕ	phase
Γ, X, M	the three high-symmetry points of the irreducible Brillouin zone of a 2D square photonic crystal lattice
λ	wavelength
ω	optical frequency
a	lattice constant
c	speed of light in vacuum ($2.99792 \cdot 10^8$ m/s)
d	layer thickness (see Fig. 2.11)
d_{etch}	etch depth
E	electric field
g	size of the gap between a photonic crystal waveguide and a ridge waveguide
G	reciprocal lattice vector
H	magnetic field
k	propagation constant
l_h	length of a semiconductor slab in the 1D grating

L	loss
n	refractive index
$n_{h,1}$	InGaAsP refractive index (see Fig. 1.3)
$n_{h,2}$	InP refractive index (see Fig. 1.3)
$n_{h,eff}$	effective refractive index of the semiconductor layer stack
$n_{l,1}$	PI refractive index (see Fig. 1.3)
$n_{l,2}$	PHFIPMA refractive index (see Fig. 1.3)
$n_{l,eff}$	effective refractive index of the polymer layer stack
N	length of a photonic crystal in periods
P	pressure
Q	quality factor
r	radius
r_d	defect radius
R	reflection
$\mathbf{R}$	elementary lattice vector
t	time
T	transmission
v_g	group velocity
w	access waveguide width

Acronyms

1D	One-Dimensional
2D	Two-Dimensional
3D	Three-Dimensional
AWG	Arrayed Waveguide Grating
CAMFR	CAvity Modeling FRamework
DBR	Distributed Bragg Reflector
EBL	Electron Beam Lithography
EDFA	Erbium Doped Fiber Amplifier
EIM	Effective Index Method
FDTD	Finite Difference Time Domain
ICP	Inductively Coupled Plasma
InGaAsP	Indium Gallium Arsenide Phosphide
InP	Indium Phosphide
MMI	Multi-Mode Interference coupler
OED	Opto-Electronic Devices
PECVD	Plasma Enhanced Chemical Vapor Deposition

PhC	Photonic Crystal
PHFIPMA	poly(1,1,1,3,3,3-hexafluoroisopropyl) methacrylate
PiA	Pillars in Air
PiP	Pillars in a Polymer layer stack
PiUP	Pillars in a Uniform Polymer
PI	polyimide
PIC	Photonic Integrated Circuit
PML	Perfectly Matched Layer
PMMA	polymethyl methacrylate
RIE	Reactive Ion Etching
SA	Saturable Absorber
SEM	Scanning Electron Microscope
SOA	Semiconductor Optical Amplifier
TE	Transverse Electric
TGA	Thermogravimetric analysis
THF	Tetrahydrofuran
TIR	Total Internal Reflection
TM	Transverse Magnetic
TU/e	Technische Universiteit Eindhoven
WDM	Wavelength Division Multiplexer

Summary

Pillar photonic crystals in integrated circuits

Photonic crystals are structures of which the refractive index is periodically modulated with a lattice constant in the order of the effective wavelength of light. If the refractive index contrast within the unit cell of the crystal is large enough, propagation in the photonic crystal is prohibited in a certain range of wavelengths. This wavelength range is called the stop band of the photonic crystal. It leads to a strong confinement of light in small volumes and to the wavelength and polarization dependent behavior of photonic crystals, and it can be exploited in photonic integrated circuits. In that case, a two-dimensional photonic crystal guides the light in the plane of the chip, whereas total internal reflection is used to confine the light in the vertical direction.

The aim of this project was to investigate the feasibility of integrating photonic crystal-based components in classical photonic integrated circuits. An important issue in this respect is the technological feasibility of the integration in indium phosphide waveguide technology. Apart from the technological issues, photonic crystal components will only be a competitive alternative to components based on conventional waveguide technology if they have much smaller footprints with the same or better performance in terms of losses.

The focus of this work is on pillar-based photonic crystals. Photonic crystals based on high-refractive-index pillars have several technological advantages over hole-type photonic crystals, where air holes are etched into the high-refractive-index dielectric material. To start with, the photonic crystals can be realized in the same layer stack as that of the classical ridge waveguides. Furthermore, to create active components electrical contacting of the pillars is possible, inherently avoiding current spreading, and heat is efficiently dissipated to the substrate.

123

The introduction of a line defect in the lattice of a photonic crystal can create a supported optical mode, resulting in a waveguide with a strongly polarization and wavelength dependent behavior. Due to the periodic intersection of the waveguide with regions of air, where vertical guiding by total internal reflection is lacking, the propagation losses in pillar-based photonic crystals are larger than in hole-type photonic crystal waveguides where the waveguide is created by a line defect of missing holes. The implementation of a polymer slab waveguide between the pillars can impose the vertical confinement in the low-refractive-index regions. The polymers reduce the in-plane refractive index contrast of the photonic crystal, but this effect is small enough to ensure the existence of the band gap. In this thesis it is shown theoretically that the propagation losses of a pillar photonic crystal waveguide are significantly suppressed by the implementation of the polymer slab waveguide.

Within the framework of this project, a fabrication process is developed to integrate photonic crystals in conventional indium phosphide waveguide technology. For the larger part of the classical circuit optical lithography is used for the definition of the structures, since this is a fast and simple process. The photonic crystals, however, are defined by electron beam lithography. This process offers a better resolution, which is required for the photonic crystal components. An additional process is developed for the implementation of the polymer slab waveguide between the pillars.

A number of photonic crystal components is modeled and described in this thesis. The properties of various waveguide defects are treated. The strong polarization dependence is used to design polarization filters. Some of the components are realized and characterized. The transmission measurements are in good agreement with the calculated band diagrams. This leads to the conclusion that with the developed fabrication process, the dimensions of different waveguide defects can be controlled with a high accuracy, which is essential for the application of photonic crystals in photonic integrated circuits.

The results of the research project that are described in this thesis show that pillars offer useful and advantageous possibilities to apply photonic crystals in photonic integrated circuits based on conventional waveguide technology.

Abigaël Kok

Samenvatting

Fotonische kristallen gebaseerd op pilaren in geïntegreerde optische circuits

Fotonische kristallen zijn structuren waarvan de brekingsindex periodiek gemoduleerd is met een roosterconstante die in de orde van grootte van de (effectieve) golflengte ligt. Indien het verschil in brekingsindex in de eenheidscel van het rooster voldoende groot is, ontstaat er een golflengtegebied waarvoor propagatie in het kristal niet toegestaan is, de zogenaamde stopband van het fotonische kristal. Dit leidt tot sterke opsluiting van licht in kleine volumes en het golflengte- en polarisatieafhankelijke gedrag van fotonische kristallen, die gebruikt kunnen worden in geïntegreerd optische schakelingen. Daarvoor wordt een twee-dimensionaal fotonisch kristal gebruikt om het licht in horizontale richting te geleiden. In verticale richting wordt gebruikt gemaakt van totale interne reflectie om het licht op te sluiten.

Het doel van dit promotieproject was de integreerbaarheid van fotonische kristallen in conventionele geïntegreerd optische circuits te onderzoeken. Belangrijk hierbij is de technologische haalbaarheid van fotonische kristallen in de conventionele circuits, gebaseerd op indiumfosfidetechnologie. Uiteraard moeten de componenten in fotonische kristallen voordelen hebben ten opzichte van componenten die in conventionele golfgeleidertechnologie gerealiseerd kunnen worden. Alleen als de fotonische kristalcomponenten (veel) kleinere afmetingen hebben, en de verliezen vergelijkbaar of lager zijn, zullen ze een aantrekkelijk alternatief vormen voor bestaande componenten.

Vanwege de technologische haalbaarheid heeft dit onderzoek zich geconcentreerd op fotonische kristallen van pilaren met een hoge brekingsindex omgeven door een diëlektricum met een lage brekingsindex. Deze geometrie heeft verschillende voorde-

125

len ten opzichte van gaatjes met een lage brekinsindex, geëtst in een diëlektricum met een hoge brekingsindex. Ten eerste kan voor pilaarkristallen hetzelfde lagenpakket gebruikt worden als voor de conventionele circuits. Bovendien is de fabricagetechnologie van deze kristallen compatibel met die van de conventionele circuits. Ook actieve componenten gebaseerd op pilaarkristallen kunnen gerealiseerd worden. Daarbij is elektrische contactering mogelijk. De ladingsdragers worden geleid in de pilaren die gecontacteerd zijn, en warmte kan gemakkelijk afgevoerd worden via het substraat.

Door het aanbrengen van een lijndefect in een fotonisch kristal kan een lokale toestand van het optische veld gecreëerd worden, resulterend in een golfgeleider die sterk polarisatie- en golflengteafhankelijk gedrag vertoont. Doordat de golfgeleider periodiek onderbroken wordt door gebieden met lucht, zonder opsluiting door totale interne reflectie, zijn de propagatieverliezen van fotonische kristallen van pilaren groter dan die van gaten in een materiaal met hoge brekingsindex. Het aanbrengen van een aantal lagen polymeren tussen de pilaren van het kristal kan deze verticale opsluiting wel teweegbrengen. De polymeren verlagen het indexcontrast in het fotonische kristal in horizontale richting, maar dit effect is te klein om de stopband af te sluiten. In dit proefschrift is theoretisch aangetoond dat de verliezen van fotonische kristallen van pilaren significant verkleind kunnen worden door het aanbrengen van de polymeren.

Binnen het kader van dit project is een fabricageproces ontwikkeld om de fotonische kristallen te integreren in de conventionele indiumfosfide golfgeleidertechnologie. Hierbij wordt voor het grootste deel van het klassieke circuit optische lithografie gebruikt, aangezien dit een snel en eenvoudig toe te passen techniek is. Voor de fotonische kristallen is echter een nauwkeurigere definitie van de structuren nodig. Daarvoor is gebruik gemaakt van elektronenbundellithografie. Ook is een proces ontwikkeld voor het aanbrengen van de polymeren.

Een aantal componenten is gemodelleerd en beschreven in dit proefschrift. De eigenschappen van verschillende golfgeleiderdefecten zijn behandeld. De sterke polarisatieafhankelijkheid is gebruikt om polarisatiefilters te ontwerpen. Een aantal componenten is gerealiseerd en gekarakteriseerd. Uit de overeenstemming van de transmissiemetingen met de berekende banddiagrammen blijkt dat met het ontwikkelde fabricageproces de afmetingen van verschillende lijndefecten met grote precisie gecontroleerd kan worden. Deze controle is essentieel voor de toepassing van fotonische kristallen in geïntegreerd optische circuits.

De resultaten van het hier beschreven onderzoek laten zien dat pilaren bruikbare en voordelige mogelijkheden bieden om fotonische kristallen toe te passen in fotonische schakelingen gebaseerd op conventionele golfgeleidertechnologie.

Abigaël Kok

Dankwoord

Nu het promotietraject bijna voltooid is, is het moment gekomen om iedereen te bedanken die in de afgelopen jaren - direct of indirect - heeft geholpen bij het tot stand komen van dit proefschrift. In de eerste plaats wil ik Jos van der Tol bedanken voor de begeleiding gedurende de afgelopen jaren, jouw deur stond altijd open en je enthousiasme werkt aanstekelijk. Meint Smit, bedankt voor de kans die je me gegeven hebt om mijn promotieproject bij OED uit te voeren. Roel Baets, de discussies die we tijdens uw bezoeken aan de TU/e en soms via de telefoon hebben gevoerd, zijn erg waardevol geweest en hebben een grote stempel gedrukt op de inhoud van dit proefschrift. Bedankt voor uw interesse in mijn onderzoek. Siang Oei, bedankt voor de vele discussies en adviezen, die me hebben geholpen om de technologieontwikkeling op te starten.

In de jaren die ik bij OED heb doorgebracht, heb ik op allerlei vlakken veel ondersteuning gekregen van collega's. Erik Jan, bedankt voor jouw hulp met allerlei apparatuur, maar met name de EBL. Je hebt me niet alleen vaak geholpen in de clean room, maar je was ook geïnteresseerd in de theoretische kant van de fotonische kristallen. Kitty, je hebt een belangrijke bijdrage geleverd aan de ontwikkeling van een proces om optische litho en e-beam litho te combineren. En de middagjes shoppen waren een welkome afwisseling! Barry, je bent altijd in voor nieuwe experimenten met exotische oplosmiddelen in de clean room, zonder jou had ik mijn chip niet kunnen realiseren. Ben, je was de stille kracht achter het draaiende houden van de clean room. Bedankt ook voor de 'extracurriculaire' activiteiten zoals de organisatie van het medewerkersfestival toen de TU/e 50 jaar bestond, de uitjes met OED en de borrels in het Walhalla. Tjibbe, bedankt voor je adviezen over litho's, de PECVD, en onze favoriet de ellipsometer. Fouad, bedankt voor jouw onuitputtelijke bron van ideeën. Hans, je bent zo vaak onmisbaar gebleken in de afgelopen jaren, ik ben je dankbaar voor je ondersteuning en voor je goede humeur. Els, het eten was heel gezellig, net als de jaarlijkse OED

eindejaarsvieringen. Ik hoop dat het je goed gaat in Twente. Susan en José, bedankt voor de ondersteuning op het administratieve vlak.

Tijdens mijn promotieproject heb ik veel plezier beleefd aan het samenwerken met anderen. Roberto, I would like to thank you for your enthousiasm during your Masters' project. It was fun working with you. Robbie, de 'klasjes' hebben zeker bijgedragen aan het begrip van de fysica achter fotonische kristallen. Chris, zonder jouw kennis van polymeren had dit proefschrift er anders uit gezien. En zonder jouw creatieve bijdrage voor de LEOS Benelux poster hadden we die posterprijs niet gewonnen. Harm en Rob, de wekelijkse projectvergaderingen waren een waardevol platform voor discussies. Bedankt voor jullie interesse en de prettige samenwerking, en veel succes met de voortzetting van jullie werk op het gebied van fotonische kristallen. Peter Bienstman, bedankt voor jouw ondersteuning op het gebied van de CAMFR-berekeningen en voor de borrel in de Vooruit in Gent.

Kamergenootjes Boudewijn en Luc, bedankt voor de gezelligheid op kamer 10.35. Boudewijn, de door jou ontwikkelde ICP ets kwam voor mijn project precies op tijd. Bedankt ook voor je geduld als je weer eens tussen twee mopperende 'schrijvers' zat en voor de nodige pastasalades en pannenkoeken. Luc, ik zou je tekort doen als ik je alleen bedankte voor de hulp bij het maken van veel figuren en grafieken en de praktische hulp in de OLA en de clean room. We hebben heel wat keren afgezien maar we mogen trots zijn op het resultaat. Martijn en Genia, bedankt voor alle etentjes en borrels die we hebben gedeeld, inclusief de bijbehorende goede gesprekken. Jan Hendrik, het samen treinen heb ik altijd erg gezellig gevonden. Ook de uitjes naar de Verkadefabriek en Winterswijk en de vele Bossche bollen waren erg goed! Xaveer, in combinatie met dat handje doping heeft jouw dvd-box wonderen gedaan. Bedankt voor het draaiende houden van oa. 'mijn' Linux-rekenmonster. Erwin, ik heb goede herinneringen aan een workshop in Metz (hoe zat het nog eens met die alfa-factor?). Ling, it was great getting to know you, especially sharing the samba workshop was great fun. Francisco, goed dat je me hebt overgehaald om mee te gaan naar mijn allereerste salsales. Het salsafeest in Rotterdam was erg leuk, bedankt voor je gastvrijheid. Yohan et Rabah, I very much enjoyed our trip to a conference in San Francisco, and the week we spent traveling afterwards. It was a great experience. Mark, wat hadden we een goede smoes om uit eten te gaan in plaats van te gaan hardlopen - en het was er wat mij betreft niet minder gezellig om. Pietro y José, gracias por hablar español conmigo, ya que se me está olvidando bastante rápido. Many thanks to Fokke, Bauke, Martin, Uzma, Mahmoud, Omar, Roger, Hugo, Youcai, Stefano and Mirvais for their interest and I wish all of them the best for their scientific careers as well as in their personal lifes. Furthermore, I would like to thank all Masters' students that came to Eindhoven to stay in our group for a few months. Germain, it would be great

to meet again in a completely different research area.

Gelukkig was er naast mijn promotie ook tijd voor de broodnodige ontspanning. Echte vrienden leren je kritisch te zijn en te relativeren. En echte vrienden hoeven elkaar niet wekelijks te zien of te spreken om er toch voor elkaar te zijn op de momenten die echt belangrijk zijn. Desondanks hoop ik straks meer tijd met jullie te kunnen doorbrengen dan ik in de afgelopen tijd voor jullie vrij kon maken.

Een paar vriendinnen wil ik hier met name noemen. Om te beginnen Anabella, ondanks jouw eigen druktes en beslommeringen vond jij de tijd en de inspiratie om een ontwerp te maken voor het omslag van dit proefschrift. Bedankt, niet alleen daarvoor maar ook voor de vele etentjes, bioscoopbezoeken en films. Bauke en Karen, ik hoop dat we nog vaak kunnen afspreken voor lunches, high teas en dinertjes. Bauke, jouw talent om kleine, maar zo belangrijke steuntjes te geven op cruciale momenten is bewonderenswaardig. Bedankt voor alle lieve kaartjes, bloemen en cadeautjes. Karen, fijn dat we de promotieperikelen hebben kunnen delen. De summerschool op Corsica was onvergetelijk.

Vrienden kun je kiezen, familie niet. Gelukkig heb ik het wat dat betreft heel erg getroffen. Miel en Josine, bedankt voor het tweede thuis dat jullie me bieden. Oma Marietje, ik hoop dat we elkaar nog lang mogen kennen. Met alle kinderen en kleinkinderen, en die van oom Joosje ben je nog altijd even geïnteresseerd in het reilen en zeilen van ieder afzonderlijk. Het is maar goed dat de e-mail lekker snel gaat. Ook een bedankje aan mijn broers is hier op zijn plaats. Fernand, bedankt voor al die keren dat je voor me klaarstond als er gesjouwd of geklust moest worden. Peter, bedankt voor de gezelligheid als ik in Heinkenszand kom. Papa en mama, jullie hebben het allemaal mogelijk gemaakt. Bedankt voor alle kansen en mogelijkheden die jullie ons gegeven hebben. Jullie hebben altijd voor ons klaar gestaan, en doen dat nog steeds. Het is fijn om thuis te komen.

Het mooiste aan mijn promotietijd is dat ik jou heb leren kennen, Milan. Bedankt dat je er altijd voor me was, ik hoop dat dat nog lang zo blijft.

Els

Curriculum Vitae

Abigaël (Els) Kok was born in Heinkenszand (The Netherlands) April 12, 1979. After finishing secondary school in 1997 (Sint Willibrord College, Goes, The Netherlands), she studied Applied Physics at Twente University (Enschede, The Netherlands). With optics as a main subject, she had her practical training at the Centro de Investigaciones en Óptica (Léon, Guanajuato, México) where she stayed for five months. Her Master's thesis was on multimode wavelength demultiplexers based on arrayed waveguide gratings using polymer waveguide technology. The research was carried out at the Lightwave Devices Group under supervision of dr. Sami Musa and ir. Albert Borreman. In December 2002 Els obtained her Master of Science degree in Applied Physics at Twente University.

After her graduation Els continued her research for six months at the Lightwave Devices Group (Twente University) as a junior researcher. In September 2003 she started her PhD project at the Eindhoven University of Technology (The Netherlands) at the Opto-Electronic Devices group (dr. Jos van der Tol, prof. dr. ir. Meint Smit) at the Faculty of Electrical Engineering.

Starting on April 1, 2008, Els continues her career at FEI Company (The Netherlands), specializing in transmission electron microscopy.

List of publications

- A.A.M. Kok, E.J. Geluk, F. Karouta, J.J.G.M. van der Tol, R. Baets, and M.K. Smit, "Short polarization filter in pillar-based photonic crystals," accepted for publication in *IEEE Photon. Technol. Lett.*.

- A.A.M. Kok, J.J.G.M. van der Tol, R. Baets, and M.K. Smit, "Reduction of propagation loss in pillar-based photonic crystal waveguides," accepted for publication in *J. Lightwave Technol.*.

- J.M. Pozo, E.A.J.M. Bente, M.J.R. Heck, F. Karouta, A.A.M. Kok, J.J.G.M. van der Tol, M.K. Smit, S. Anantathanasarn, R. Nötzel, M. Yousefi, and D. Lenstra, "InP-based lasers and photonic crystal devices for integrated photonics," in *10th Int. Conf. on Transparent Optical Networks (ICTON)*, Jun. 2008.

- A.A.M. Kok, J.J.G.M. van der Tol, E.J. Geluk, F. Karouta, and M.K. Smit, "Pillar photonic crystal for polarization filtering," in *Proc. Eur. Conf. on Int. Opt. (ECIO)*, Eindhoven, The Netherlands, Jun. 2008.

- J.J.G.M. van der Tol, L.M. Augustin, A.A.M. Kok, U. Khalique, and M.K. Smit, "Use of polarization in InP-based integrated optics," in *2008 Conference on Lasers and Electro-Optics (CLEO)*, 2008.

- A.A.M. Kok, R. Meneghelli, J.J.G.M. van der Tol, and M.K. Smit, "Fabrication and characterization of pillar-based photonic crystal waveguides," in *Proc. IEEE/LEOS Symposium (Benelux Chapter)*, pp. 51–54, Brussels, Belgium, Dec. 2007.

- A.A.M. Kok, E.J. Geluk, J.J.G.M. van der Tol, and M.K. Smit, "Optical characterization of pillar-based photonic crystal waveguides in InP/InGaAsP/InP technology," in *Proc. NanoNed Symp.*, p. 104, Nijmegen, The Netherlands, Dec. 2007.

- A.A.M. Kok, E.J. Geluk, B. Docter, J.J.G.M. van der Tol, R. Nötzel, M.K. Smit, and R. Baets, "Transmission of pillar-based photonic crystal waveguides in InP technology," *Appl. Phys. Lett.*, vol. 91, p. 201109, Nov. 2007.

- R. Meneghelli, A.A.M. Kok, J.J.G.M. van der Tol, and M.K. Smit, "Integrazione tra guide d'onda ridge e guide a cristallo fotonico tramite taper efficienti," in *Proc. Fotonica '07*, pp. 21–23, Montova, Italy, May 2007.

- A.A.M. Kok, J.J.G.M. van der Tol, Y.S. Oei, and M.K. Smit, "Modeling of efficient coupling structures for integration of pillar photonic crystals in photonic integrated circuits," in *Proc. NanoMeta*, Seefeld, Austria, Jan. 2007.

- A.A.M. Kok, R. Meneghelli, J.J.G.M. van der Tol, and M.K. Smit, "Efficient coupling structures for integration of pillar photonic crystals with ridge waveguides," in *Proc. IEEE/LEOS Symposium (Benelux Chapter)*, pp. 37–40, Eindhoven, The Netherlands, Dec. 2006.

- A.A.M. Kok, R. Meneghelli, J.J.G.M. van der Tol, and M.K. Smit, "Efficient coupling structures for integration of pillar photonic crystals in photonic integrated circuits," in *Proc. NanoNed Symp.*, p. 91, Eindhoven, The Netherlands, Nov. 2006.

- A.A.M. Kok, E.J. Geluk, M.J.H. Sander-Jochem, J.J.G.M. van der Tol, Y.S. Oei, and M.K. Smit, "Two-dimensional photonic crystals based on InP rods," in *Proc. IEEE/LEOS Symposium (Benelux Chapter)*, pp. 273–276, Mons, Belgium, Dec. 2005.

- A.A.M. Kok, C.M. van Heesch, E.J. Geluk, M.J.H. Sander-Jochem, J.J.G.M. van der Tol, Y.S. Oei, and M.K. Smit, "Building two-dimensional photonic crystals on InP with rods," in *Proc. NanoNed Symp.*, Groningen, The Netherlands, Dec. 2005.

- A.A.M. Kok, E.J. Geluk, J.J.G.M. van der Tol, F. Karouta, Y.S. Oei, and M.K. Smit, "Guiding light between pillars in InP-based photonic crystals," in *Proc. PECS-VI*, Crete, Greece, Jun. 2005.

- C.F. Carlström, R.W. van der Heijden, A.A.M. Kok, R.W. van der Heijden, F. Karouta, J.J.G.M. van der Tol, R. Nötzel, P.J. van Veldhoven, and H.W.M. Salemink, "Inductively coupled plasma etching of deep photonic crystal holes in InP using Cl_2," in *Proc. IPRM*, pp. 500–503, Glasgow, Scotland, 2005.

- S. Musa, A. Borreman, A.A.M. Kok, M.B.J. Diemeer, and A. Driessen, "Experimental Study of Bent Multimode Optical Waveguides," *Appl. Opt.*, vol. 43, pp. 5705–5707, Oct. 2004.

- A.A.M. Kok, S. Musa, A. Borreman, M.B.J. Diemeer, and A. Driessen, "Completely multimode arrayed waveguide grating-based wavelength demultiplexer," in *Proc. EUROCON*, vol. 2, pp. 422-426, Ljubljana, Slovenia, Sept. 2003.

- A. Borreman, A.A.M. Kok, M.B.J. Diemeer, and A. Driessen, "Low-cost polymeric multimode optical devices," in *Proc. IEEE/LEOS Workshop (Benelux Chapter)*, Mons, Belgium, June 2003.

- S. Musa, A. Borreman, A.A.M. Kok, M.B.J. Diemeer, and A. Driessen, "Multimode arrayed waveguide grating-based demultiplexers for short-distance communication," in *Proc. Eur. Conf. on Int. Opt. (ECIO)*, pp. 367–370 Prague, Czech Republic, Apr. 2003.

- A. Borreman, S. Musa, A.A.M. Kok, M.B.J. Diemeer, and A. Driessen, "Fabrication of polymeric multimode waveguides and devices in SU-8 photoresist using selective polymerization," in *Proc. IEEE/LEOS Symposium (Benelux Chapter)*, pp. 83–86, Amsterdam, The Netherlands, Dec. 2002.